Maria Henriksen Hasselø

Optical Measurements and Numerical Modeling of the Temperature Distribution Across a Proton Exchange Membrane (PEM) Fuel Cell

Master's thesis

NTNU
Norwegian University of
Science and Technology

Maria Henriksen Hasselø

Optical Measurements and Numerical Modeling of the Temperature Distribution Across a Proton Exchange Membrane (PEM) Fuel Cell

NTNU
Norwegian University of
Science and Technology

Preface

When selecting the topic for my project thesis last spring, which would eventually evolve into this Master's thesis, I had no prior experience with independent laboratory work. However, my previous and forthcoming internships in the hydrogen industry sparked my interest in exploring the current research topics surrounding hydrogen technologies. Over the past year, I have gained confidence in the lab and have come to enjoy testing my practical problem-solving skills. Although there have been moments of frustration due to technical challenges and setbacks, these experiences have taught me the value of patience and persistence. In the end, I am grateful for the experience and everything it has taught me.

With that said, this thesis would not have been possible without the support and guidance of several individuals. I owe a huge thanks to my supervisor, Jacob Lamb, for his assistance with both technical and report-related questions in our guidance meetings over the past year. I would also like to thank Markus Solberg Wahl, who introduced me to optical sensors, an area I had no previous experience with before this fall. Furthermore, I need to thank Michael Aron Fried and Marco Sauermoser for their patience in answering all my emails about operating the fuel cell tester station. Finally, I want to thank Benedikt Julius Eichner for sharing his knowledge from the thermal conductivity lab and giving me some ideas for my model design.

Abstract

Effective heat management is essential for optimizing the performance of Proton Exchange Membrane (PEM) fuel cells. While numerous models exist to predict the thermal behavior of PEM fuel cells, they are limited by the lack of experimental data to validate their designs. This is largely due to the absence of experimental techniques that withstand their electrically and chemically harsh environment while remaining small enough to avoid interference with cell operation.

In the initial part of this thesis, a novel approach for in-situ temperature measurements using optical Fiber Bragg Grating (FBG) sensors is investigated. A single FBG is embedded between two Gas Diffusion Layers (GDLs) at the cathode of a laboratory PEM fuel cell. Furthermore, the FBG is calibrated against a co-located thermocouple, showing a linear response over the operating range. During operation, the FBG records a significant temperature increase with changes in current and exhibits a good temporal response. At the cathode GDL, a temperature rise of 13.13 °C is observed between 0.32 and 1.4 A/cm^2. In conclusion, the initial part of this study offers valuable insights into the thermal behavior of PEM fuel cells and highlights FBGs as a potential sensor technology for electrochemical devices. Moreover, the presented sensor implementation is highly advantageous as it is easily adaptable, requiring only off-the-shelf components.

In the second part of this thesis, a one-dimensional thermal model is created to simulate the temperature distribution across the laboratory PEM fuel cell during testing. In contrast to traditional models, which typically enforce a fixed temperature across the graphite plate, this model integrates the FBG-measured temperatures as the boundary condition. Furthermore, experimentally derived thermal conductivities of the PEM fuel cell components are added to the model. This implementation of empirical data is seen to have a notable impact on the simulated temperature profiles, enhancing their accuracy. This is particularly true at higher currents where a temperature gradient is observed over the graphite plate. Recognizing this temperature gradient is a crucial step toward advancing numerical PEM fuel cell models.

Sammendrag

Effektiv varmestyring er avgjørende for å optimalisere ytelsen til Proton-utveksling membran (PEM) brenselsceller. Flere numeriske modeller er designet for å predikere temperaturvariasjonene til en PEM brenselcelle under drift. Det er derimot manglende eksperimentell data til å validere disse modellene. Til tross for en høy etterspørsel etter eksperimentelle målinger, har forskningen vært bremset på grunn av mangelen på et egnet måleinstrument som er upåvirket av elektrokjemien i brenselcellen.

Denne hovedoppgaven presenterer en ny tilnærming for å oppnå nøyaktige temperatur målinger ved bruk av en optisk fiber med Fiber Bragg Gitter (FBG) sensorer. En FBG sensor er installert mellom to gassdiffusjonslag (GDL) på katodesiden til en PEM brenselcelle. FBGen er så kalibrert mot et nærliggende termometer, hvor en lineær respons til temperaturøkningen er observert. Under drift av PEM brenselcellen, måler FBGen en betydelig temperaturøkning for økt strømtetthet med en god varmerespons. Over en økning av strømtettheten fra 0.32 til 1.4 A/cm^2, måler FBGen en temperaturøkning på 13.13 °C. Sensorinstallasjonen som er presentert i denne hovedoppgaven er enkel å gjenskape for videre forskning, da den ikke krever spesiallagde deler. Videre gir funnene verdifull innsikt i temperaturvariasjonene i PEM-brenselceller, og fremhever optiske FBG-sensorer som en egnet sensorteknologi for elektrokjemiske celler.

Videre i denne hovedoppgaven er det utviklet en en-dimensjonal modell for å simulere temperaturvariasjonen over PEM-brenselcellen for varierende strømtetthet og vanninnhold. I motsetning til konvensjonelle modeller, som vanligvis antar konstant temperatur over grafittplaten, anvender denne modellen temperaturene målt i første del av oppgaven. Ved å anvende eksperimentell data økes nøyaktigheten til modellen, spesielt ved høy strømtetthet hvor temperaturvariasjoner over grafittplatene er observert. Å anerkjenne denne temperaturvariasjon er avgjørende for videre utvikling av numeriske modeller for PEM brenselceller.

Nomenclature

Abbreviations

ACL   Anodic Catalyst Layer

BP   Bipolar Plate

CC   Current Collector

CCL   Cathodic Catalyst Layer

CCM Catalyst Coated Membrane

CL   Catalyst Layer

FBG   Fiber Bragg Grating

FCT   Fuel Cell Tester

GDL Gas Diffusion Layer

HOR Hydrogen Oxidation Reaction

MEA Membrane Electrode Assembly

MPL Micro-Porous Layer

OCV Open Circuit Voltage

ORR Oxygen Reduction Reaction

PEM Proton-Exchange Membrane or Polymer Electrolyte Membrane

PTFE Polytetrafluoroethylene

RH   Relative Humidity

SDG Sustainable Development Goal

TCR Thermal Contact Resistance

Greek Letters

α	Thermal Expansion Coefficient	[-]
δ	Component Thickness	$[m]$
η	Sum of Electrode Overpotentials	$[V]$
η_a	Activation Overpotential	$[V]$
η_c	Concentration Overpotential	$[V]$
κ	Thermal Conductivity	$[W/mK]$
Λ	Grating Period	$[m]$
λ	Membrane Humidity Level	$[H_2O/SO_3^-]$
λ_B	The Bragg Wavelength	$[\mu m]$
λ_{H_2}	Stoichiometric Coefficient for Feed Hydrogen	[-]
λ_{O_2}	Stoichiometric Coefficient for Feed Oxygen	[-]
θ_1	Angle of Incidence	$[rad]$
θ_2	Angle of Refraction	$[rad]$
θ_C	Critical Angle	$[rad]$
ε	Strain	[-]
ε_{eff}	Energy Efficiency	$[\%]$

Roman Letters

ΔH	Reaction Enthalpy	$[J]$
ΔS	Entropy Change	$[J/K]$
Δx	Sample Thickness	$[m]$
$\dot{m}$	Mass Flow Rate	$[kg/s]$
$\dot{Q}$	Heat Rate	$[W]$
$\overline{g}$	Gibbs Free Molar Energy	$[J/mole]$
$\overline{h}$	Molar Enthalpy	$[J/mole]$
$\overline{s}$	Molar Entropy	$[J/moleK]$
A	Area	$[m^2]$
C	Speed of Light in Medium	$[m/s]$
c_p	Constant Pressure Specific Heat	$[kJ/kgK]$
c_V	Constant Volume Specific Heat	$[kJ/kgK]$
E_{cell}^{rev}	Reversible Cell Potential	$[V]$
E_{cell}	Cell Potential	$[V]$
F	Faraday's Constant	$[C/mole]$
G	Gibbs Free Energy	$[J]$
h	Specific Enthalpy	$[J/kg]$
h_{conv}	Convective Heat Transfer Coefficient	$[W/m^2K]$
I	Current	$[A]$
j	Current Density	$[A/cm^2]$
j_0	Exchange Current Density	$[A/cm^2]$
j_l	Limiting Current Density	$[A/cm^2]$
K	Conductivity	$[S/m]$
M	Molar Mass	$[kg]$

N	Total Amount of Elements in a Quantity	$[-]$
n	Charge Transfer	$[-]$
n	Refractive Index	$[-]$
n_{eff}	Effective Refractive Index of an FBG Sensor	$[-]$
P	Power	$[W]$
p	Pressure	$[N/m^2]$
q''	Heat Flux	$[W/m^2]$
Q	Heat	$[J]$
Q_{rev}	Reversible Heat	$[J]$
R	Electric Resistance	$[\Omega]$
R	Universal Gas Constant	$[J/moleK]$
r	Area Specific Resistance	$[\Omega m^2]$
r_t	Area Specific Thermal Resistance	$[Km^2/W]$
R_{th}	Thermal Resistance	$[K/W]$
S	Standard Deviation	$[-]$
T	Temperature	$[K]$
W	Work	$[J]$
W_{rev}	Reversible Work	$[J]$

Contents

List of Figures

List of Tables

Chapter 1

Introduction

1.1 Background and Motivation

Addressing climate change is one of the biggest challenges of modern society. In the Paris Agreement, adopted in 2015, world leaders at the UN Climate Change Conference (COP21) set long-term goals to limit global warming and invest in a low-carbon future [1]. This was also the year when the UN General Assembly adopted the 17 Sustainable Development Goals (SDGs). Amongst the 17 SDGs, SDG 7 specifically addresses the energy sector by calling out to "ensure access to affordable, reliable, sustainable, and modern energy for all" [2]. Reaching this common goal demands nothing less than a complete transformation of the global energy system, and renewable energy sources are right in the center of this transformation [3]. However, having an energy system primarily powered by intermittent renewable sources, such as solar and wind, will result in a weather-dependent energy supply. Previously, energy production has been scaled according to the demand, but this is changing with the rise of renewables [4]. Instead, the energy generation will align with the weather conditions, prioritizing production when resources are accessible. Thus, carbon-neutral energy storage solutions are required to achieve the balance between supply and demand [4].

Hydrogen is highlighted as one of the energy storage solutions endorsed by the Intergovernmental Panel on Climate Change (IPCC) in 2022 [5]. Recognized for its flexibility, hydrogen systems have the potential to balance energy fluctuations across various timescales, ranging from short-term (minutes) to long-term (seasonal) variations [6]. The effective utilization of hydrogen as a low-carbon energy storage solution relies on several technologies, such as water electrolyzers, hydrogen fuel cells, and various distribution and storage systems [6]. Therefore, maximizing the

potential for hydrogen to support the growing share of renewables heavily relies on minimizing losses across these critical technologies. This thesis focuses exclusively on exploring the Proton Exchange Membrane (PEM) fuel cell technology.

Amongst various fuel cell technologies, the PEM fuel cell stands out as the most developed and surpasses other fuel cells in performance [6]. The PEM fuel cell facilitates an electrochemical reaction between hydrogen and oxygen gas, generating electricity with a general efficiency of 50% [7, 8]. In addition to generating electricity, this reaction releases a substantial amount of heat. Approximately half of the energy carried by the hydrogen is lost as heat in the fuel cell [8]. Thus, managing this heat is one of the main design challenges when it comes to PEM fuel cells, as staying within their narrow operating range is crucial for both performance and long-term durability. One of the key challenges in designing efficient thermal management lies in understanding the heat sources and thermal gradients within the PEM fuel cell. Although the total heat released from the PEM fuel cell is easily calculated from the cell potential, it is much more challenging to know the localized heat generation and, hence, the temperature distribution.

In the last decade, computational models have given significant insight into the temperature distribution of the PEM fuel cell for different operating conditions. However, in-situ experimental measurements are lacking to confirm their predictive capabilities [9]. The chemically harsh and electrically noisy environment within a PEM fuel cell poses a challenge for most standard sensing technologies [10]. However, optical fiber Bragg grating (FBG) sensors have been suggested as a suitable sensing technology for electrochemical devices [10]. Hence, this thesis aims to further investigate the temperature distribution within a PEM fuel cell using FBG sensors. Furthermore, the measured temperatures will be utilized to model the temperature distribution, incorporating material characteristics previously found in the associated project thesis [7]. Incorporating empirically derived data into a thermal model of the PEM fuel cell is expected to result in a more precise representation of its temperature profile. Ultimately, this can contribute to advancements in thermal management strategies for optimizing PEM fuel cell performance.

1.2 Research Objectives and Methodology

The main objective of this thesis is to acquire in-situ temperature measurements within a PEM fuel cell, while also showcasing the application of optical FBG sensors for this exact purpose. FBGs have been recognized as particularly well suited for in-situ measurements within PEM fuel cells as they are immune to their electrochemical environment [9]. An FBG will be installed between a double GDL at the cathode of a laboratory-scaled PEM fuel cell. Furthermore, the fuel cell housing will be placed into a fuel cell tester (FCT) station at the Varmeteknisk Laboratory at NTNU Trondheim. Here, the installed FBG will be used to measure the steady-state temperature while operating the PEM fuel cell at different current densities. To the best of the author's knowledge, no previous research has explored the use of FBGs for temperature sensing within the GDL of a running PEM fuel cell. Additionally, the proposed method is highly reproducible, as it utilizes only off-the-shelf components. Hence, achieving temperature measurements for other operating conditions can easily be obtained.

The second objective of this work is to develop a one-dimensional thermal model based on the experimental results. This model will incorporate the in-situ temperature measurements, the operating conditions, the cell's I-V relationship, as well as the thermal conductivities previously found in the project thesis [7]. With these implementations, the model will be designed to simulate the temperature profiles experienced by the laboratory PEM fuel cell during the temperature measurements. In the model, the temperature at the cathode GDL will be set to the FBG-measured temperature, while the remaining temperatures will be calculated based on Fourier's first law, considering the modeled heat sources. The model will use the measured I-V relationship to estimate its losses and corresponding heat sources. Additionally, heat sources and sinks related to mass transport will be implemented for completeness.

Furthermore, the simulated temperature distribution will be compared to previous model designs. By incorporating in-situ temperature measurements, this model stands out and offers valuable insights into how experimental data influence the modeled temperature profile. Ultimately, the broader goal of this work is to gain a deeper understanding of temperature variations within the PEM fuel cell. This knowledge can contribute to designing a more efficient thermal management system, ultimately enhancing its performance and extending its expected lifetime.

1.3 State of The Art

For a long time, the PEM fuel cell was assumed to be isothermal during operation
[11]. However, this assumption is far from reality, particularly at higher current
densities. Vie was the first to contradict this by reporting a 6 °C temperature
difference at 1 A/cm^2 in 2002 [12]. This realization sparked an interest in modeling
the temperature distribution within the PEM fuel cell. However, accomplishing
this was challenging at the time due to a lack of knowledge regarding the thermal
properties of the PEM fuel cell components. Therefore, several efforts have been
made in recent years to measure their thermal conductivities [13].

In 2009, Burheim et al. published a method for measuring the thermal conductivity
of materials for various clamping pressures [11]. This paper was the first to report
on the thermal conductivity of a Nafion membrane as a function of its water content.
It was found that the thermal conductivity of Nafion increased from 0.177 ± 0.008
$\frac{W}{Km}$ to 0.254 ± 0.016 $\frac{W}{Km}$ when going from a fully dry to a fully humidified state
[11]. In later years, the thermal conductivities of all PEM fuel cell components
have been extensively studied, taking into account various factors such as material
compositions, water content, compression, gas content, direction (through-plane and
in-plane), and PTFE loading [14, 15]. In 2017, Burheim reviewed how this research
had advanced our understanding of the internal temperature profile of the PEM fuel
cell [14].

Over the past two decades, significant temperature variations in the PEM fuel cell
have been proven, both experimentally and through numerical models [14]. As a
result, it is today standard practice to consider these temperature variations in PEM
fuel cell studies. This is commonly done through computational models of varying
complexity [14, 16, 17]. However, there is a lack of reliable experimental results to
validate these model designs [9, 18]. This is despite the many methods that have
been investigated for measuring the in-situ temperatures of PEM fuel cells [9, 18–
21].

Thermoelectric sensors, such as micro-thermocouples, have been the most common
technologies used for investigating PEM fuel cell temperatures, but they have many
limitations [20–22]. Firstly, they must be electrically isolated which also impacts
the accuracy of their temperature readings [20]. Furthermore, their large diameter
in comparison to the fuel cell components, causes the sensors to interfere with the
cell structure, uniform compression, and overall performance of the fuel cell [18]. In
2009, Lee et al. used a total of seven micro-thermocouples to study the through-
plane temperature distribution of a single PEM fuel cell. However, this study was

limited due to significant modifications made to the cell assembly to accommodate the micro-thermocouples. These modifications included the addition of a double layer of membrane and two sheets of GDL on both the anode and cathode sides.

Optical techniques have also been investigated for studying the PEM fuel cell temperatures during operation [9, 18]. In 2009, Nigel et al. performed in-situ temperature measurements with FBGs embedded into the graphite flow field. The method was deemed successful with a reported error of less than 0.2 °C. They observed a temperature variance of 1 °C between the inlet and outlet gas channels at a current density of approximately 0.4 A/cm^2 [9]. Although they effectively demonstrated FBGs as a viable sensor technology for PEM fuel cells, their method was limited to measuring temperatures at the flow channels and necessitated substantial modifications to the cell housing.

In this thesis, a novel approach for measuring the GDL temperature using optical FBG sensors will be demonstrated on a laboratory PEM fuel cell. In contrast to the measurements conducted by Nigel et al., the suggested method requires no modification to the laboratory fuel cell housing. Instead, it uses an additional GDL to support the optical fiber against bending over the graphite flow fields. Furthermore, a one-dimensional model will be developed based on the laboratory PEM fuel cell, incorporating the measured temperatures as boundary conditions. This approach is valuable for comparison with standard models, which often make the bold assumption of constant temperature at the end of the graphite plate regardless of load. By integrating experimental temperature measurements, this model aims to provide a more accurate representation of the thermal profile within the fuel cell under different operating conditions.

1.4 Background from the Project Thesis

This Master's thesis builds upon the project thesis titled *Optical and traditional detection of thermal balance in green hydrogen systems*, submitted in January 2024 [7]. The foundation for this Master's work was established during the course of this project thesis, implying that certain aspects of the technical background may exhibit resemblances to the project report.

The primary focus of the project thesis was experimental evaluation of the thermal conductivities of PEM fuel cell materials. The thermal conductivities measured for the Nafion membrane and the catalyst layers (CLs), with respect to water content, are integrated into the model cases presented in this thesis. Since the project thesis

is unpublished, this report includes a summary of its findings, the method used, and a brief evaluation for completeness. Consequently, some of these sections may resemble those in the project report. Additionally, the final phase of the project thesis involved initial testing of the optical FBG sensing setup. Both ex-situ calibrations and in-situ measurements at non-operational conditions were conducted. This thesis utilized a new type of optical fiber, necessitating new calibrations. However, the ex-situ calibration results from the project thesis are included in this thesis for comparison.

Chapter 2

Theory

In this chapter, the theoretical background essential for understanding the work of this thesis will be covered. The first section describes the PEM fuel cell in great detail, beginning with the working principles and the characteristics of its multiple-layered components. Furthermore, the thermodynamics of the fuel cell will be examined, highlighting how its irreversibilities contribute to total heat generation, which is a critical concern in PEM fuel cell design. The next section addresses the heat transfer phenomena within a PEM fuel cell, which is the basis for any thermal modeling. This is followed by an explanation of the working principles of optical fiber sensing, with a focus on the optical FBG sensors relevant to this thesis work. Finally, the chapter includes the formulas used for uncertainty calculations.

2.1 Proton Exchange Membrane (PEM) Fuel Cell

2.1.1 Working Principle of PEM Fuel Cells

The fundamental principle of fuel cells is to convert chemical energy into electrical energy, classifying them as electrochemical devices alongside batteries [23]. Fuel cells are similar to batteries in the fact that they utilize electrochemical reactions for electricity generation. Electrochemical reactions involve the transfer of electrons, providing an efficient way to convert chemical to electrical energy [23]. An electrochemical reaction always consists of two half-reactions, one oxidation reaction, and one reduction reaction which occurs simultaneously [24]. An oxidation reaction releases electrons, while a reduction reaction consumes them, and the location at which the oxidation and reduction occur is defined as the anode and cathode respect-

ively. In contrast to batteries, which eventually require recharging or replacement, a fuel cell consistently produces electricity as long as there is a continuous supply of reactants [23]

While various types of fuel cells have been developed, this thesis specifically focuses on the PEM fuel cell. The PEM fuel cell is the most developed due to its distinct advantages over other fuel cell technologies, including higher efficiency, increased power density, and lower operating temperatures [8]. Moreover, the PEM fuel cell has the advantage of zero emissions during operation. By utilizing the electrochemical reaction between hydrogen and oxygen gas, it generates electricity with the only byproducts being heat and water [24].
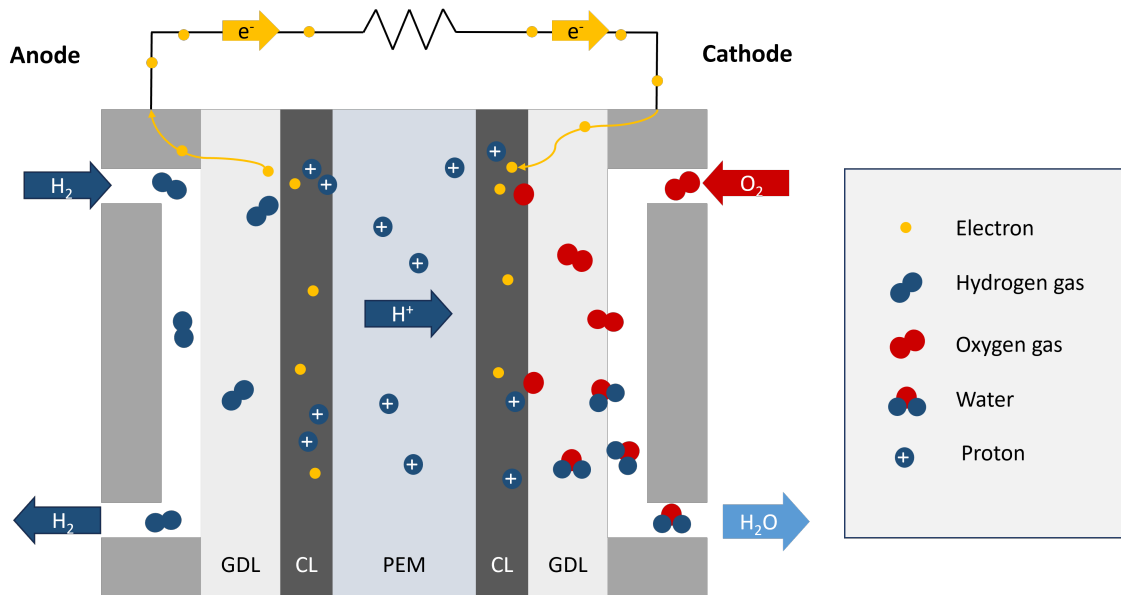
Figure 2.1: Schematic illustration of a single PEM fuel cell with arrows appointing the directions of reactants, protons, electrons, and water [7].

The hydrogen gas is supplied to the anode where it undergoes a Hydrogen Oxidation Reaction (HOR), producing protons (H^+) and electrons (e^-). Meanwhile, the oxygen is supplied to the cathode, either in pure form or air, where it undergoes an Oxygen Reduction Reaction (ORR). The HOR and ORR are expressed in equation (2.1) and (2.2) respectively, while the total electrochemical reaction is expressed in equation (2.3) [25]. Figure 2.1 provides a simplified illustration of a single PEM fuel cell, featuring arrows highlighting the flow of reactants, protons, water, and electrons [7]. As the figure demonstrates, the protons and electrons from the HOR take separate paths to the cathode [23]. The protons are conducted through the membrane, while the electrons are led through an external circuit [7, 24]. Furthermore, the protons and electrons are reunited at the cathode, reacting with oxygen in an ORR [24].

$$2H_2(g) \rightarrow 4H^+ + 4e^- \qquad (2.1)$$

$$O_2(g) + 4H^+ + 4e^- \rightarrow 2H_2O(l/g) \qquad (2.2)$$

$$2H_2(g) + O_2(g) \rightarrow 2H_2O(l/g) \qquad (2.3)$$
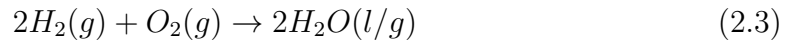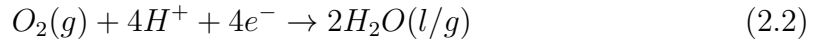
2.1.2 Components of PEM Fuel Cells

The PEM fuel cell is composed of multiple components, including the PEM, the Catalyst Layers (CLs), the Gas Diffusion Layers (GDLs), several gaskets, Bipolar Plates (BPs), Current Collectors (CCs), and end plates [24]. Each of these components has distinct roles and characteristics for a well-functioning fuel cell, which will be covered in this section. A schematic illustration of the layered components of a single PEM fuel cell, along with their associated abbreviations, are given in Figure 2.2.
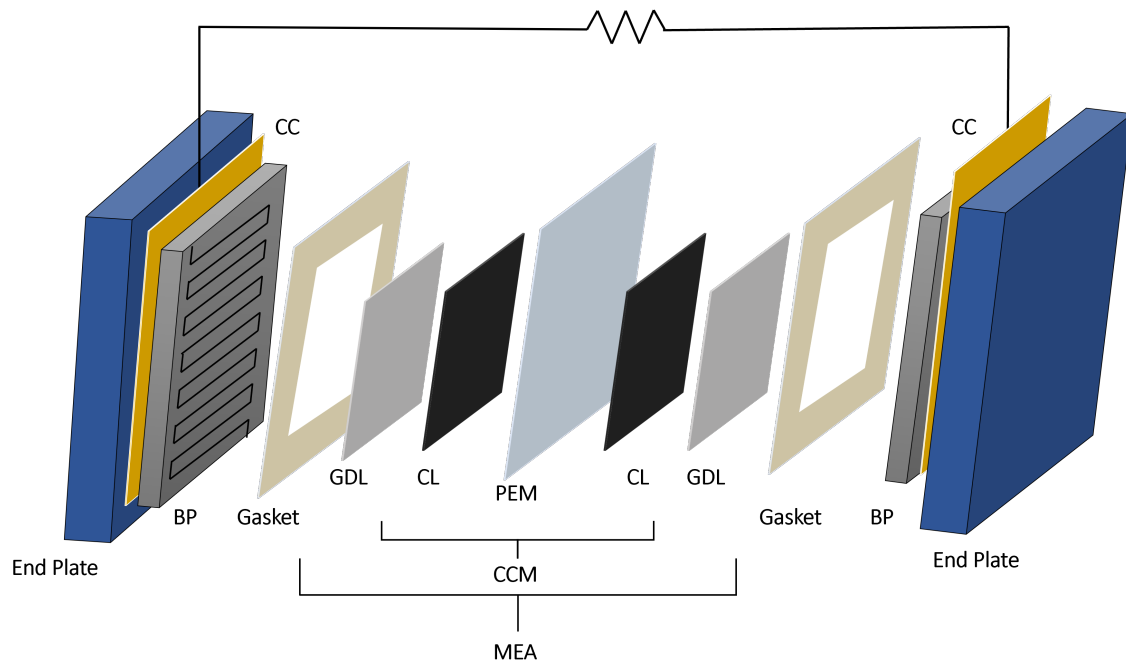
Figure 2.2: Illustration of the layered components of a single PEM fuel cell in the correct order for assembly. The figure also illustrates the layered components that make up the CCM and MEA

The central component of the PEM fuel cell is the membrane. On each side of the membrane is the highly active CL where the half-reactions occur. These are typically coated onto the membrane, forming a Catalyst Coated Membrane (CCM) [6]. Additionally, a GDL is pressed onto each side of the CCM. Together, these form

the Membrane Electrode Assembly (MEA), known as the core of the fuel cell [26]. Specifically, this configuration is referred to as a five-layered MEA, whereas the term three-layered MEA is sometimes used instead of CCM [26]. To avoid confusion, this thesis exclusively employs the term MEA when referring to a membrane with both CLs and GDLs attached, as shown in Figure 2.2.

The Proton Exchange Membrane (PEM)

The PEM is defined by its semipermeable property, which is critical for the functioning of PEM fuel cells. It must be impermeable to the reacting gases and insulate electrons, while still conducting protons [6]. The membrane material most commonly used in PEM fuel cells is Nafion, which has been on the market since the 1960s [27]. Nafion has the key ability to absorb large amounts of water, which enhances its proton conductivity. A typical proton conductivity for a Nafion membrane under normal PEM fuel cell operation is 10 S/m [6]. Another beneficial feature is its mechanical durability, making it possible to be produced as thin films (20-60 μm) resembling household plastic wrap [6, 27].

In more detail, Nafion is a polytetrafluoroethylene (PTFE) polymer equipped with sulfonic active groups (SO_3^-). These functional groups attract water and cluster within the material, leaving hydrated regions in the membrane [27]. The membrane can retain up to 22 water molecules per sulfonic group when fully humidified with liquid water. However, this value decreases by nearly 50% when the membrane is humidified with vapor [6]. These humidified regions function as proton conductive pathways due to their weak attraction to SO_3^- [27]. The larger these hydrated regions are, the easier the H^+ move through the membrane, enhancing its conductivity [27]. Hence, sufficient membrane humidification is essential for optimal fuel cell performance. This is done through conditioning, also referred to as the MEA break-in.

The Catalyst Layers

The two CLs are three-dimensional porous structures with complex roles in the PEM fuel cell. These layers have to facilitate the electrochemical half-reactions while transporting electrons, protons, reactants, and products [28]. To form the CL, a porous structure is made out of small carbon particles covered with even smaller platinum nanoparticles and mixed with pieces of membrane material [6]. This mixture is then generally coated onto the membrane. While the membrane material is added to the CL mixture for proton conduction, the platinum particles

are added as the catalyst for the HOR and OOR [27]. This production method is ideal as it minimizes the use of costly catalyst material while allowing for a three-phase contact between membrane, reactants, and catalyst [27].

The Gas Diffusion Layers and Microporous Layers

The next part of the electrodes is the GDL. The GDLs are located at each side of the CCM to complete the MEA. They are porous layers, either made of carbon cloth or carbon paper [27]. One of its critical roles is to lead away produced water to allow for the transport of reactant gases to the CL [6]. Enhanced water removal by the GDL is generally achieved through PTFE treatment [27]. Other functions of the GDL include diffusing gases and conducting electrons between the CL and the bipolar plate [27].

It is common practice to spray an even finer distribution layer to the side of the GDL that is in direct contact with the CL [6]. This layer is commonly referred to as the microporous layer (MPL) and is proven to significantly improve the performance of the PEM fuel cell [6]. The MPL is made of carbon particles and PTFE and has similar roles to the GDL. It distributes the gases, conducts electrons, and removes water [6]. Additionally, it improves the contact with the CL [24].

The Bipolar Plates

The reactant gasses are supplied to the GDLs from flow channels engraved into graphite plates. A standard single PEM fuel cell, as depicted in Figure 2.1, produces below 1 V [24]. Hence, assembling several cells in series to reach a useful voltage is standard practice. This is done using BPs, which feature flow channels on both sides for connecting neighboring cells [6]. They have hydrogen gas flowing on one side and oxygen flow on the other [6]. An illustration of a small PEM fuel cell stack can be seen in Figure 2.3. In addition to distributing the reactants, the bipolar plates remove water, give mechanical support, and conduct electricity [24]. Moreover, the bipolar plates may also feature internal cooling channels for effective heat management [29].

Gaskets

Finally, sealing gaskets are added around the MEA for safety reasons, as they are essential for ensuring a leakage-free fuel cell [27]. These are commonly made out of silicon rubber.
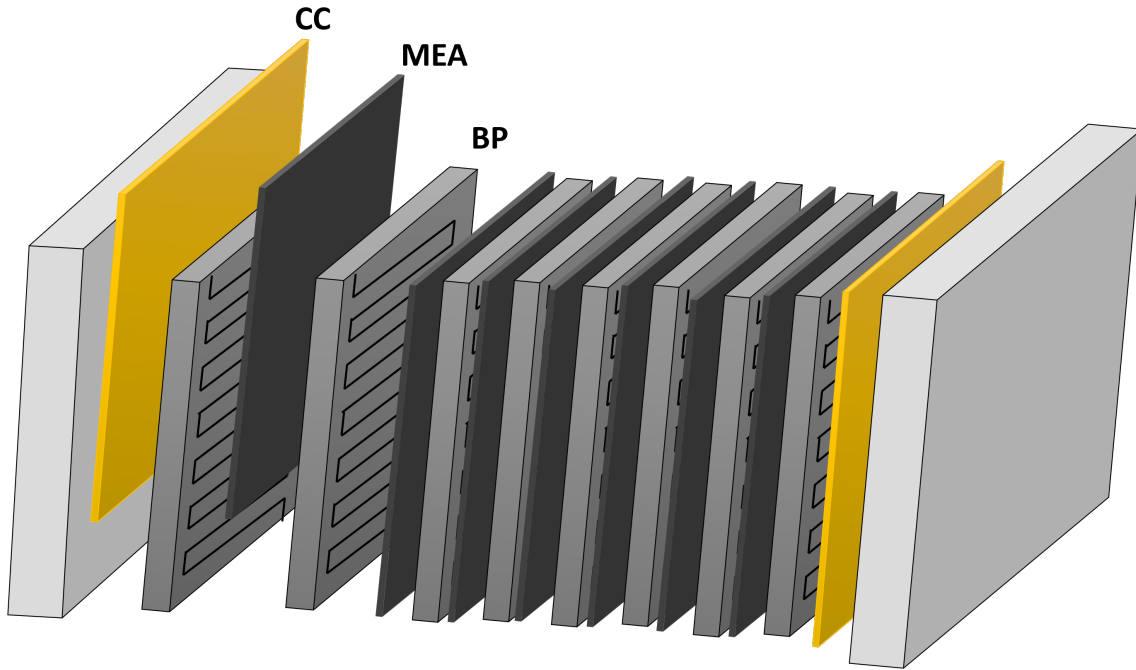
Figure 2.3: Illustration of how several PEM fuel cells are assembled into a stack with BPs separating individual MEAs.

2.1.3 Thermodynamics of PEM Fuel Cells

Engineering energy storage using hydrogen systems requires a fundamental understanding of electrochemistry, given that it relies on the energy conversion between electrical and chemical energy [30]. Hydrogen production is achieved through water electrolysis, where electrical energy is transformed into chemical energy carried by the produced hydrogen. Subsequently, PEM fuel cells are employed to reconvert the chemical energy back into electrical energy [6]. These energy conversion processes are not without losses, which must be accounted for when discussing their efficiencies [30]. Additionally, these losses generate significant heat, creating challenges for systems that lack adequate heat management [8]. This section will cover the necessary fuel cell thermodynamics to understand the losses in PEM fuel cells, as well as the associated heat generation.

The total energy converted in the PEM fuel cell is given by its reaction enthalpy, ΔH, which is equal to the enthalpy difference between the reactants (H_2 and O_2) and the products (H_2O) [7, 30]. When assuming reversible conditions, the reaction enthalpy is a function of the reversible work and the reversible heat. Furthermore, the reversible work from chemical reactions is also known as Gibbs free energy ΔG, and the reversible heat can be expressed as the product of the entropy change ΔS and temperature T [30]. Hence, the reaction enthalpy can be expressed as follows

$$\Delta H = W_{rev} - Q_{rev} = \Delta G + T\Delta S. \tag{2.4}$$

Furthermore, Gibbs free molar energy is related to the reversible electrochemical cell potential, E_{cell}^{rev}, and can be expressed as

$$\Delta \overline{g} = \Delta \overline{h} - T\Delta \overline{s} = -nFE_{cell}^{rev}, \tag{2.5}$$

where n is the amount of charge per reactant and F is Faraday's constant [30]. For the electrochemical reaction in a PEM fuel cell, n = 2, as two moles of electrons are transferred when oxidizing one mole of hydrogen into protons [30].

After calculating Gibbs free molar energy, one knows the potential electric work for reversible conditions. However, a reversible condition only occurs at equilibrium, which is not the case for a fuel cell with a net current flow [30]. Hence, the energy conversion within a PEM fuel cell is not without losses. These irreversibilities add to the heat generation as the entropy production increases [30]. Therefore, it is crucial to include irreversibilities when discussing the temperature distribution within the PEM fuel cell.

Firstly, there are ohmic losses in the PEM fuel cell. These losses occur due to the friction encountered by the protons as they travel through the membrane, as well as the friction encountered by the electrons when transferred between the CLs and current collectors [31]. The drop in potential due to ohmic losses is calculated from Ohm's law as the product of the area-specific resistance r and the current density j [31].

Secondly, there are activation losses related to the slowness of reactants at the surface of the CLs. These losses cause some of the generated voltage to be lost driving the chemical reaction [25]. This is called the activation overpotential, η_a, and is commonly modeled by the Tafel equation with the following form

$$\eta_a = a + b\log(j), \tag{2.6}$$

where a and b are the Tafel coefficients. The Tafel equation is an approximation that only holds for higher current densities but is sufficient when considering fuel cell technologies. Furthermore, there are concentration losses caused by the change in the concentration of reactants at the electrode surface [31]. Their contribution to the drop in potential is called the concentration overpotential, η_c. It is also in

some cases called the "Nernstian" loss as it is modeled by the Nernst equation. The concentration overpotentials are

$$\eta_{c,H_2} = -\frac{RT}{2F}ln(1 - \frac{j}{j_l}), \tag{2.7}$$

and

$$\eta_{c,O_2} = -\frac{RT}{4F}ln(1 - \frac{j}{j_l}), \tag{2.8}$$

for the hydrogen and oxygen reactants respectively. The j_l parameter is a postulated limiting current density where the reactants are used at the same rate it is consumed [31]. It can be seen that the concentration overpotential increases with the current density as the PEM fuel cell fails to transport sufficient reactants to the electrode [31].

Additional losses can occur from fuel crossover and internal currents, which are fuel transport and electron conduction through the electrolyte. However, these are usually sufficiently small, and their effect is commonly not considered [31]. Consequently, the actual cell potential when accounting for the three main loss terms can be expressed as

$$E_{cell}(j) = E_{cell}^{rev} - rj - \eta_a(j) - \eta_c(j), \tag{2.9}$$

where r is the sum of all electrical and ionic resistances. Figure 2.4 summarizes the fuel cell thermodynamics, as well as the effect of irreversibilities. The figure also shows how irreversible heat generation comes in addition to reversible heat and reduces the cell potential [30].
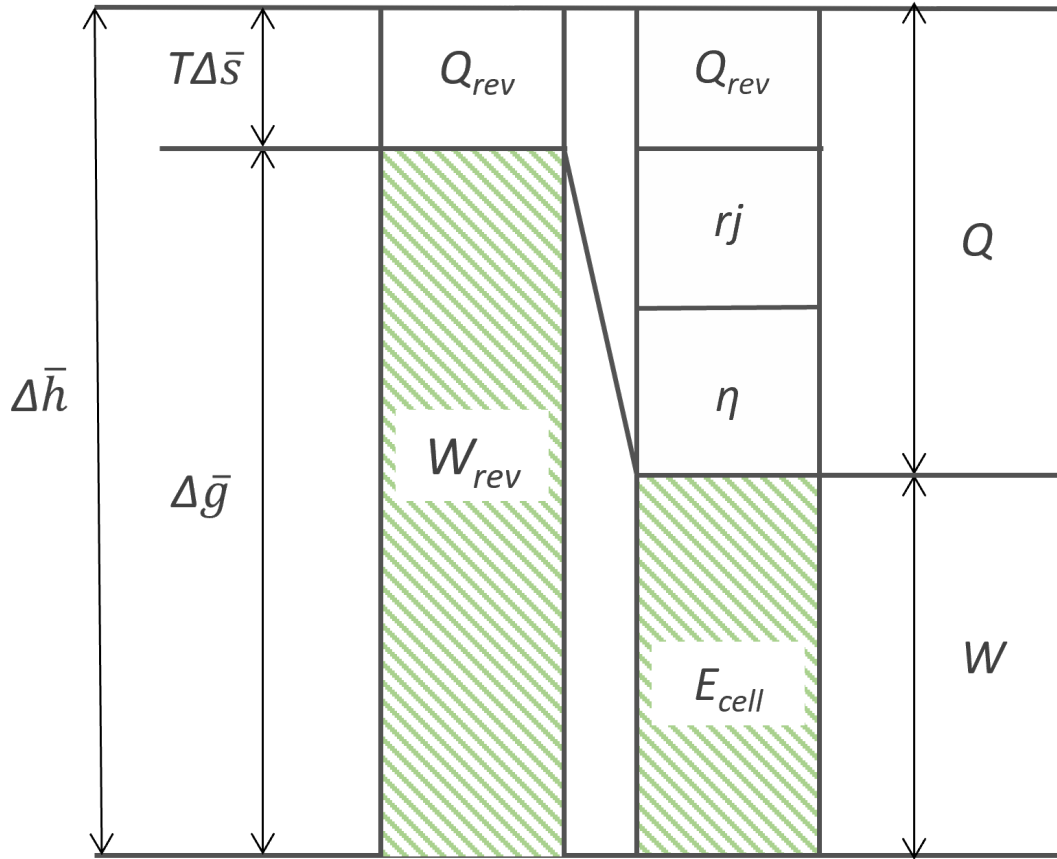
Figure 2.4: Visualizations of the thermodynamic relations and the effect of irreversibilities on the total heat generation. The illustration is a recreation of Figure 6.1 in the book *Engineering Energy Storage* by Burheim [30].

One common tool to evaluate the performance of a specific fuel cell is to calculate the energy efficiency ε_{eff}, which is given as

$$\varepsilon_{eff} = \frac{E_{cell}(j)}{E_{cell}^{rev}} \qquad (2.10)$$

where E_{cell} is the actual measured cell potential and E_{cell}^{rev} is the reversible cell potential [30]. In addition to energy efficiency, polarization curves are a widely used tool to evaluate fuel cell performance [23, 32]. A standard polarization curve for a PEM fuel cell can be seen in Figure 2.5. It is either created by recording the voltage for a series of set current densities or by recording the current density for a series of set voltages [32]. The measured I-V relation is then plotted to form the polarization curve. This curve is particularly useful as it visualizes the losses with respect to the current density j. As seen from Figure 2.5, the fuel cell losses increase with increasing current density as one moves further away from equilibrium [30]. The curve also marks the three regions of voltage drop in a PEM fuel cell, corresponding

to the three loss terms: activation losses, ohmic losses, and concentration losses [23].
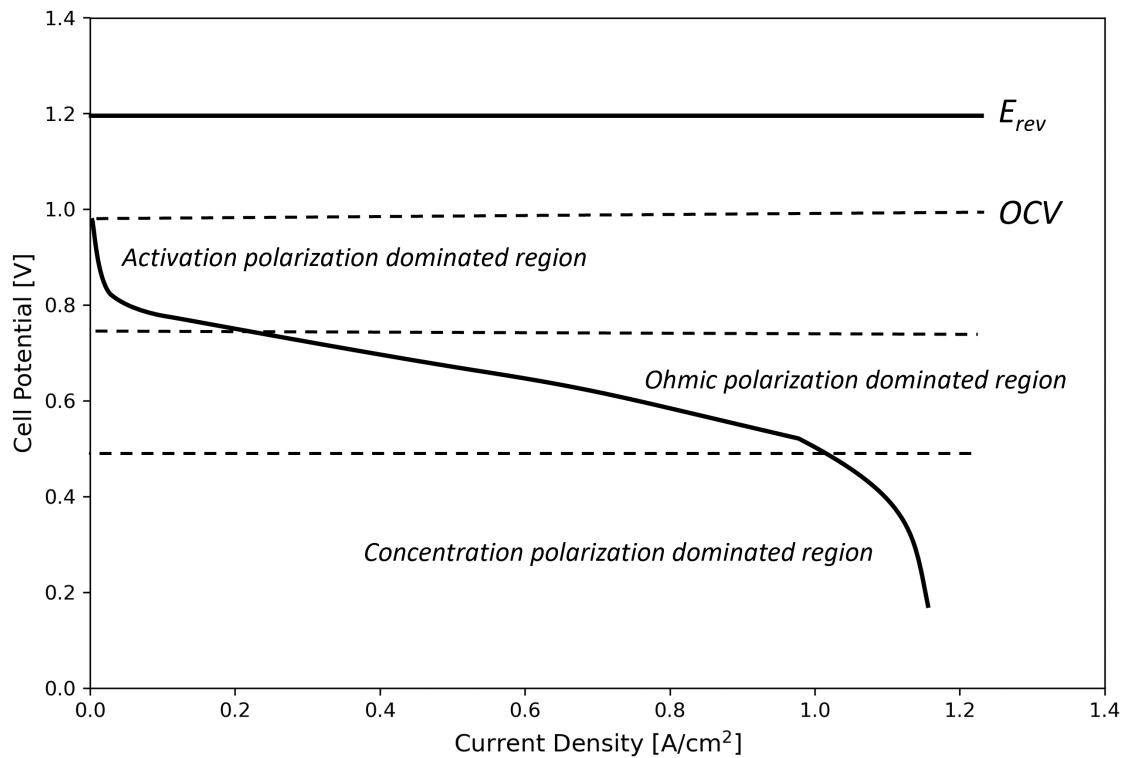
Figure 2.5: Generalized polarization curve for PEM fuel cells with polarization regions.

The power curve is another graph commonly created alongside the polarization curve and is calculated from the previous results by multiplying the voltage and current [30]. The plot is useful to know the fuel cell power output for each current density and the maximum power output. A typical power curve is shown in Figure 2.6. For smaller current densities the power output grows close to linearly before it curves and moves towards the maximum power output for higher current densities.
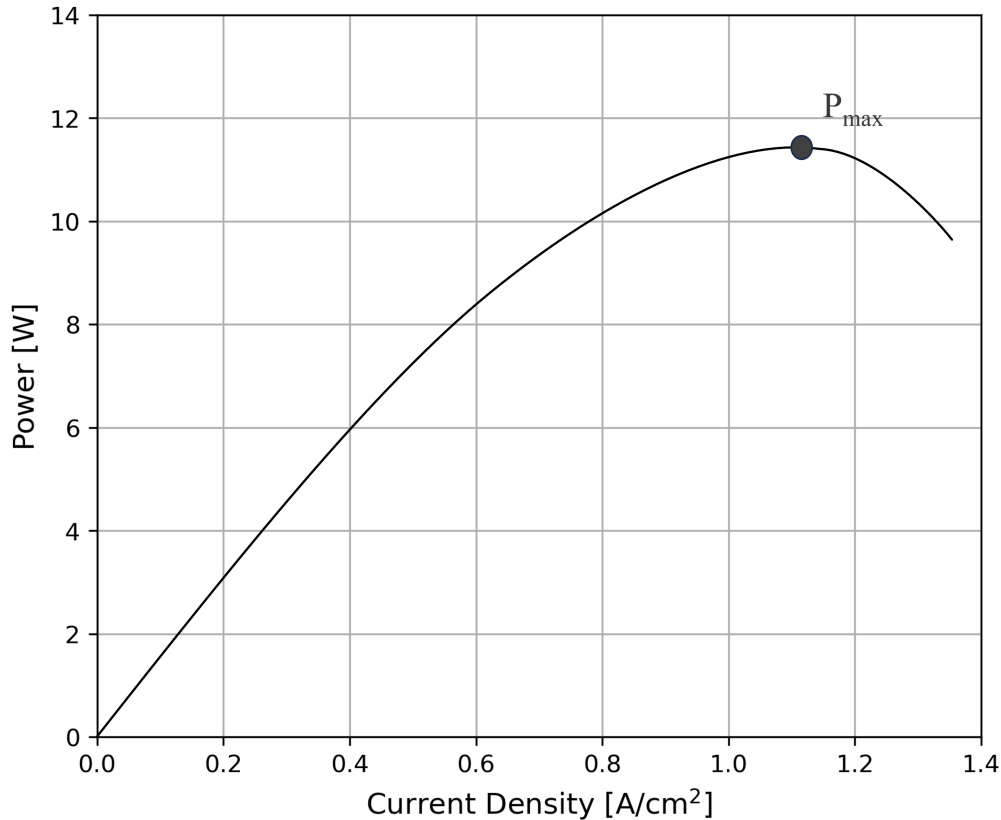
Figure 2.6: Generalized power curve for PEM fuel cells.

2.1.4 Importance of Temperature in PEM Fuel Cells

The temperature has a significant impact on the PEM fuel cell performance, affecting electrochemical reactions, mass transport, and overall efficiency [8]. Upon examining the impact of irreversibilities in Section 2.1.3, it becomes apparent that a significant amount of heat is generated during operation. Hence, proper heat management is one of the biggest challenges in PEM fuel cell designs [9]. Further adding to the challenge is the uneven distribution of the heat sources, causing temperature variations within the PEM fuel cell [8]. Hence, both the heat sources and the resulting temperature distribution within the PEM fuel cell have been, and continue to be, a topic of investigation. To underline the importance of heat management, this section will summarize the consequences of operating the cell at temperatures outside the recommended range.

The ideal operating range for low-temperature PEM fuel cells lies between 60 and 80 °C [8]. Given the narrow temperature range, there is a constant risk of overheating the cell without effective heat regulation [6]. Overheating is one of the main operational concerns, due to the large heat sources present during operation. One

significant consequence of operating beyond the temperature window is an accelerated degradation rate of both the membrane and the CLs, ultimately affecting the cell's lifespan [8]. Furthermore, exceeding 85 ℃ increases the risk of membrane dehydration. A dehydrated membrane exhibits reduced proton conductivity, affecting the overall performance of the PEM fuel cell [8]. Therefore, maintaining the temperature below 85 ℃ is important for optimal performance.

However, this is a delicate balance, as performance improves with temperature increases up to 80 ℃ [8]. Therefore, excessive cooling of the PEM fuel cell is also not ideal. Excessive cooling of the PEM fuel cell introduces its own set of challenges, including electrode flooding. Electrode flooding is the term used when water accumulates in the cell, hindering mass transport of reactants [33]. Moreover, lower temperatures correspond to decreased reaction rates, further affecting performance [8]. Overall, a good heat management system is able to effectively cool the cell to prevent overheating, without decreasing the temperatures more than necessary. Such a system is key for a long-lasting and well-performing PEM fuel cell [8].

2.2   Heat Transfer

Section 2.1.3 discussed the heat production associated with the energy conversion process occurring in the PEM fuel cell. This heat is transferred through the layered materials of the PEM fuel cell, resulting in internal temperature variations [8]. This thesis aims to simulate the temperature variations in a single PEM fuel cell through numerical modeling. However, to accurately model the temperature distribution of the PEM fuel cell, it is essential to grasp the nature of heat transfer. Therefore, this section will provide the theoretical background needed to understand heat transfer in a PEM fuel cell.

2.2.1   Modes of Heat Transfer

Heat transfer is the transport of thermal energy caused by a spatial temperature difference, where the heat always moves from the hotter to the colder region [34]. When discussing heat transfer, there are three primary processes, often referred to as modes of heat transfer. These are conduction, convection, and radiation [34]. When discussing heat transfer in the PEM fuel cell, the effect of radiation is negligible compared to conduction and convection and will therefore not be covered in this theoretical background.

Conduction

Conduction is the transfer of heat through a stationary medium with temperature gradients [34]. The heat transfer by conduction can be explained at a molecular level, as higher temperatures are related to higher molecular activity. When a stationary medium is subject to a temperature variation, the molecular activity of the medium varies. For gases and liquids, this yields a transfer in molecular energy by collision and diffusion. For a solid, however, the molecular energy is transferred by the mitigation of electrons and lattice vibrational waves [34].

The heat transfer by conduction is quantified by Fourier's law. For one-dimensional heat transfer in an isotropic material, Fourier's law is given as

$$q_x'' = -\kappa \frac{dT}{dx},$$

(2.11)

where q_x'' is the heat flux defined as the rate of heat per unit area. Defined by Fourier's law, the heat flux is proportional to the temperature gradient and normal to the isothermal surface [34]. Furthermore, the proportionality constant κ is defined as the thermal conductivity given in units W/mK. The thermal conductivity is characteristic of the medium and describes its ability to conduct heat [34]. This varies greatly between different materials. As the PEM fuel cell is a multilayered device, each layer will have a separate thermal conductivity κ that must be known to determine the temperature profile of the PEM fuel cell. Furthermore, the thermal conductivity is not constant, but varies with temperature, pressure, and purity [34]. For many homogeneous mediums, the thermal conductivity is tabulated as a function of the temperature. If not, one must find it experimentally, as was done for the Nafion membrane and the CCM in the project thesis [7].

Convection

Convection is another mode of heat transfer, covering the transfer of heat between a stationary medium and a moving fluid [34]. Convection is classified as natural convection or forced convection, depending on the nature of the fluid flow. For forced convection, the fluid is driven by external forces, such as fans or wind, while the flow is induced by buoyancy forces for natural convection [34]. Either way, the heat flux for convection is given by Newton's law of cooling

$$q'' = h_{conv}(T_s - T_\infty),$$

(2.12)

where T_s is the temperature of the surface area and T_∞ is the temperature of the free flow fluid [34]. Furthermore, h is the convection heat transfer coefficient in units $W/m^2 K$. The heat transfer coefficient, h, is governed by the boundary layer of the fluid flow [34]. From the no-slip boundary condition, it is given that the velocity of a fluid flowing past a stationary surface will be zero at the surface (y=0). Consequently, the surface heat transfer will occur by conduction. By combining Newton's law of cooling with Fourier's law, an expression for the heat transfer coefficient h is found as

$$h_{conv} = -\kappa_f \frac{\partial T/\partial y \mid_{y=0}}{T_s - T_\infty}, \tag{2.13}$$

where κ_f is the thermal conductivity of the fluid [34].

2.2.2   Thermal Resistance

For all modes of heat transfer, one can find the thermal resistance in units K/W. The thermal resistance for conduction and convection is expressed in equations (2.14) and (2.15) respectively. This is often done for complex heat transfer systems as it can be represented as an equivalent thermal circuit in a similar manner as electric circuits [34]. Circuit representation is often useful for systems with different thermal conductivities and/or modes of heat transfer to conceptualize and quantify the heat transfer problem [34]. The layered materials making up a PEM fuel cell, for example, can be represented as a series of thermal resistances in a thermal circuit.

$$R_{th,conduction} = \frac{\Delta x}{\kappa A} \tag{2.14}$$

$$R_{th,convection} = \frac{1}{hA} \tag{2.15}$$

For a system with conduction through layered components, as for the PEM fuel cell, thermal resistance will also be present at their interface. This is called contact resistance and is caused by the materials' surface roughness, creating small fluid-filled gaps between them [34]. A common method to reduce contact resistance is through applied compaction pressure, which is essential in PEM fuel cells to enhance both thermal and electrical conductivity.

Besides reducing contact resistances, applied compaction pressure also decreases the thermal resistance of the porous layers within the PEM fuel cell. The thermal resistance in porous media is influenced by the thermal properties of its solid and the occupying fluid [34]. In a PEM fuel, the occupying fluids are air/oxygen, hydrogen,

and/or water. Hence, the effective conductivity of the porous material is defined by the solid-to-fluid ratio, where the solid generally holds a higher thermal conductivity than the fluid. Applied compaction pressure will reduce the fluid ratio, and consequently reduce the thermal resistance of the porous media. However, the downside is that higher compaction pressures will eventually limit mass transport in the porous layers, which is crucial for operation [13]. Therefore, a trade-off between mass transport and conductivity must be found when choosing the compaction pressure [13]. Another way of reducing the thermal resistance in porous materials is by replacing gases like air with liquids of higher thermal conductivity, such as water [34]. This partially explains the improved thermal conductivities observed in PEM fuel cell materials when sufficiently humidified.

2.3 Optical Sensors

Optical sensors exploit the behavior of light and its interaction with matter to measure external factors [35]. They are microscopic sensors capable of measuring various parameters, such as temperature, strain, humidity, pressure, and concentrations [36]. In recent years, they have been a topic of discussion in the electrochemical industry due to their beneficial characteristics [8–10]. Electrochemical devices have a harsh and chemically reactive environment, which is a challenging working environment for most sensing technologies. Optical fibers, however, stand out as they are made of chemically inert glass and are resistant to electromagnetic interference [10]. This section will cover the theoretical background necessary to understand the working principle of optical fibers. Furthermore, a more detailed description of Fiber Bragg Grating (FBG) sensors will be included as they are the specific fiber technology to be used in this thesis work.

2.3.1 Introduction to Fiber Optics

Optical fibers utilize the phenomena of total internal reflection to guide light through its core [35]. An illustration of an optical fiber with total internal reflection is given in Figure 2.7. To understand the phenomena of total internal reflection, one first needs to understand the refractive index of materials and the behavior of light at the interface of two mediums. First, the refractive index of a material, n, characterizes how light propagates through the material [37]. It is defined as

$$n = \frac{C_0}{C},\qquad(2.16)$$

where C is the velocity of light in the medium and C_0 is the velocity of light in a vacuum [37]. The refractive index is tabulated for most common mediums and will always be greater than one as light travels at a slower velocity for all other mediums than vacuum [37].
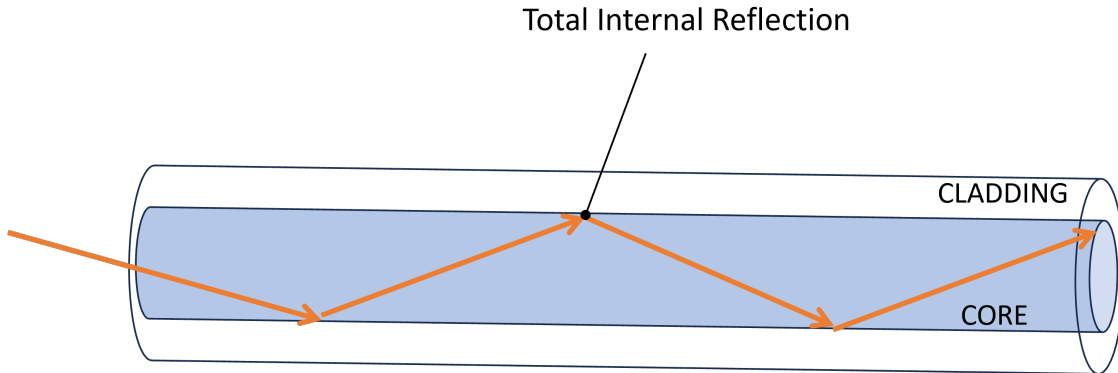
Figure 2.7: Illustration of total internal reflection through the core of an optical fiber.

Furthermore, the behavior of light between two mediums is a function of their refractive index. Light at the interface between two mediums can either be reflected, refracted, or both. If reflected, the light will return to the initial medium with an angle of reflection equal to the angle of incidence. The refracted light, however, will penetrate the interface and be bent due to the change in refractive index [37]. The refraction of light is illustrated in Figure 2.8a for the case of light moving to a medium of lower refractive index. This is mathematically expressed by Snell's law as

$$n_1 sin(\theta_1) = n_2 sin(\theta_2),\qquad(2.17)$$

for light moving from medium 1 at an angle of incidence θ_1 to medium 2 at an angle of refraction θ_2. The angle of incident that yields a 90-degree angle of refraction is defined as the critical angle as demonstrated in case (b) of Figure 2.8. As soon as one exceeds this critical angle, total internal reflection is obtained [37]. Total internal reflection is illustrated in case (c) of Figure 2.8 and in Figure 2.7. This phenomenon is ideal for optical fibers as the light can travel for long distances due to minimal optical losses [37]. Total internal reflection only occurs when moving from a higher to a lower refractive index. Hence, optical fibers achieves total internal reflection by

having a higher refractive index core with a lower refractive index cladding [37].
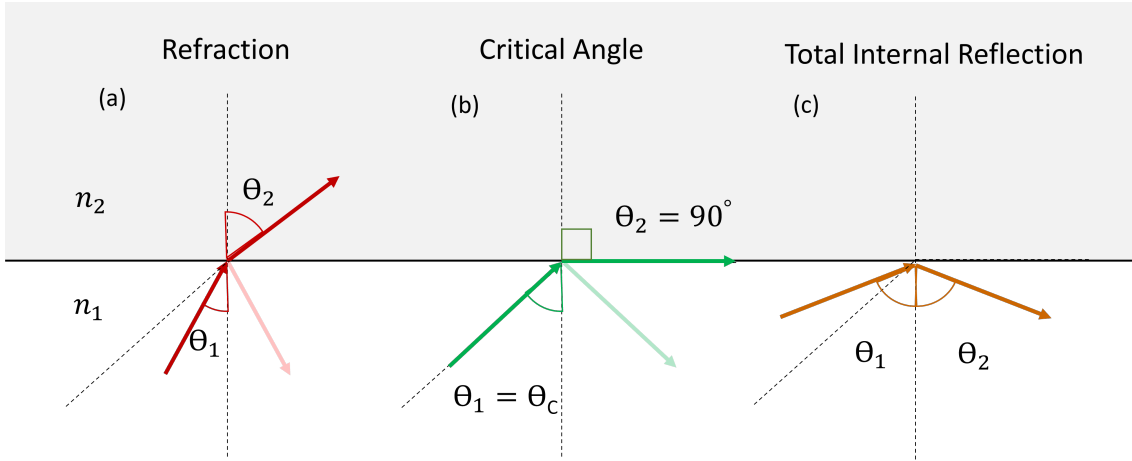
Figure 2.8: Illustration of how the behavior of light changes with angle of incidence, θ_1, at the interface of two materials with different indexes of refraction. n_1 and n_2 are the indexes of refraction of the two interfacing materials, whereas $n_1 > n_2$ for the depicted scenario.

2.3.2 Fiber Bragg Grating (FBG) Sensors

There exist various types of optical fiber technologies suitable for sensing a range of different parameters [35]. For temperature sensing in electrochemical devices, optical FBG sensors have been recognized [8–10]. FBGs are increasing in popularity due to their inherent characteristics. Amongst these characteristics are their microscopic scale, their chemically inert nature, and their resistance to electromagnetic interference, which are qualities shared among all types of optical fibers [10]. However, FBGs also hold additional qualities. These are a high sensitivity to external changes and a long-term reliability [10]. In this thesis work, FBGs will be used to obtain in-situ temperature measurements of a PEM fuel cell. Hence, this specific optical sensing technology will be covered in more detail.

Optical FBG sensors are an optical fiber technology specifically used for strain and temperature measurements [35]. The gratings are inscribed into the optical fiber using UV light, resulting in a periodic change in the refractive index of the core [10]. Furthermore, the gratings are inscribed with a set grating period Λ, resulting in a high reflectivity of one specific wavelength. This wavelength is called the Bragg wavelength, λ_B, and is expressed as follows

$$\lambda_B = 2n_{eff}\Lambda, \tag{2.18}$$

where n_e is the effective refractive index of the grating [10].

Figure 2.9 depicts an optical fiber integrated with two FBG sensors. Furthermore, the figure illustrates how only a narrow range of wavelengths, centered at λ_B, is reflected from each FBG for a broadband spectrum input. Measuring the reflected Bragg wavelength is the basis of FBG sensors, as it is sensitive to changes in temperature and strain [10]. The strain response on an FBG is due to changes in the grating period Λ, which shifts the reflected Bragg wavelength as seen by equation (2.18). The temperature response, however, is mainly due to changes in the effective refractive index n_{eff} with temperature. This is called the thermo-optic effect [10]. Approximately 95% of the temperature response of an FBG is tied to the thermo-optic effect. However, 5% of the temperature response is due to changes in the grating period by thermal expansion [38]. Due to the limiting role of thermal expansion, it is often neglected.
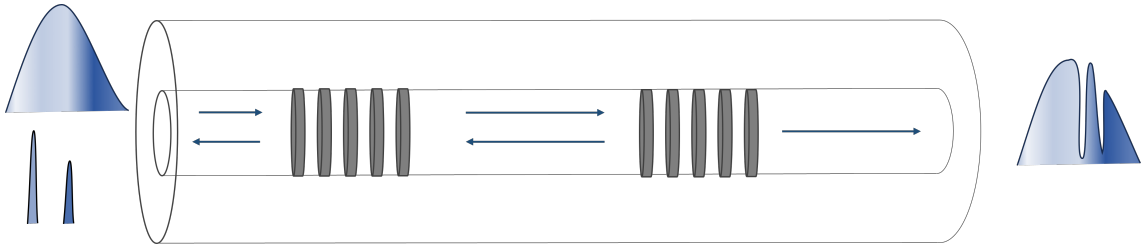
Figure 2.9: Schematic of inscribed FBGs into the core of an optical fiber and the reflected Bragg wavelengths for a broadband input signal.

An optical fiber can have several FBGs centered at different Bragg wavelengths. Hence, external changes can be measured at multiple points downstream of the fiber [38]. These shifts in reflected Bragg wavelengths are either detected by the reflected or transmitted spectrum, before translated into changes in temperature or strain [38]. When using FBGs for temperature measurements, one usually assumes constant or negligible strain as it is difficult to separate the two. Under the assumption of negligible strain, most FBGs have a temperature sensitivity of 10 pm per °C [10]. A mathematical expression for the shift in reflected Bragg wavelength is given as

$$\Delta\lambda_B = 2n_{eff}\Lambda(0.78\varepsilon + (\alpha + \frac{dn_{eff}}{dT})\Delta T), \tag{2.19}$$

where ε is the strain, α is the thermal expansion coefficient and $\frac{dn_e}{dT}$ is the thermo-optic coefficient [35, 38].

2.4 Uncertainty Calculation

Experimentally derived data will always hold a certain amount of uncertainty. Hence, it is essential to document the level of uncertainty tied to the published results. In this thesis, experimental measurements were obtained over a specific dwell time for each state under consideration. The mean of the measure values x was calculated over the dwell time to obtain the final result. The mean value $\overline{x}$ is found using the following formula

$$\overline{x} = \frac{1}{N} \sum_{i=1}^{N} x_i, \tag{2.20}$$

where N is the total number of measurements done over the dwell time. The uncertainty associated with this approach is represented by twice the standard deviation [39], where the standard deviation is given as follows

$$S_x = \sqrt{\frac{\sum_{i=1}^{N} (\overline{x} - x_i)^2}{N}}. \tag{2.21}$$

When a result x is derived from a series of experimental measurements (A, B, C), it is essential to include the standard deviations of all the measurements in the uncertainty calculation. This process is known as the propagation of error and is defined as

$$S_x = \sqrt{\frac{\partial x}{\partial A} S_A^2 + \frac{\partial x}{\partial B} S_B^2 + \frac{\partial x}{\partial C} S_C^2}, \tag{2.22}$$

where S_A, S_B, and S_C are the standard deviations of A, B, and C respectively [39].

Chapter 3

Method

Upon laying the fundamental theoretical background needed in Chapter 2, this next chapter goes on to explain the methods employed to achieve the thesis objectives. First, section 3.1 provides a summary of the experimental method used to measure thermal conductivities in the project thesis, ensuring completeness for the reader. Next, section 3.2 details the approach taken for acquiring in-situ temperature measurements using the optical FBG sensor. This section also covers the experimental setup and preparatory steps taken, such as the FBG calibrations and the conditioning of the MEA. Finally, section 3.3 outlines the design of the one-dimensional model developed to simulate the temperature profile of the PEM fuel cell based on the experimental data.

3.1 Ex-Situ Thermal Conductivity Measurements

Designing an accurate model for a PEM fuel cell's temperature distribution requires knowing the thermal characteristics of its constituent materials. Given that conduction is the primary heat transfer mode, the thermal conductivity of each layered material in the PEM fuel cell is critical. In recent years, many researchers have been investigating the thermal properties of PEM fuel cell material through various experimental approaches. Notably, in 2010 Burheim et al. published an ex-situ measurement method for finding the through-plane thermal conductivity of different materials [11]. In the project thesis, which this Master's thesis is a continuation of, an approximately equal approach as represented by Burheim et al. was utilized to determine the thermal conductivity of PEM fuel cell materials. This was done using a measurement rig at the Varmeteknisk laboratory at NTNU Trondheim. The materials tested were a Nafion 211 membrane and a CCM at dry and fully humidified

conditions. The specific CCM used was a 11210 MEA from Baltic FuelCells with the GDLs removed. Since the findings from this experiment significantly influence the simulated temperature profiles in this thesis, this section offers a concise summary of the experimental setup and method used to determine the thermal conductivities.

3.1.1   Experimental Setup

The measurement rig utilized in the project thesis was developed to find the thermal conductivity of a material sample based on Fourier's first law of heat conduction. The basis of the method was to measure both the temperature drop over a material sample and the one-dimensional heat flux to calculate the sample's thermal resistance. This was done using the rig illustrated in Figure 3.1, specifically designed to supply the sample material with an approximately constant one-dimensional heat flux. The material sample was positioned between two steel rods, subject to a temperature variation induced by running chilled and heated water through the bottom and top rod respectively. Furthermore, the steel rods and sample layer were insulated in the radial direction to limit any radial heat flux during testing.

Six thermocouples were integrated into the steel rods to calculate the heat flux. Moreover, two additional thermocouples were incorporated into two aluminum caps placed at the end of the rods facing the sample. The point of the two aluminum caps was to provide an approximately isothermal layer on each side of the sample caused by the high thermal conductivity of aluminum. Therefore, the temperature drop over the material sample could be assumed to be equal to the temperature difference between the two thermocouples at the aluminum caps.

The measurement rig was also equipped with a pneumatic piston to supply the material sample with a series of clamping pressures. The pressures and their respective sampling time were set by the user in an associated LabView program. The front panel of the Labview program is seen in Figure 3.2. The rig was also equipped with two micrometers on each side, as seen in Figure 3.1, to measure sample thickness and sample compression for various clamping pressures.
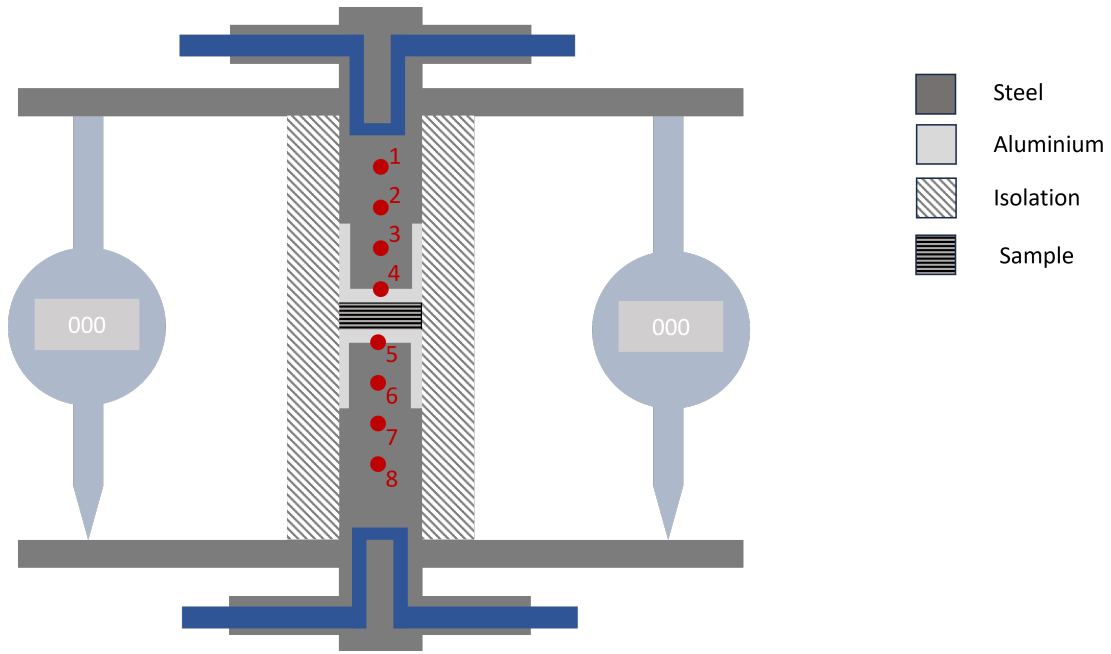
Figure 3.1: Illustration of the thermal conductivity measurement rig with its eight thermocouples marked and numbered in red.

3.1.2 Thermal Conductivity Calculation

Accompanying the measurement rig was a Matlab program designed to compute the respective thermal conductivities using the recorded temperatures and thicknesses. This calculation followed Fourier's first law, as outlined in equation (2.11), to determine the total thermal resistivity across the sample, expressed as

$$r_t = \frac{T_4 - T_3}{q''_{mean}}, \tag{3.1}$$

in units Km^2/W, where q''_{mean} is the mean heat flux through the steel rods. To find the mean heat flux, the associated LabView program, seen in Figure 3.2, uses the integrated thermocouples to calculate the heat flux in the top and bottom rods as

$$q''_{1-3} = \kappa_{ss} * \frac{T_1 - T_3}{L_{1-3}}, \tag{3.2}$$

and

$$q''_{6-8} = \kappa_{ss} * \frac{T_6 - T_8}{L_{6-8}}, \tag{3.3}$$

respectively, where κ_{ss} is the thermal conductivity of the steel rod. Ideally, these heat fluxes would be equal but were generally seen to have a deviation between 2-5%

during testing [7].
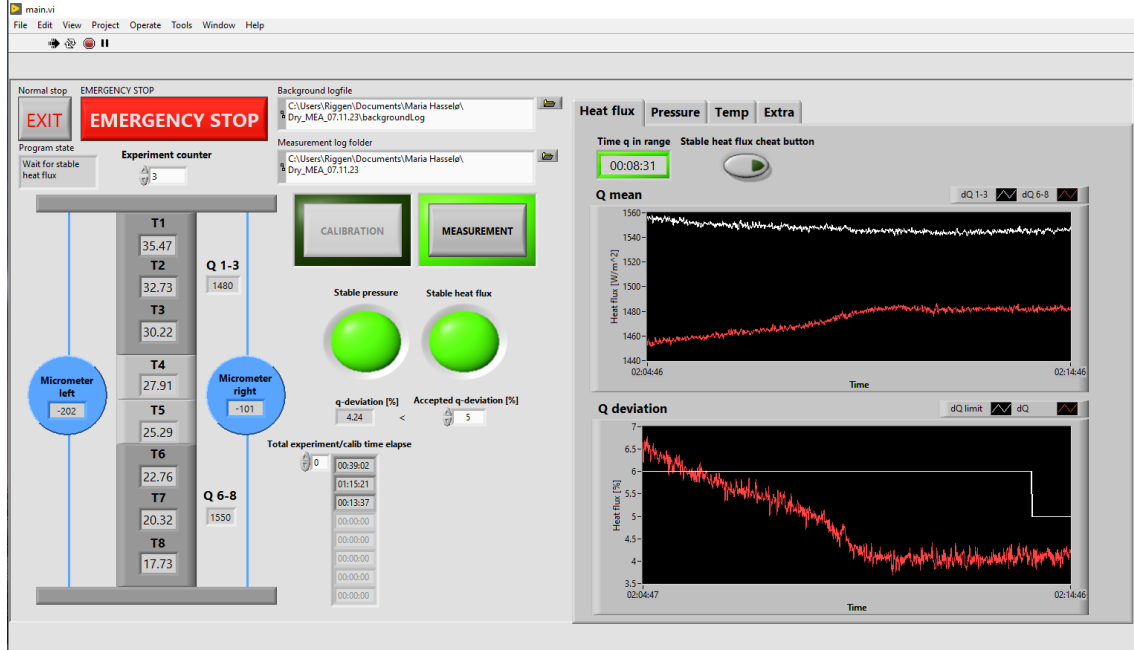
Figure 3.2: Image of the LabView program's front panel, used to operate and monitor the thermal conductivity measurement rig.

Moreover, the total thermal resistance r_t in equation (3.1), could be expressed as a sum of the sample thermal resistance and its contact resistance with the aluminum caps as follows

$$r_t = r_{t,sample} + 2 \cdot r_{contact,Al-sample} = \frac{\Delta x}{\kappa} + 2 \cdot r_{contact,Al-sample}. \tag{3.4}$$

Thus, to determine the actual thermal conductivity of the sample, the contact resistance had to be accounted for. Therefore, each material was tested for various thicknesses, Δx, establishing a linear relation between the sample thickness and the total thermal resistance r_t as seen in Figure 3.3. With this linear relation, the inverse of the thermal conductivity κ^{-1}, could be determined by the slope.
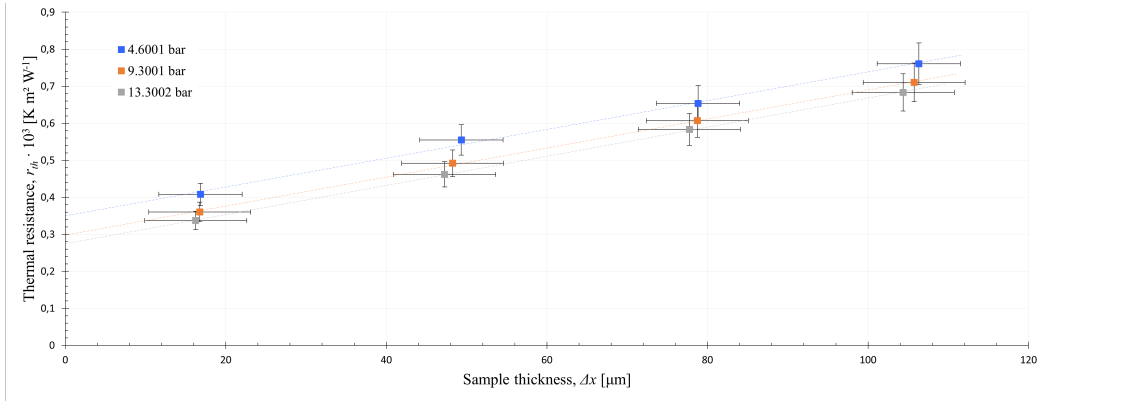
Figure 3.3: Image of the measured total thermal resistance of humidified Nafion 211 samples as a function of the sample thickness.

3.1.3   Experimental Procedure

The materials tested included a Nafion 211 membrane and a CCM composed of one Nafion 212 membrane with two CLs. The CCL and ACL were loaded with 0.3 and 0.1 mg Pt/cm^2, respectively. Each material underwent testing in both dry and fully humidified conditions.

To prepare the test samples, four 21 mm diameter disks were punched out of each material to match the cross-sectional area of the rod. Measurements at various thicknesses were then achieved by stacking one to four of the punched disks. During the measurements, the stacks were subject to three different clamping pressures: 4.6, 9.3, and 13.3 bars. For the humidified samples, the same procedure was followed, except they were submerged in demineralized water for a minimum of 30 minutes before testing. The rod was also sealed with parafilm to limit sample dehydration over the measurement period. The corresponding time intervals for each clamping pressure are detailed in Table 3.1. After determining the thermal conductivities experimentally, the results were further used to estimate the combined thermal conductivity of the CLs.

	4.6 bar	9.3 bar	13.3 bar	4.6 bar
Calibration	6 min	6 min	6 min	6 min
Dry Samples	20 min	15 min	15 min	6 min
Wet Samples	15 min	10 min	10 min	10 min

Table 3.1: Measurement time period for each clamping pressure.

3.2 In-Situ Temperature Measurements Using Optical Fiber Bragg Grating (FBG) Sensors

In addition to establishing thermal conductivities, the final part of the project thesis began the research for acquiring in-situ temperature measurements within the laboratory PEM fuel cell. However, this work was confined to ex-situ FBG calibrations and initial testing of fiber assembly. In continuation of the project work, the initial objective for this thesis was to achieve in-situ temperature measurements using FBG sensors.

Theoretical discussions on using optical FBG sensors for in-situ temperature measurements in electrochemical devices have attracted interest in numerous publications [8–10]. However, experimental validation of this theory remains scarce, with only a limited number of reports exploring its practical implementation. Nigel et al. are, to the author's knowledge, the only researchers who have tested the use of FBGs for temperature sensing within a PEM fuel cell [9]. Their approach successfully measured the temperatures across a custom-designed graphite flow field. To expand upon their research, this thesis will install an optical FBG sensor at the GDL of a laboratory PEM fuel cell. In contrast to the work done by Nigel et al., this approach requires no custom-made parts or alteration to the cell housing.

3.2.1 Experimental Setup

The experiments were conducted at a pre-existing fuel cell tester station at Varmeteknisk laboratory at NTNU, Trondheim. This test station consisted of three main components: the fuel cell housing, the fuel cell fixture, and the Fuel Cell Tester (FCT). Additionally, an optical fiber sensing setup was added to the station.

The Laboratory PEM Fuel Cell

The fuel cell test station used was equipped with a cell housing (cF25/100) to be installed in a Quick CONNECT fixture (qCf FC25/100), both from Baltic FuelCells. The open fuel cell housing is seen in the left image of Figure 3.4. This type of cell housing differs from the conventional bolted fuel cell housings as it is a clamped-based system to be compressed by a pneumatic cylinder. The cell housing consists of two end plates with embedded flow fields. The flow field area was 25 cm^2 and had a parallel serpentine flow field pattern at both the cathode and anode. These two end plates were to be clamped together with an MEA and gaskets in between
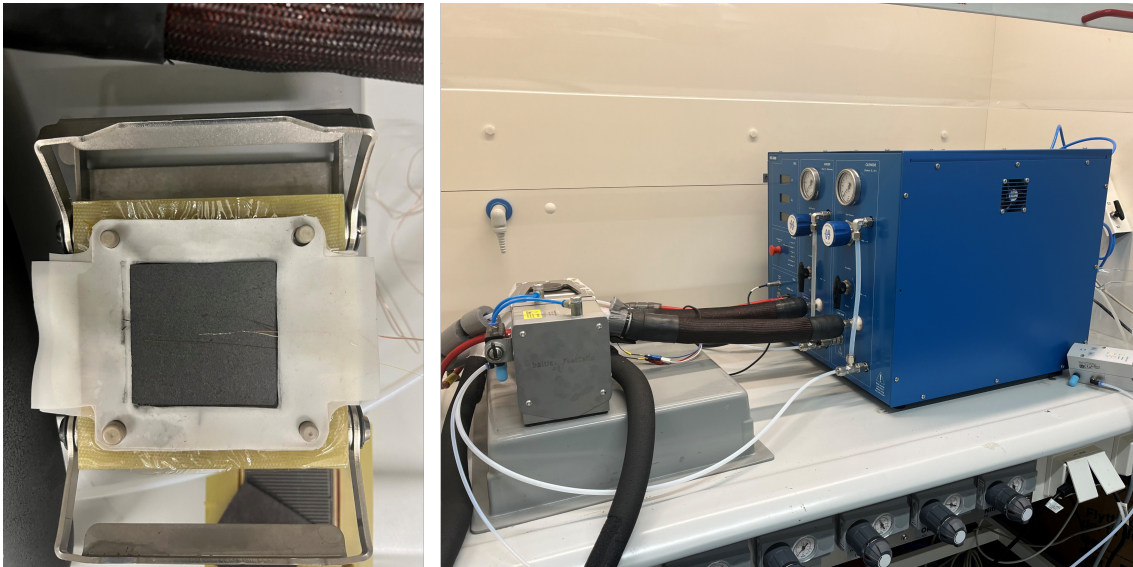
Figure 3.4: Imags of the opened fuel cell housing with installed FBG and thermo-
couple (to the left) and the FCT station (to the right).

them, to form a complete PEM fuel cell.

The particular MEA used for this thesis was a 11210 MEA from Baltic FuelCells
with an active area of 25 cm^2. This is the same type of MEA as used in the
thermal conductivity measurements in the project thesis, which consist of a Nafion
N212 membrane coated with platinum-loaded CLs. The CLs had 0.3 Pt/cm2 on
the cathode and 0.1 Pt/cm2 on the anode. Furthermore, it had two GDLs of the
type Sigracet S28BC, which is a PTFE-treated carbon paper with MPL. Finally, a
minimum of 2 gaskets were placed at each side of the MEA, to properly seal the
cell. These gaskets were manually cut from a silicon rubber sheet.

FBG Installation for PEM Fuel Cell Temperature Sensing

The optical FBG sensor was installed at the GDL of the PEM fuel cell. It was
chosen to do this by adding a second GDL, whereas the fiber would be placed in
between the two. The idea was that this would reduce some strain compared to
the fiber laying directly against the graphite flow fields. It was also assumed that
the temperature measurements would be less affected by the inlet temperatures of
the reactants and cooling water compared to placing the FBG directly against the
graphite plate. The second GDL used was a Toray PTFE-treated carbon paper
(TGP-H-030). Unlike the Sigracet S28BC GDL used in the MEA, the second GDL
did not consist of an MPL. It was attempted to place the FBG right in the center of
the active area of the cell. This is shown in Figure 3.4 where the FBG portion of the
optical fiber lays parallel to a k-type thermocouple to be used for the calibrations.

Finally, the cell assembly with the FBG also required an additional gasket on top of the fiber to be properly sealed.

The Fuel Cell Tester (FCT)

After assembly, the cell housing was placed inside the Quick CONNECT fixture, which is the gray structure seen in the right image of Figure 3.4. This is a structure designed to supply the cell with all the necessary gas and cooling media. Hence, all supply lines are connected to this fixture, making it possible to remove the cell housing without disconnecting any lines. Furthermore, the structure consisted of a pneumatic air cylinder used to fix the cell housing and apply a compaction pressure of 1.5 N/mm2 on the active area. The cooling media supplied to the fixture was water from a circulating bath set to the desired cell temperature. The water first flows through the integrated cooling channels on the cathode end plate, then through the anode end plate before returning to the bath.
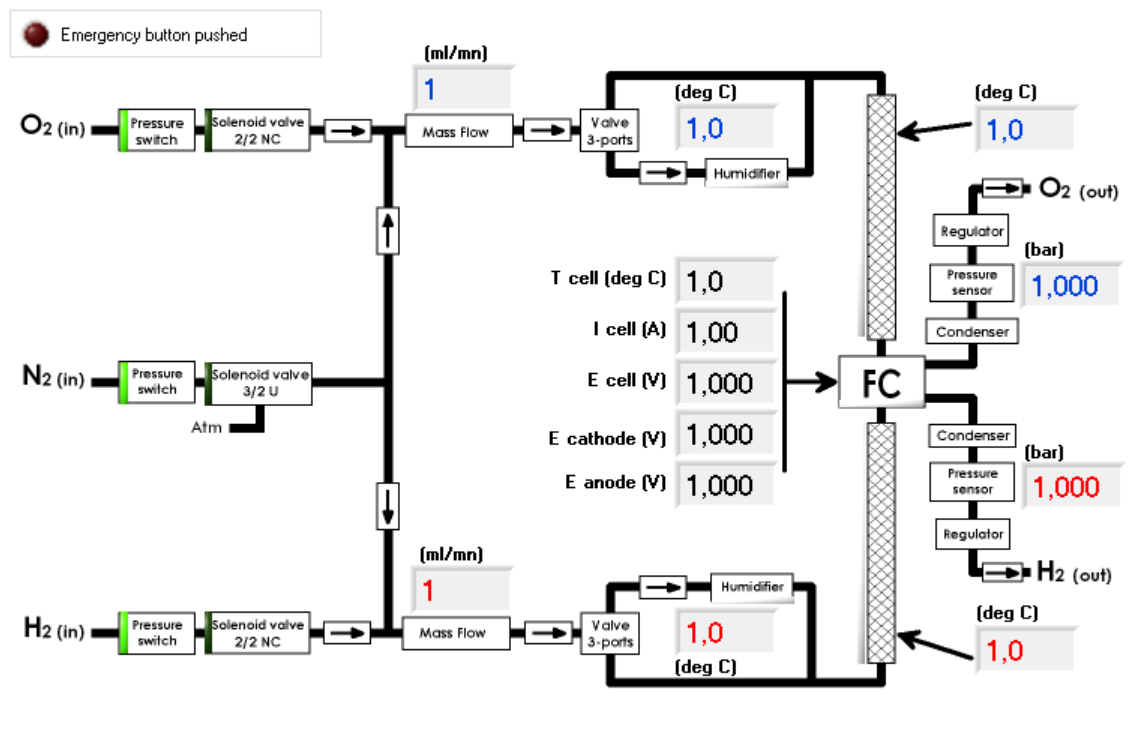
Figure 3.5: Schematics of the FCT station's internal gas line structure and integrated sensor locations as shown in the FCT-Lab software.

Furthermore, a Fuel Cell Tester (FCT-50/Z) and its associated monitoring software, FC-Lab, were used to operate the PEM fuel cell. This is a computer-controlled Fuel Cell Tester (FCT) from Bio-Logic Science Instruments and PaxiTech, which is seen to the right (blue box) in Figure 3.4. It is specifically designed for electrochemical testing of a single PEM fuel cell [40]. The FCT supplied the PEM fuel cell with

humidified gas, removed the products, measured the voltage, and applied electronic loads. An overall view of the internal gas line structures of the FCT and its sensor points can be seen in Figure 3.5. The FCT is equipped with a bubbler type of humidifier, filled with water heated to a set temperature. The humidifier temperature relies on the desired relative humidity of the fuel cell, whereas temperatures closer to cell temperature yield higher relative humidity. The gas exiting the humidifier then moves through a heated gas line before entering the cell housing. These gas line heaters are typically set 3-5 °C higher than the cell temperature to avoid any condensation.

Through the FC-Lab monitoring software, parameters such as the mass flow rates, temperatures, and load were user-regulated through an Ethernet connection. The supply gas pressures were also user-regulated with manual backpressure regulators [40]. In Figure 3.6 the "Gas" monitoring tab in the FC-Lab front panel is shown. The settings for the anodic and cathodic gas are set on the left side of Figure 3.6, while temperatures, pressures, flows, and the electric are monitored to the right. The gas supply, heating, load, and humidifier water are turned on in the top right corner. However, before turning on the load, the desired electrochemical techniques were programmed in the FCT software, and security limits had to be set. The user-defined FCT security limits and the corresponding actions set in this thesis are presented in Appendix A.
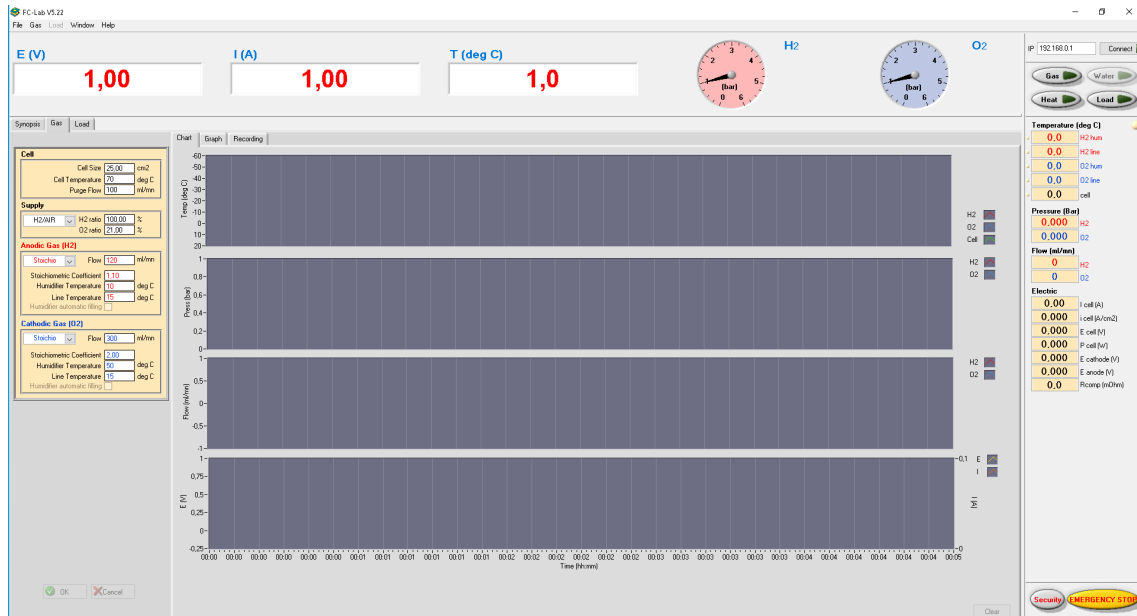
Figure 3.6: Image of the FCT-Lab front panel.

The Fiber Optic Setup

An optical fiber sensing setup was added to the FCT station to detect the reflected Bragg wavelength from the installed FBG. This setup consisted of three essential components in addition to the optical fiber, which were a light source, a fiber optic circulator, and a spectrum monitor. An image of the fiber optic setup is given in Figure 3.7, while a schematic of the same setup is given in Figure 3.8 for clarity.
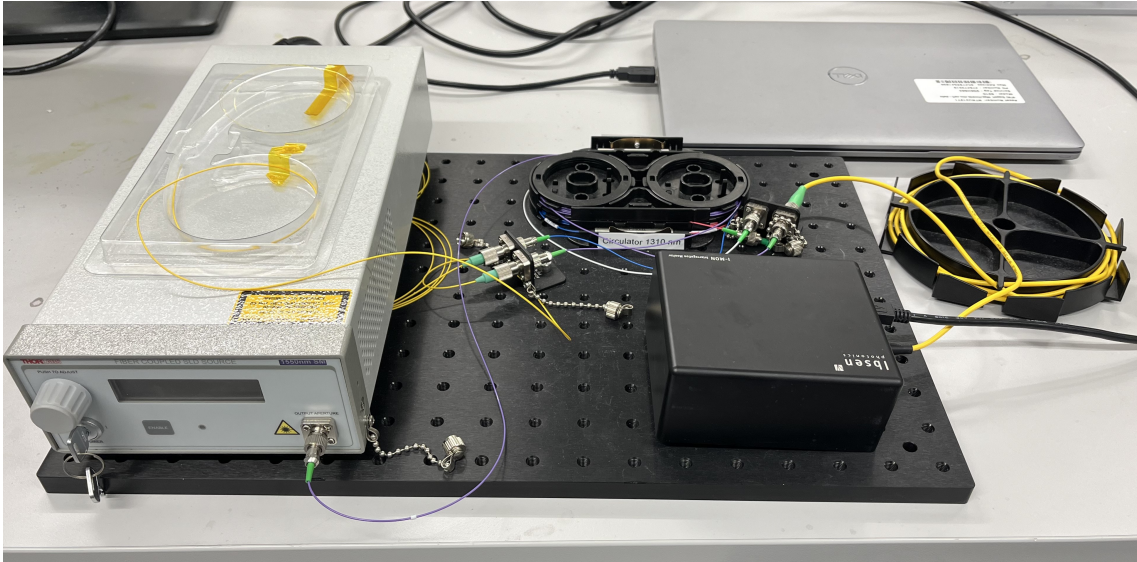
Figure 3.7: Image of the fiber optics setup.
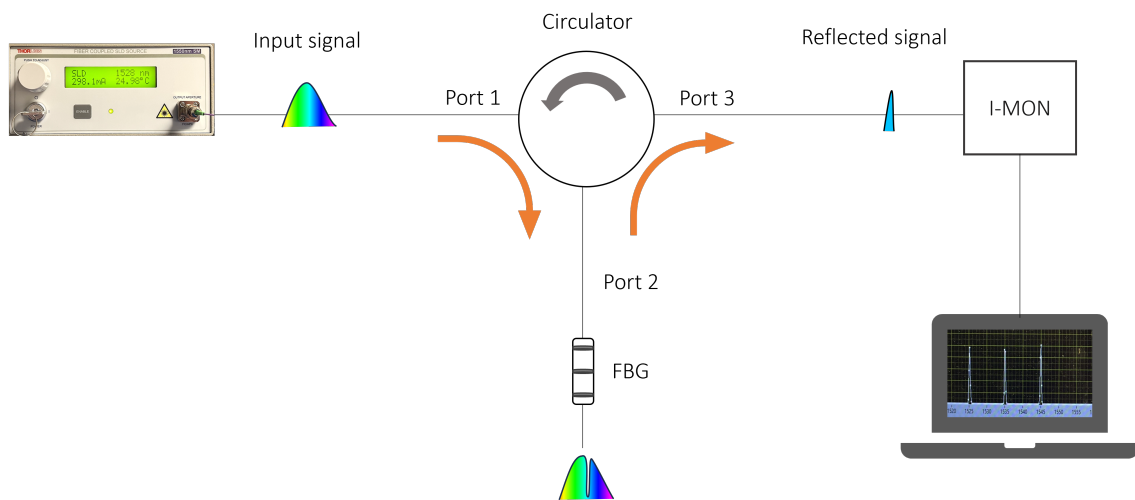
Figure 3.8: Schematic of the fiber optics setup.

A single-mode (SM) fiber-coupled superluminescent diode (SLD) sourced from THOR-LABS was utilized as the light source. This SLD featured a broadband emission centered at 1550 nm and an FC/APC bulkhead fiber connector. The provided input signal from the SLD was directed to a fiber optic circulator. An optic circulator

is a three-port device that only allows light to travel in one direction [41]. The circulator's role was to guide the input signal to the optical sensor and the reflected signal to the spectrum monitor. The spectrum monitor was an I-MON 256 USB Interrogation monitor (1525-1570 nm) from Ibsen Photonics [42]. This monitor was connected to a computer where the I-MON 256 USB Evaluation software provided real-time monitoring of the measured spectrum, as illustrated in Figure 3.9. Additionally, the software logged the peak reflected wavelengths in a user-defined text file.
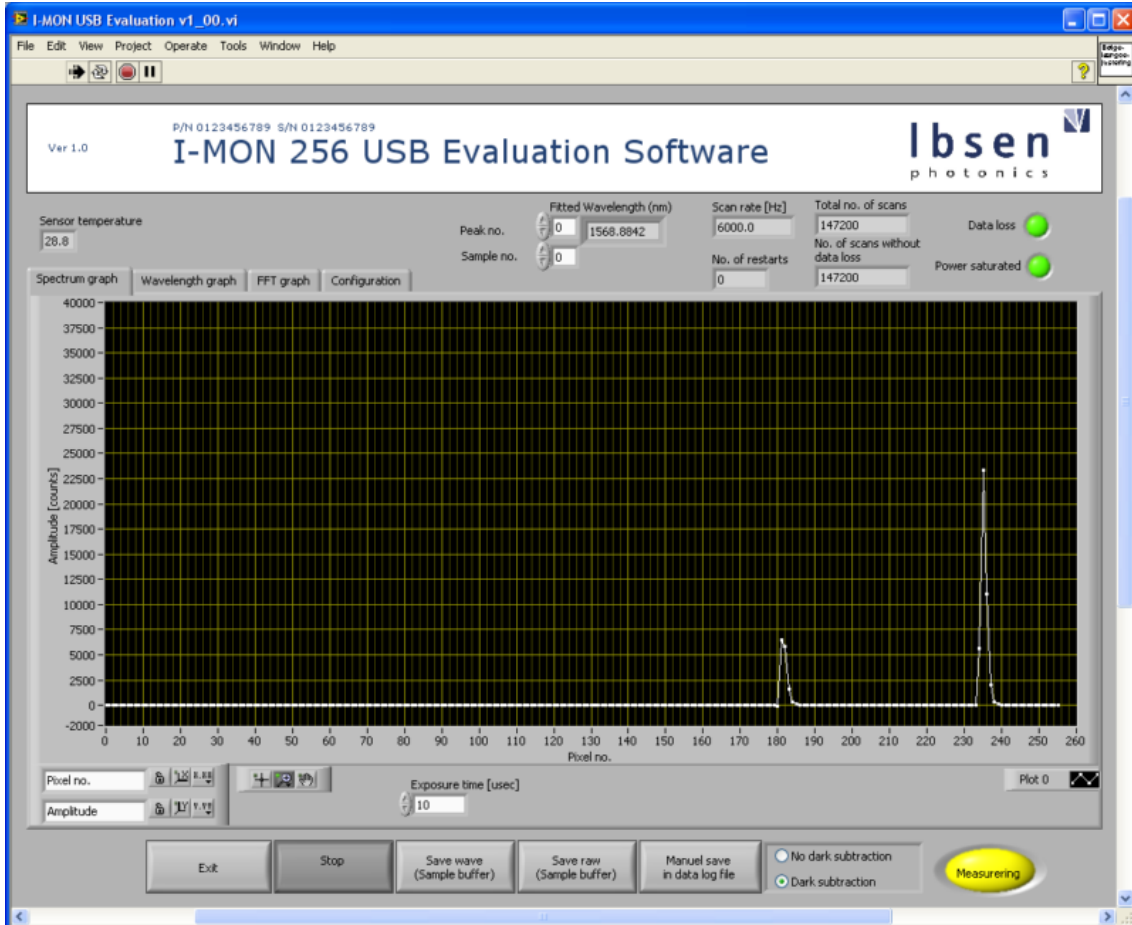
Figure 3.9: Image of the I-MON USB evaluation software front panel showing the optical response signal.

3.2.2 Ex-Situ and In-Situ Calibrations of the FBG: Mitigating Strain Effects on Temperature Measurements

As this master thesis is a continuation of the project thesis delivered in January 2024, some initial steps in achieving temperature sensing with FBGs were already completed. This included a calibration of three FBGs in an incubator, under the assumption of zero strain, to establish the linear relation between the temperature

and the reflected Bragg wavelength. Furthermore, one of the FBGs was centered between two GDLs at the cathode to do some initial temperature readings while running heated water through the cooling channels. However, this particular setup caused the optical fiber to be fixed at both sides of the FBG, which posed a significant strain effect on the reflected wavelength. As induced strain and increased temperatures, both increase the reflected Bragg wavelength, this translated to higher temperatures than the supply water. Hence, it was concluded that the method used was not able to accurately measure the PEM fuel cell temperatures.

For this thesis, several measures have been taken to avoid the same conclusion. Firstly, the non-coated optical fiber was exchanged with a polyimide-coated optical fiber that is less sensitive to strain. Secondly, the strain was limited by cutting off the end of the optical fiber so that the FBG would only be fixed on one side. However, this only limits the strain to some extent as the whole active area of the cell is subject to a 1.5 N/mm2 compression. Therefore, it was decided to perform additional in-situ calibrations with the FBG at the desired location for temperature measurements. This meant that the optical fiber would be subject to 1.5 N/mm2 compression during the calibration, limiting the uncertainty associated with the applied compaction pressure.

First, an ex-situ calibration was performed on the new polyimide-coated optical FBG sensor under the assumption of zero strain. This was done despite the project thesis concluding that neglectable strain was unattainable within the PEM fuel cell housing, as it provided information about the strain effect during later measurements. It was done following the same approach as done in the project thesis, by placing the FBG within a VWR INCU-Line 68R incubator [7]. The incubator was programmed to stepwise increase from 50 to 65 °C with a 5 °C interval. When the incubator reached one of the desired temperature steps, it was held for 30 minutes period, before moving on to the next temperature. Both the incubator temperature and the reflected Bragg wavelength were logged every minute of the calibration period.

Furthermore, the in-situ calibrations were performed by installing a k-type thermocouple next to the FBG in between the two GDLs at the cathode. This is seen in the left image of Figure 3.4. As the thermocouple reading is not reliable during operation due to the harsh cell environment, the in-situ calibration had to be done at non-operation. Hence, temperature variation was achieved by stepwise increasing the water temperature supplied to the cooling channels of the fuel cell. The water temperature supplied was varied between 50 and 85 °C with a 5°C step-size. These temperatures were chosen as the operating range for a PEM fuel cell lies between

60 and 80 °C [8]. The circulating bath temperature was increased as soon as both the thermocouple temperature and the reflected wavelength remained approximately constant for a ten-minute period. Afterward, the average temperature and wavelength were taken for the final 10 minutes of each temperature step and plotted to establish their linear relation through linear regression.

3.2.3 MEA Conditioning and Performance Assessment through Polarization Curves

It is well known that a newly assembled PEM fuel cell requires initial conditioning to achieve its optimal cell performance [43]. This is also referred to as the initial break-in of the cell. The general assumption is that the process increases the number of active catalyst sites in the CL and proton conductive channels in the membrane. However, the exact mechanisms taking place during initial conditioning are yet to be investigated [43]. The current methods utilized for the initial conditioning of the PEM fuel cell are established from experience, which all involve sufficient humidification of the membrane [44]. The most common conditioning methods consist of repeatedly going from a low to a high current density in a stepwise manner and/or operating at a high current density for a set period [44]. Overall, it is shown that high temperatures and humidity coupled with high currents and/or load cycling lead to a successful break-in [43].

The conditioning method chosen for this thesis is voltage stepping between high and low voltages, which is an equivalent approach to current stepping. This method is one of the more common techniques used and was recommended by the MEA supplier (Baltic FuelCells). To initiate the conditioning of the MEA, pure nitrogen at 100% humidification was applied for 10 minutes. This was also suggested by Baltic FuelCells to flush out residue from production. Then voltage cycling was done between 0.8 and 0.4 V for a 10-minute interval at each voltage level. The full duration of the conditioning varies depending on the MEA and the conditioning method. However, based on recommendations, a three-hour duration was chosen. Subsequently, the cell's conditioning status was assessed by monitoring whether the current remained constant for a set voltage across multiple cycles. One considers an MEA fully conditioned when the performance stops increasing with further voltage cycling. The conditioning was done at 80°C as higher temperatures are said to accelerate the process [45]. Both the hydrogen and oxygen gas were supplied at fully humidified conditions (100% RH) and their pressure was set to 0.5 bars. An overview of the FCT settings used during the conditioning of the PEM fuel cell is

seen in Table 3.2

Table 3.2: FCT settings for conditioning the MEA.

	H_2	O_2	Cell	Circulating bath water
Relative Humidity (RH)	100%	100%	-	-
Minimum flow [ml/mn]	200	300	-	-
Stoichiometric Coefficient	2	3	-	-
Humidifier Temperature [°C]	80	80	-	-
Line Temperature[°C]	83	83	-	-
Pressure [bar]	0.5	0.5	-	-
Temperature [°C]	-	-	80	82

Furthermore, polarization and power curves of a fuel cell are commonly used for assessing its performance. They are an easy tool to compare individual cells at specified operating conditions. However, they are also useful to see the effect of conditioning [45]. Hence, a polarization curve where created before and after the initial conditioning of the MEA. The operating conditions employed to generate the polarization curve were consistent with those intended for later fuel cell operation, as detailed in Table 3.3.

Table 3.3: FCT settings for PEM fuel cell operation and establishing polarisation curves.

	H_2	O_2	Cell	Circulating bath water
Relative Humidity (RH)	70%	70%	-	-
Minimum flow [ml/mn]	200	300	-	-
Stoichiometric Coefficient	2	3	-	-
Humidifier Temperature [°C]	62	62	-	-
Line Temperature[°C]	75	75	-	-
Pressure [bar]	0.7	0.7	-	-
Temperature [°C]	-	-	70	72

The polarization procedure was performed using the current-stepping technique in the FCT software, following the EU's polarization testing procedure for PEM fuel cell MEAs in single-cell configurations [32]. This is a current controlled technique where the resulting potential is measured. The current-stepping procedure used is summarized in Table 3.4. Each current step was held for the recommended dwell time to ensure stabilization of the voltage. For a non-conditioned MEA, the PEM fuel cell struggled to reach the maximum currents in Table 3.4. For this scenario, the current-stepping technique was stopped when the voltage went below 0.4 V.

Afterward, the measured voltages of the final 30 seconds of each current step were averaged. Furthermore, the average voltages are plotted against the respective cur-

rent density to create the polarization curve. To ensure precision, it is standard procedure to also calculate the standard deviation and add error bars to the polarization curve [32]. The respective power was then calculated by multiplying each average voltage with the respective current and plotted against the current density to create the power curve.

Table 3.4: Polarization protocol [32]

Step number	Current [A]	Dwell time [s]	Data acquisition time [s]
1	0.0	60	30
2	0.5	60	30
3	1.0	60	30
4	1.5	60	30
5	2.0	60	30
6	2.5	60	30
7	5.0	120	30
8	7.5	120	30
9	10.0	120	30
10	15.0	120	30
11	20.0	120	30
12	25.0	120	30
13	30.0	120	30
14	35.0	120	30

3.2.4 Optimizing PEM Fuel Cell Performance: Ramp-up and Ramp-Down Procedure

Following the MEA conditioning process, the PEM fuel cell was prepared for standard operation. However, it was noted that a proper ramp-up procedure was still necessary to achieve the same performance level as immediately following the conditioning. This was even more important if the cell housing had been opened since the conditioning. The ramp-up of the cell was simply done by performing current-stepping using the same current steps as given in Table 3.4. This step ensured that the voltage stabilizes before initiating experiments on the PEM fuel cell. Thus, it was essential to ensure a sufficient time interval at each current level for the voltage to reach stability. Generally, the ramp-up time intervals were closely aligned with those used for the polarization protocol.

Furthermore, a proper ramp-down procedure was required for the MEA to keep its optimal performance for a later occasion. However, if the MEA weren't to be reused or if the cell housing were to be opened it was sufficient to properly purge the cell with nitrogen. The initial step of the ramp-down procedure was to supply

the cathode with nitrogen while drawing current from the cell. The purpose of this initial step was to remove the leftover oxygen in the cell. Initially, the current was set to 1 A and decreased by 0.1 A each time the voltage fell below 0.4 V. When reaching a voltage below 0.4 V for a 0.2 A current, the load was turned off and nitrogen was supplied to the anode as well. At this point, there was only nitrogen flowing in the gas lines, purging the cell. While nitrogen was supplied the pressures were slowly decreased before turning off all gas supply.

3.2.5 In-Situ Temperature Measurements of the PEM Fuel Cell for Different Current Densities

The initial temperature measurements using an optical FBG sensor were conducted at the cathode of the PEM fuel cell, precisely at the same location as for the in-situ calibration. The fiber optic setup utilized in this thesis work allowed for temperature sensing with only a single optical fiber at a time. Also, the small active area of the laboratory PEM fuel cell only allowed for one FBG in the downstream direction. This FBG was placed right in the center of the cell's active area. As detailed in section 3.2.2, the fiber had been cut at the end such that it would only be fixed at one side of the FBG. This was done as a measure to prevent a significant strain effect on the temperature readings.

Furthermore, it was decided to measure the cathode temperature over a series of current densities, to see its effect on the internal temperature of the PEM fuel cell. For this, the current-stepping technique in the FCT software was utilized. The current steps and their time intervals are summarized in Table 3.5. The remaining FCT settings chosen during the measurements are given in Table 3.3, which stayed consistent throughout the current-stepping. It is, however, worth noting that the PEM fuel cell was operated at a stoichiometric flow mode. This means the mass flow rates were a function of the current drawn. As a result, the actual flow rates may differ from the minimum flow rate at higher current densities.

During the current-stepping technique, the reflected Bragg wavelength was logged by the I-MON software with a ten-second interval. Afterward, these readings were translated into temperature measurements using the linear relation found from the in-situ calibrations of the FBG.

Table 3.5: Current Stepping Set During The Temperature Measurements.

Step	Current [A]	Current Density [A/cm^2]	Time Interval [s]
1	8	0.32	300
2	10	0.4	300
3	12.5	0.5	300
4	15	0.6	300
5	20	0.8	300
6	25	1.0	300
7	30	1.2	300
8	35	1.4	300

Afterward, the FBG was moved to perform temperature measurements for the anode at the same operating conditions. The same MEA was used, however, both the FBG and the second GDL were moved, meaning the cell housing had to be opened. Consequently, it was observed a significant drop in cell performance after reassembling the PEM fuel cell. Thus, additional conditioning was performed in an attempt to recreate a similar environment as for the cathode temperature sensing.

Furthermore, it was at the time assumed that the strain effect at the anode would be similar to the strain effect measured at the cathode. Hence, a second calibration was not performed. This was a significant underestimation of the FBG's sensitivity to strain and was later proven to be far from reality. It was tried to correct this mistake by performing a calibration at the anode at a later time. However, since the FBG had been moved, one was not able to recreate the same strain experienced by the FBG during the measurements. Ideally, a new calibration and temperature measurements would be performed without moving the FBG, but the PEM fuel cell had at this point been disassembled. To correct for this, a new MEA had to be assembled and conditioned, before performing the calibration and the new temperature measurements. This was not completed due to limited time. Instead, it was attempted to draw some conclusions from the FBG response at the anode by assuming constant strain and an isothermal temperature over the PEM fuel cell at open circuit voltage (OCV).

3.3 Modeling PEM Fuel Cell Temperature Distribution

For many years, assuming isothermal conditions within PEM fuel cells was standard practice. However, this assumption does not hold at higher current densities [46].

Recently, the standard has shifted towards modeling temperature distribution by considering the various heat sources and sinks within the PEM fuel cell. Despite this, empirical data to validate these models remains scarce. In this thesis, a one-dimensional steady-state model of the laboratory PEM fuel cell was developed based on the experimental results obtained. These results included temperatures measured at the cathode GDL and the through-plane thermal conductivities determined in the project thesis [7].

3.3.1 Model Geometry

The geometry used for the one-dimensional model is depicted in Figure 3.10, and includes the MEA, the second GDL, and the two BPs. As shown in the figure, the model specifically considered the temperature profile under the land rather than the channels. Furthermore, a 10 μm layer was added between the GDL and the BP to account for their thermal contact resistance (TCR). All the thicknesses, δ, used in the model are given in Table 3.7, and marked along the x-axis in Figure 3.10. The x-axis was defined as the through-plane direction was set to zero at the center of the membrane. For simplicity, all modeled heat transfer was assumed to be in the x-direction. Furthermore, the temperature between the two GDLs at the cathode was set equal to the FBG-measured temperature at the specific current density, while the remaining temperatures were calculated at the interfaces of the layers.
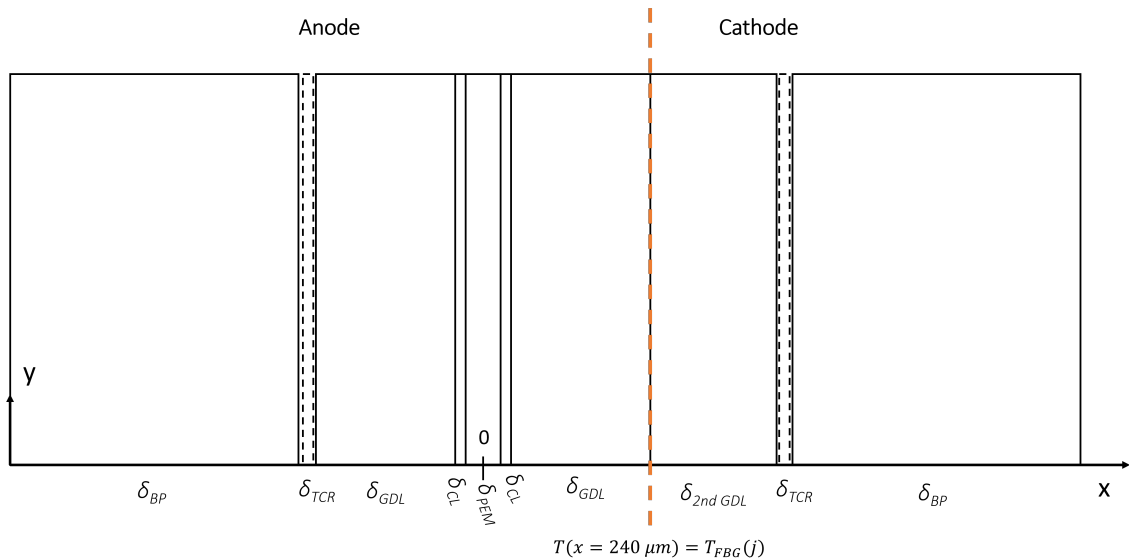
Figure 3.10: Visualization of the implemented model geometry.

3.3.2 Localization and Quantification of Heat Sources

Section 2.1.3 in the Theory touched on the increase in heat generation away from equilibrium due to irreversibilities. This was also illustrated by Figure 2.4, where the total heat generation was shown to be much larger than the reversible heat. Although the total heat released can easily be calculated from the cell potential, it is much more challenging to determine the local heat generation for each layered component. However, to model the temperature distribution of the PEM fuel cell, both the reversible and irreversible heat sources must be quantified and localized. Unfortunately, this is quite challenging and most model designs rely on a series of assumptions and simplifications. This section will cover the heat sources assumed in the model, as well as their assumed location, which is summarized in Table 3.6. In addition to the heat sources in Table 3.6, heat sources and sinks from mass transport were calculated and added by treating each layer as a separate control volume. This will be further detailed in section 3.3.3.

Table 3.6: Model implemented heat sources and their location.

Location	q'' $[W/m^2]$
ACL	$0.80 \cdot \frac{-T\Delta\bar{s}}{nF}j + \eta_{conc}^{anode}j + \frac{\delta_{CL}}{K_{CL}}j^2$
CCL	$0.20 \cdot \frac{-T\Delta\bar{s}}{nF}j + \eta_{act}j + \eta_{conc}^{cathode}j + \frac{\delta_{CL}}{K_{CL}}j^2$
Membrane	$\left(\frac{\delta_{mem}}{K_{mem}} + r_{contact}\right)j^2$
GDLs	$\frac{\delta_{GDL}}{K_{GDL}}j^2$
Toray GDL	$\frac{\delta_{Toray,GDL}}{K_{GDL}}j^2$
BPs	$\frac{\delta_{BP}}{K_{BP}}j^2$

Reversible Heat

The entropy change of the electrochemical reaction gives rise to the reversible heat. Since the two half-reactions take place at the ACL and the CCL of the fuel cell, the reversible heat is associated with the CLs of the PEM fuel cell. It is well known that the total entropy change in a PEM fuel cell is highly negative, which means the reversible heat source is large [46]. It is, however, far more challenging to determine the localized reversible heat at the ACL and the CCL. To add to the challenge, the reversible heat is proportional to the local temperature at the CLs which is

commonly unknown. For this model, 80% of the total reversible heat was assumed at the ACL and the remaining 20% at the CCL, which was based on a model presented by Burheim in 2017 [14]. The total reversible heat flux was expressed as

$$q''_{rev} = -\frac{T\Delta\overline{s}}{nF} \cdot j, \tag{3.5}$$

where T is the local temperature in unit K and $\Delta\overline{s}$ is the reaction entropy in units $J/molK$ [14]. In this model, the local temperature was assumed equal to the mean temperature over the CCM. The reaction entropy was calculated from the difference in entropy of the product and reactions as follows

$$\Delta\overline{s}(T) = \overline{s}(T)_{H_2O_{(l)}} - \frac{1}{2}\overline{s}(T)_{O_2} - \overline{s}(T)_{H_2}, \tag{3.6}$$

where tabulated entropy values were found as a function of the local temperature T at 1 bar [47].

Ohmic Heat

The ohmic heat in a PEM fuel cell is caused by the components' ionic and electric resistance. In many models, electronic resistances are assumed negligible in comparison to ionic resistance. It was, however, found that neglecting electric resistances underestimated the drop in potential at higher current densities and was therefore included in this model.

Firstly, the total ionic resistance was set as the sum of the resistance met by the protons in the membrane r_{mem}^{ionic} and the ionic contact resistance between the active site in the CLs and the membrane $r_{contact}^{ionic}$. Both of the respective heat sources related to the ionic resistances are assumed located at the membrane and proportional to the current density squared as follows

$$q''_{mem} = r_{tot}^{ionic}j^2 = (r_{contact}^{ionic} + r_{mem}^{ionic})j^2. \tag{3.7}$$

The ionic contact resistance between the membrane and CLs was assumed constant and equal to 0.8 $m\Omega \cdot cm^2$ based on the experimental findings of Pivovar and Kim for a commercial Nafion membrane [48]. The ionic membrane resistance, however, was calculated from the membrane thickness δ_{mem} and the ionic conductivity of the membrane K_{mem} as follows

$$r_{mem}^{ionic} = \frac{\delta_{mem}}{K_{mem}}, \tag{3.8}$$

where K_{mem} is given in units S/m. While the thickness was assumed constant, the ionic conductivity was calculated with respect to the humidity and membrane temperature. An increase in ionic conductivity can be achieved by sufficiently humidifying the membrane through proper conditioning and humidifying of the reactants. The humidification level of the membrane is defined by the number of water molecules per sulfonic group and is denoted by the Greek letter λ. A mathematical expression for the ionic conductivity K_{mem} of Nafion was presented by Springer et al. [49] as a function of the temperature T and humidity level λ as follows

$$K_{mem}(T, \lambda) = (0.5139 \cdot \lambda - 0.326) \cdot exp[1268(\frac{1}{303} - \frac{1}{T})]. \tag{3.9}$$

A fully humidified Nafion membrane can reach up to 22 water molecules per sulphonic group [11]. It is, however, more realistic to have between 14-21 water molecules per sulphonic group for a well-humidified PEM fuel cell [46].

Furthermore, the electrical resistances were calculated from the through-plane electrical conductivity and the thickness of each layered material in the PEM fuel cell. These conductivities were assumed constant and are listed in Table 3.7 along with the thicknesses used by the model. Consequently, an ohmic heat source from electric resistance was added to each of the PEM fuel cell layers.

Table 3.7: Constant model parameters.

Description	Symbol	Value	Unit	ref.
Nafion 212 Membrane thickness	δ_{mem}	50	μm	*
Catalyst Layer thickness	δ_{CL}	15	μm	*
Sigracet S28BC thickness	δ_{GDL}	200	μm	*
Toray Paper thickness	$\delta_{Toray,GDL}$	186	μm	*
TCR_{GDL-BP} thickness	δ_{TCR}	10	μm	[14]
Bipolar Plate thickness	δ_{BP}	5	mm	*
Electrical conductivity GDL	K_{GDL}	267	S/m	[16]
Electrical conductivity CL	K_{CL}	160	S/m	[16]
Electrical conductivity BP	K_{BP}	2000	S/m	[16]

*Manually measured values

Irreversible Heat

The irreversible heat is related to the overpotentials of the PEM fuel cell and is located at the CLs along with the reversible heat generation. To quantify the irreversible heat one must first calculate the overpotentials. This was done by considering the polarization curve created for the laboratory PEM fuel cell after conditioning.

First, the activation overpotential was modeled by the Tafel equation expressed in equation (2.6). To estimate the Tafel coefficients, the cell potential was plotted for the logarithm of the current density as seen in Figure 3.11 [30]. Also seen in the figure, a linear line was drawn for the cell potential for the smaller current densities, which represents the activation polarization dominated region. The b coefficient was set equal to the slope of this line, while the exchange current was determined by the intersection between this line and the OCV. The a coefficient was then estimated from the two as given in Figure 3.11.
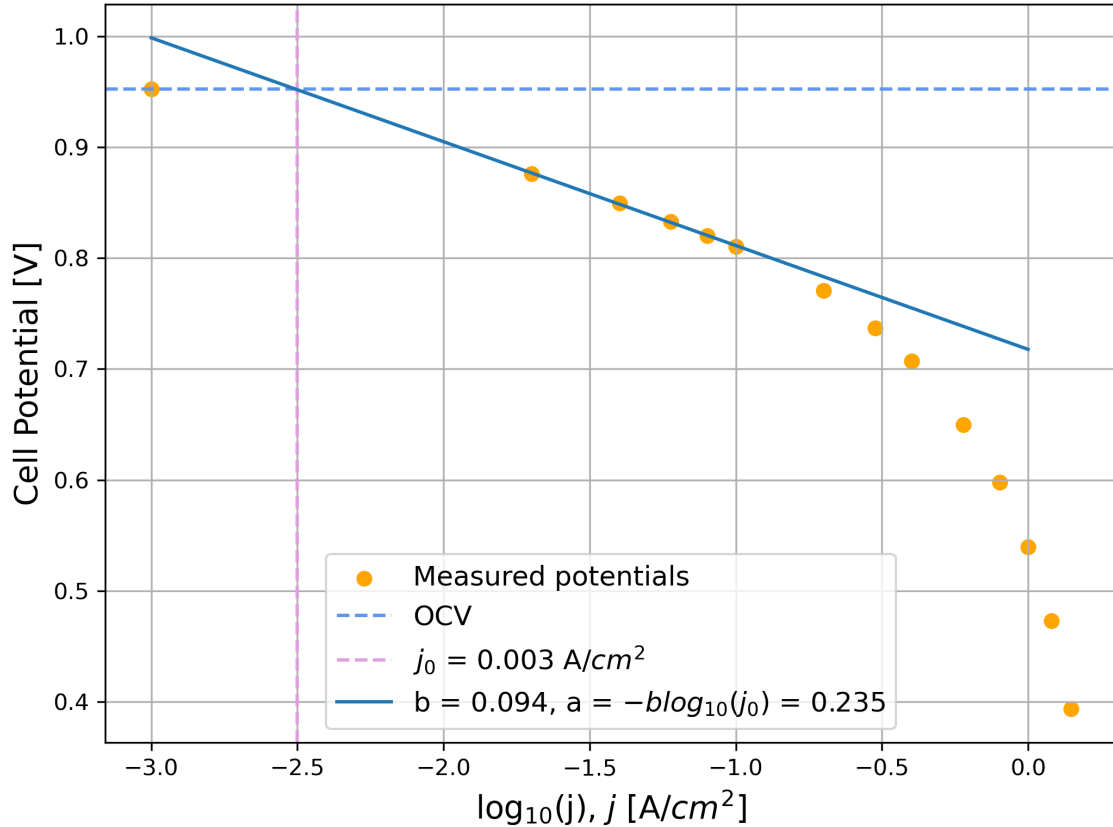
Figure 3.11: The Tafel equation found from experimental data.

The activation losses estimated by the Tafel equation are commonly associated with the CCL, while the activation losses at the anode are neglectable in comparison. Hence, the respective heat source was assumed located at the CCL in the model,

and calculated from the coefficients as follows

$$q''_{a,CCL} = (a + b log(j)) \cdot j. \tag{3.10}$$

Secondly, the concentration overpotential η_c was calculated using equation (2.7) for the ACL and equation (2.8) for the CCL as a function of the temperature and current density. The limiting current, however, was set equal to the maximum stable current density of 1.4 A/cm^2 obtained during the laboratory tests. The respective heat sources could then be calculated with respect to the current density as follows

$$q''(j,T)_{c,CCL/ACL} = \eta_{c,CCL/ACL}(j,T) \cdot j. \tag{3.11}$$

3.3.3 Mass Flows and Associated Heat Sources/Sinks
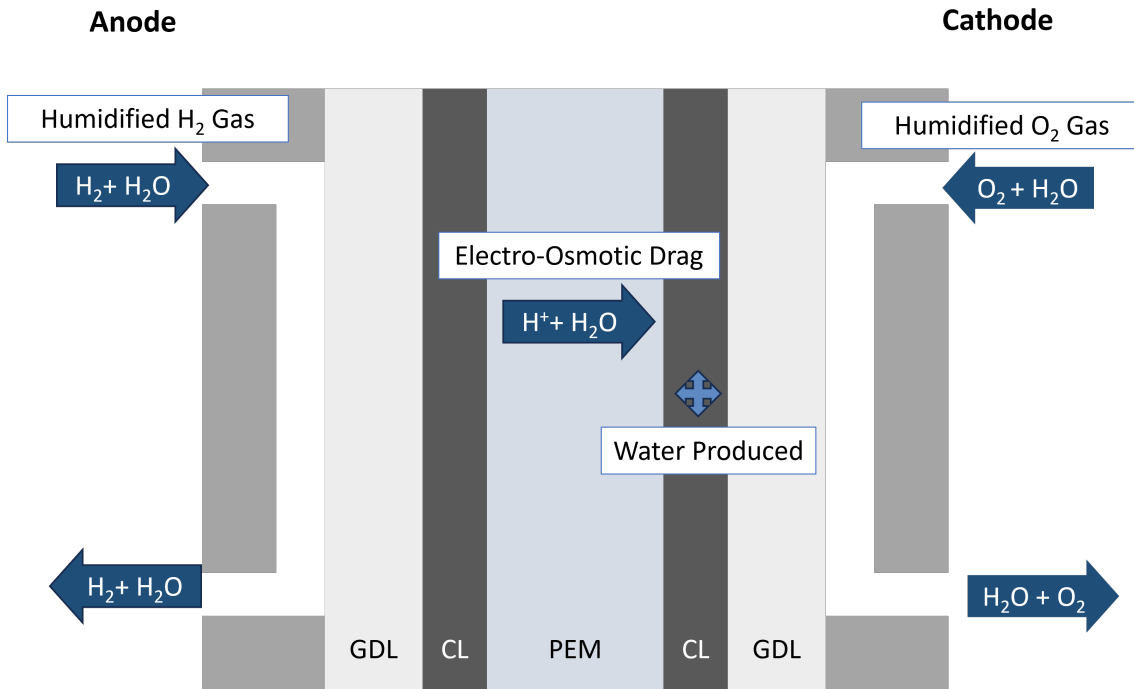
Figure 3.12: Illustration of the mass flows accounted for by the model.

In addition to the heat sources listed in Table 3.6, the heat transport by mass flow was also accounted for by the model. To do so, the mass flows within the PEM fuel cell had to be known. A summary of the mass flows considered by the model is given in Figure 3.12. These mass flows are dependent on the current density of the PEM fuel cell. First, the required supply of hydrogen and oxygen gas in g/sec for a specific current density is given as

$$\dot{m}_{H2,consumed} = \frac{jA}{2F} \cdot M_{H2}, \tag{3.12}$$

$$\dot{m}_{O2,consumed} = \frac{jA}{4F} \cdot M_{O2}, \tag{3.13}$$

where A is the active area of the fuel cell in cm^2, F is Faraday's constant and M is their molar mass in g/mol [50].

In reality, however, it is much more common to supply the fuel cell with more reactants than consumed. The ratio between reactant feed and reactant consumed is defined as the stoichiometric ratio λ which always is greater than one [50]. In most PEM fuel cell operations the stoichiometric ratio is set constant whereas the flow rates are adjusted accordingly as follows

$$\dot{m}_{H2,feed} = \frac{jA\lambda_{H2}}{2F} \cdot M_{H2}, \tag{3.14}$$

$$\dot{m}_{O2,feed} = \frac{jA\lambda_{O2}}{4F} \cdot M_{O2}. \tag{3.15}$$

The laboratory PEM fuel cell was operated at stoichiometric conditions where λ_{H2} and λ_{O2} were set equal to 2 and 3 respectively, with a minimum flow rate of 200 ml H2/min and 300 ml O2/min. Consequently, the minimum flows were used in the model for smaller current densities, while equations (3.14) and (3.15) were used for higher current densities. With stoichiometric settings, there were considerable amounts of recycled reactants, which were calculated as the difference between the mass rate of supplied reactants and consumed reactants.

The were also gaseous and liquid water flows present in the PEM fuel cell during operation. The water production was easily calculated from the respective current density as follows

$$\dot{m}_{H_2O,produced} = \frac{jA}{2F} \cdot M_{H_2O}, \tag{3.16}$$

where M_{H_2O} is the molar mass of water equal to 18 g/mol [50]. The model assumed all production water to be in liquid phase. The water following the feed gases, however, was assumed at gaseous phase. The FCT supplied the PEM fuel cell with gas at a constant humidity mass ratio of 4.06 gH_2O/gH_2 and 0.26 gH_2O/gO_2. Hence, the mass flow rates of water in the supply feeds was given as

$$\dot{m}^{anode}_{H_2O,feed} = 4.06 \cdot \dot{m}_{H2,feed}, \tag{3.17}$$

and

$$\dot{m}^{cathode}_{H_2O,feed} = 0.26 \cdot \dot{m}_{O2,feed}, \tag{3.18}$$

for the anode and cathode respectively. The model also accounted for water drag through the membrane along with the protons. This phenomenon is called electro-osmotic drag, where 2-5 water molecules are typically dragged per hydrogen proton [27]. However, it also depends on the membrane's humidity level λ. Springer et al. estimated that 2.5 water molecules were dragged for each proton for a fully humidified membrane ($\lambda = 22$). Consequently, the following equation was proposed for estimating the electro-osmotic drag for a specific membrane humidity level λ

$$\dot{m}_{H2O,drag} = 2.5 \cdot \frac{\lambda}{22} \cdot \frac{jA}{F} \cdot M_{H2O}. \tag{3.19}$$

After establishing all the mass flows, the heats transported by mass flow were incorporated into the model. The heat sources or sinks related to the mass flows was estimated following the approach described by Eichner, treating each material layer as a control volume [51]. Following this method, the heat sources or sinks from mass transport were defined by energy conservation and expressed as

$$\dot{Q} = \sum_{i,out} h_i \cdot \dot{m}_i - \sum_{i,in} h_i \cdot \dot{m}_i, \tag{3.20}$$

by assuming incompressible fluids. The enthalpies in equation (3.20) were calculated as

$$h_i = h_i^0 + c_{p/v} \cdot (T - T_0), \tag{3.21}$$

where T_0 is the reference temperature of 70°C and h_i^0 is the enthalpy of a specific fluid stream, i, at the reference temperature and 0.7 bar. Furthermore, c_p and c_v were used for gaseous and liquid fluid streams respectively. The specific heat capacities, as well as h_i^0, were determined by version 3.0.0b1 of the Catera library in Python.

3.3.4 Solving for the Temperature Profile

The model was based on energy conservation, assuming steady-state conduction in the x-direction to simulate the one-dimensional temperature distribution. Several of the modeled heat sources were temperature-dependent, so the temperature profile had to be solved iteratively. This is summarized in the flow diagram in Figure 3.14. The model estimated the temperatures at the interfaces of the different material layers, while the heat sources/sinks were established for each layer.

A thermal equivalent circuit analysis was done to estimate the fractions of the total heat generated leaving the anode and cathode respectively. This method of using heat flux fractions was inspired by the analysis by Burheim et al. on reversible electrode heats [52]. The anode and cathode equivalent thermal resistance was calculated by summing the thermal resistances on the left- and right-hand side of the membrane respectively as illustrated in Figure 3.13. The TCRs between the layers were neglected except for the TCR between the GDL and the graphite plate. In reality, the contact resistance would play some part in the temperature profile. They were, however, reduced to some extent due to the 15 bars compaction pressure applied during the temperature measurements. Furthermore, the anode and cathode equivalent resistance were used to calculate the fraction of the total heat flux leaving each side. The cathode heat flux fraction was estimated to be 40% from the following calculation

$$f_{cathode} = \frac{r_{anode}}{r_{anode} + r_{cathode}}, \tag{3.22}$$

while the total heat flux leaving the anode was set equal to the remaining 60%.
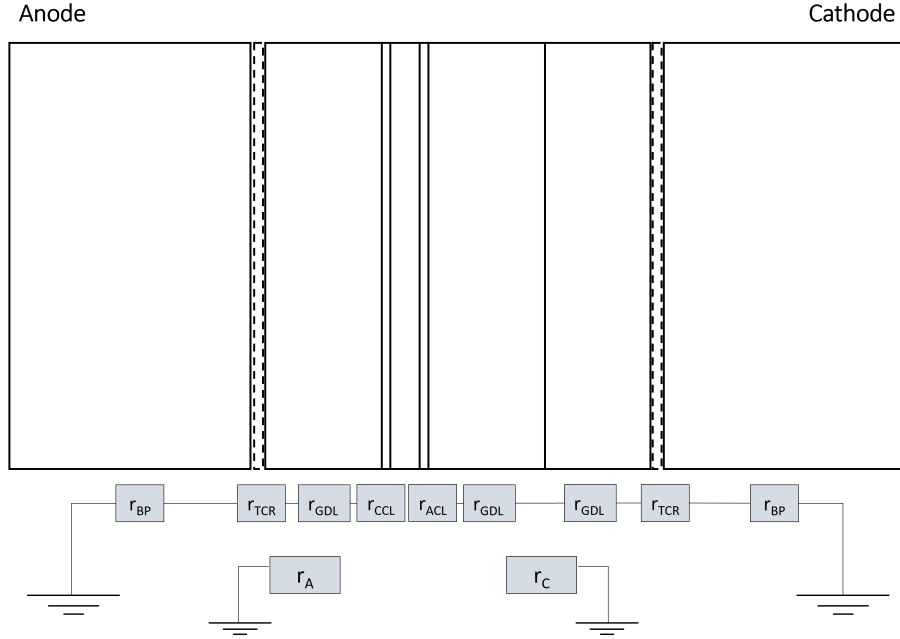
Figure 3.13: Schematic of the thermal equivalent circuit for the PEM fuel cell.

The initial temperature profile for each current density j was defined from the respective heat fluxes using Fourier law and $T_{FBG}(j)$ as the Dirichlet (constant temperature) boundary condition. Thus, Fourier's law, given in equation (2.11), was rewritten in terms of temperature as follows

$$T_i = T_{i+1} \pm q_i'' \cdot r_i, \tag{3.23}$$

where i is the layers from left (anode) to right (cathode). The sign is positive when the heat flux through the layer goes in the positive x-direction and negative if not. The initial temperature profile only accounted for the heat sources in Table 3.6. Furthermore, as the temperature over at the CLs was unknown at this point, $T_{FBG}(j)$ was used to estimate the reversible heat. This was later corrected to the mean temperature over the CCM after the initial run. Additionally, once the initial temperature profile was established, the heat transported by the mass flow at each layer could be estimated using equation (3.20) and (3.21). The heat fluxes and temperature profile were then corrected accordingly for N iterations. The iteration was stopped when all the temperatures in the temperature profile remained constant at the second decimal point. A total of 3 iterations were needed before the temperature profile converged for the higher current densities.

Figure 3.14: Flow chart for the temperature profile simulation.

3.3.5 Model Scenarios

The model parameters are selected to replicate the environment experienced during laboratory testing of the PEM fuel cell described in section 3.2.5. The laboratory FCT settings were summarized in Table 3.3 and serve as the basis for the model, along with the recorded current-voltage (I-V) relationship. Despite many of the required model parameters being experimentally determined from the laboratory PEM fuel cell testing, th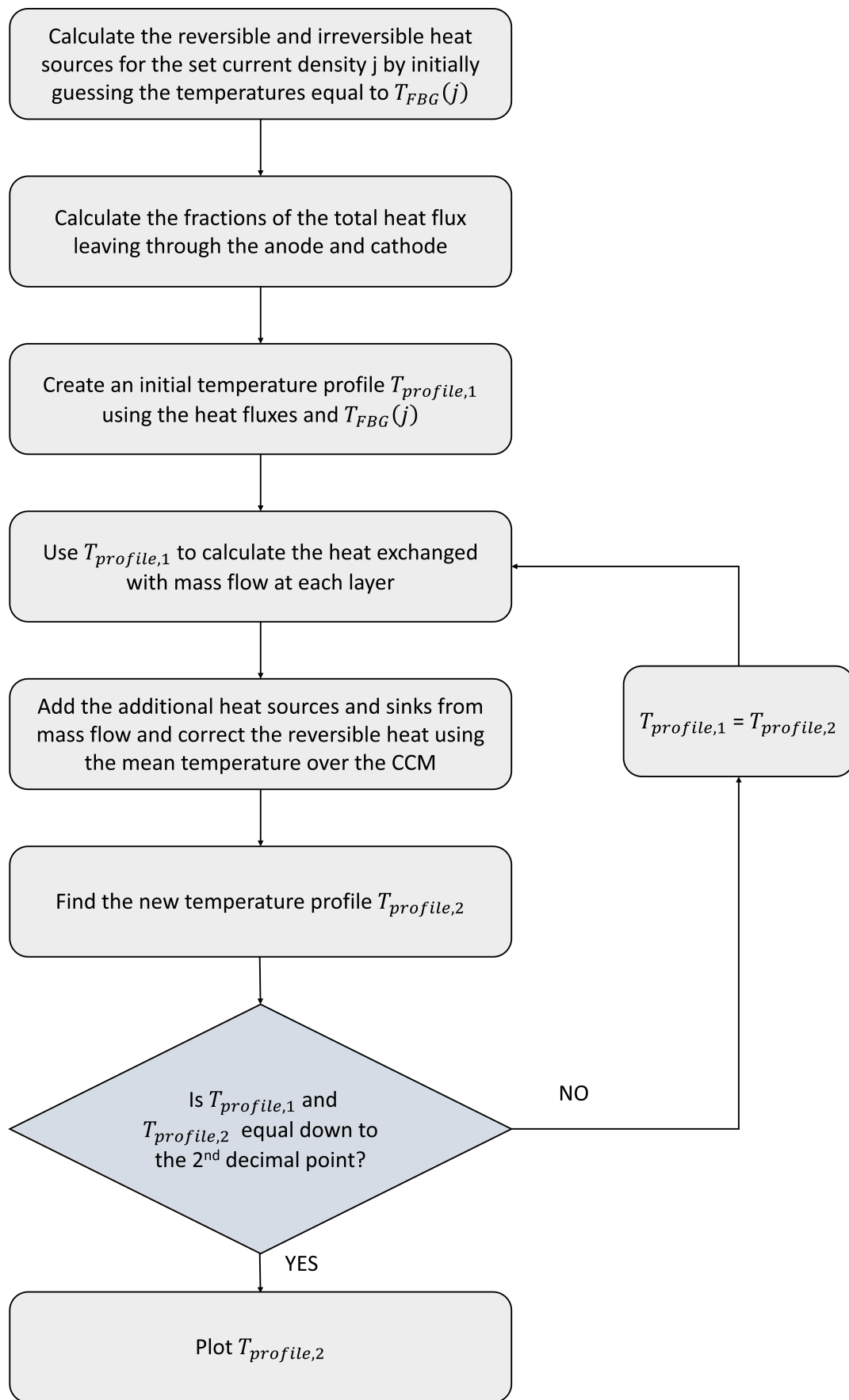e humidity level during fuel cell operation remains unknown. This parameter significantly affects the thermal conductivities, mass flows, and heat generation within the PEM fuel cell. Therefore, three model scenarios were created to represent a high, moderate, and poor humidification level.

A humidification level of 22 water molecules per sulfonic group was chosen for the first model case as this is considered the highest achievable value for a Nafion membrane [6]. This humidification level corresponds to the conditions under which the thermal conductivities were measured in the project thesis. Hence, these thermal conductivities are incorporated into this model case.

In reality, a well-humidified PEM fuel cell is more likely to have a humidity level between 14 and 21 water molecules per sulfonic group, and even fewer if not sufficiently humidified [46]. Thus, a humidification level of 15 and 10 water molecules per sulfonic group was chosen to model a moderate and poorly humidified membrane. The thermal conductivities were adjusted for each model scenario according to their humidity level. Each material was assumed to have a constant through-plane thermal conductivity, which was either based on the results from the project thesis or collected from the literature. The thermal conductivities used for each of the three model cases are listed in Table 3.8.

As seen in Table 3.8, the thermal conductivities of the GDLs were set constant for the three model scenarios. The TCR at the cathode, however, was adjusted accordingly. In the fully humidified scenario, the cathode TCR was set equal to the conductivity of water. This was adjusted to the thermal conductivity of air for the model scenarios of lower water content. The anode TCR, on the other hand, was kept constant to the thermal conductivity of hydrogen gas.

Table 3.8: The thermal conductivities used for the three model scenarios.

Material	κ $[W/mK]$	ref.
Fully humidified ($\lambda = 22$):		
Nafion 212 Membrane	0.254	[7]
Catalyst Layer	0.266	[7]
Sigracet S28BC	0.6	[53]
Toray Paper	0.449	[13]
Cathode TCR_{GDL-BP}	0.56	[14]
Anode TCR_{GDL-BP}	0.2	[54]
Bipolar Plate	8.35	[55]
Moderate humidification level ($\lambda = 15$):		
Nafion 212 Membrane	0.23	[14]
Catalyst Layer	0.20	[7]
Sigracet S28BC	0.6	[53]
Toray Paper	0.449	[13]
Cathode TCR_{GDL-BP}	0.03	[56]
Anode TCR_{GDL-BP}	0.2	[54]
Bipolar Plate	8.35	[55]
Poor humidification level ($\lambda = 10$):		
Nafion 212 Membrane	0.21	[11]
Catalyst Layer	0.11	[28]
Sigracet S28BC	0.6	[53]
Toray Paper	0.449	[13]
Cathode TCR_{GDL-BP}	0.03	[56]
Anode TCR_{GDL-BP}	0.2	[54]
Bipolar Plate	8.35	[55]

Chapter 4

Results

This chapter presents the results of the investigation into the temperature behavior of the PEM fuel cell in relation to current density. Firstly, the chapter will summarize the thermal conductivity results from the project thesis, which were integrated into the modeling scenarios of this study. Furthermore, the chapter will present the results from the FBG calibrations and the corresponding FBG-measured temperatures during PEM fuel cell operation. Finally, the chapter will present the simulated temperature profiles for the three model scenarios.

4.1   Measured Thermal Conductivities

The project thesis presented experimentally measured thermal conductivities, which is given in Table 4.1. These measurements include values for the Nafion membrane and the CCM at a dry and fully humidified state across various compaction pressures for an ambient temperature. Both components showed a significant enhancement of through-plane thermal conductivity with proper humidification. Additionally, Table 4.1 provides computed thermal conductivities for the CLs. It is essential to note that these values come with higher uncertainty due to error propagation, calculated using equation (2.22).

For this thesis work, only the thermal conductivities measured at a compression pressure of 13.3 bars are relevant, as this pressure best represents the 15 bars of compression pressure applied to the active area of the laboratory PEM fuel cell. At 13.3 bars, the Nafion membrane measured thermal conductivity of 0.149 ± 0.015 W/mK when dry. This value increased to 0.254 ± 0.005 for a fully humidified Nafion membrane estimated to have 22 water molecules per sulfonic group. Furthermore,

the CL was calculated to have a thermal conductivity of $0.203 \pm 0.128 \ W/mK$ at a dry state and $0.266 \pm 0.212 \ W/mK$ at a fully humidified state for 13.3 bars compression.

Table 4.1: Thermal Conductivity Results, $\kappa \pm 2 \cdot$ S $\quad [\frac{W}{mK}]$

Material	4.6 bar	9.3 bar	13.3 bar
Dry CCM	0.135 ± 0.013	0.154 ± 0.013	0.162 ± 0.009
Humidified CCM	0.231 ± 0.071	0.248 ± 0.073	0.258 ± 0.072
Dry Nafion®	0.135 ± 0.020	0.146 ± 0.018	0.149 ± 0.015
Humidified Nafion®	0.257 ± 0.022	0.255 ± 0.009	0.254 ± 0.005
Dry CL	0.134 ± 0.060	0.176 ± 0.090	0.203 ± 0.128
Humidified CL	0.192 ± 0.135	0.235 ± 0.181	0.266 ± 0.212

4.2 Experimental Results from PEM Fuel Cell Testing and In-Situ Temperature Measurements

To ensure accurate and realistic in-situ temperature measurements of the PEM fuel cell, several preparatory steps were taken. These included both ex-situ and in-situ calibration of the FBG sensor, MEA conditioning, and fuel cell performance evaluation. This section will begin by presenting the linear temperature relationships observed from the calibrations of the FBG. Thereafter, the performance evaluation before and after conditioning will be shown, before presenting the in-situ temperature measurements.

4.2.1 Results from FBG Calibrations

The project thesis presented the calibration of three FBGs under the assumption of zero strain [7]. These were calibrated for a temperature range from 25 to 70 °C in an incubator. From this calibration a sensitivity of 0.00973 to 0.00986 nm/ °C was recorded for all three of the FBGs, correlating to the theoretical sensitivity of
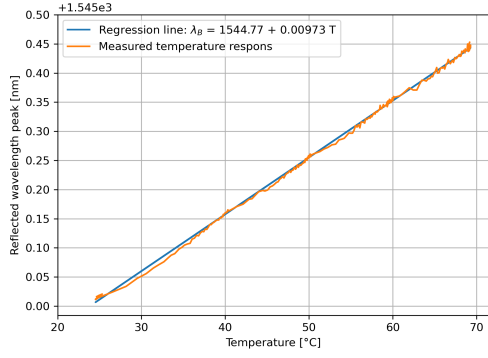
(a) Uncoated FBG number 1
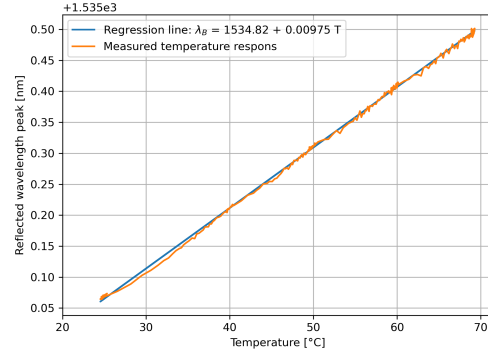
(b) Uncoated FBG number 2
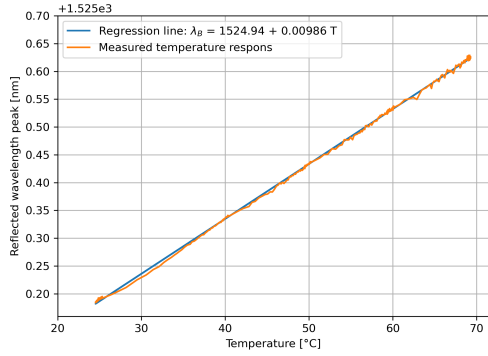
(c) Uncoated FBG number 3
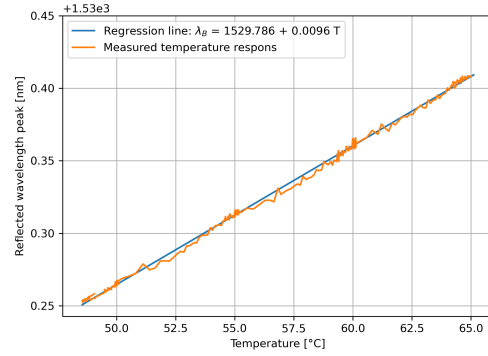
(d) New polyimide coated FBG

Figure 4.1: Plot of the reflected wavelengths from the three FBGs as a function of the external temperature during the calibration. A linear function is fitted to the measurement points and plotted with their coefficients given in the top left corner.

0.01 nm/ °C given for silica optical fibers [38]. In this thesis, the original uncoated optical fiber was replaced with a polyimide-coating optical fiber. This was calibrated following the same approach but for a smaller temperature range. The measured temperature response from the FBGs of the original uncoated optical fiber and the new polyimide coated optical fiber is given in Figure 4.1a - 4.1c and 4.1d respectively. The FBG in the new polyimide-coated optical fiber measured a similar temperature sensitivity of 0.0096 nm/ °C. Through linear curve-fitting, the calibration gave the following function for the reflected Bragg wavelength

$$\lambda_B(T) = 1529.786 + 0.0096T, \qquad (4.1)$$

where T is the temperature in °C.
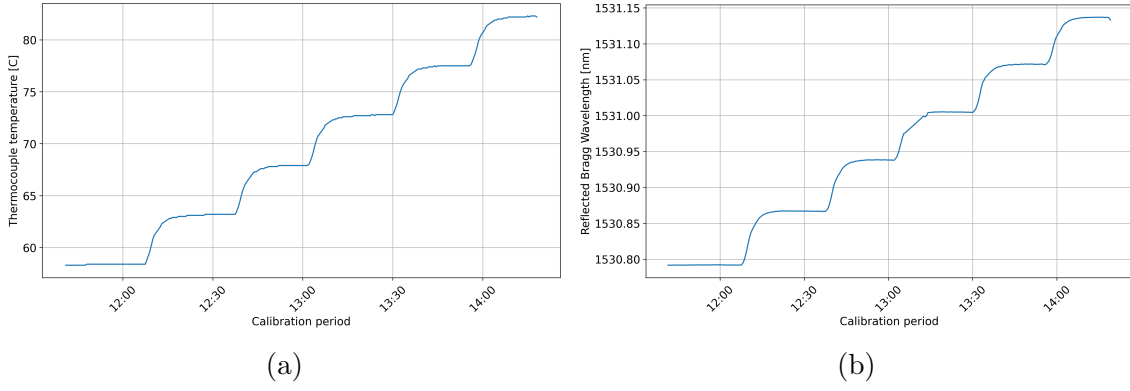
Figure 4.2: The measured thermocouple temperature (a) and the reflected Bragg wavelength (b) over the calibration period.

Furthermore, in-situ calibrations were performed to account for the significant strain effect on the FBG when placed inside of the cell housing. Two in-situ calibrations were performed on the FBG while assembled at the cathode of the PEM fuel cell. These were performed after the initial conditioning of the cell, right before the temperature sensing. The cell housing was kept untouched between the two calibrations.

Figure 4.2 shows the time response of the thermocouple and the reflected Bragg wavelength over the calibration period for the first of these calibrations. Both the temperature and the reflected Bragg wavelength were seen to reach a stable value for each interval. Hence, the temperature response was found by taking the average reflected Bragg wavelength over each stable temperature interval. These are marked by blue dots in Figure 4.3 for the first of the calibrations and pink for the second calibration. The maximum standard deviation for both calibrations was ± 0.00026 nm. From this, a linear relation was drawn, which also can be seen in Figure 4.3. Mathematically this relation was expressed as

$$\lambda_B(T) = 1529.97 + 0.01427 \cdot T, \tag{4.2}$$

where the temperature is given in °C. Comparing to the relation found for the ex-situ calibration in equation (4.1), a significant strain effect can be seen.
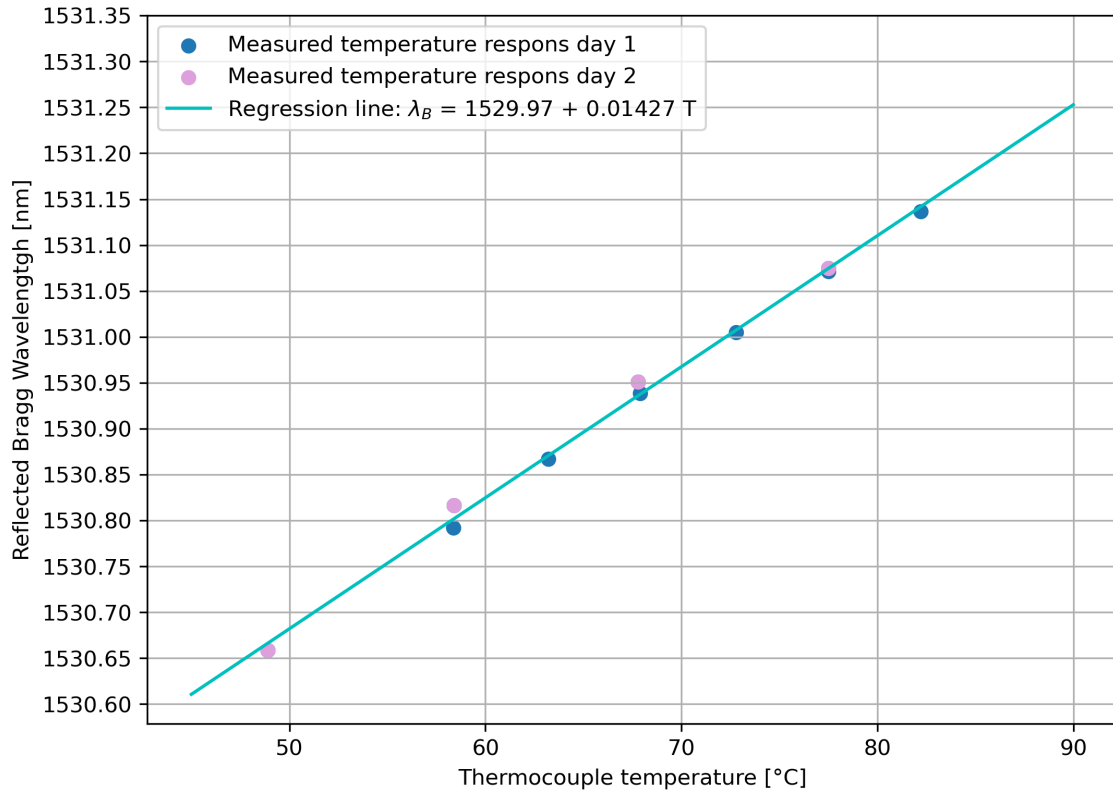
Figure 4.3: The measured temperature response from the two in-situ calibrations of the FBG located at the cathode GDL.

Upon realization of the FBG's sensitivity to location in the cell housing, an in-situ calibration was also performed for the FBG positioned at the anode GDL. The calibration plot and its linear regression line are presented in Figure 4.4. It's important to note that the exact position of the FBG, and consequently the imposed strain, were not consistent between the anode temperature measurements and the calibration process. The significant impact this has on the temperature readings will be discussed in Section 4.2.3.
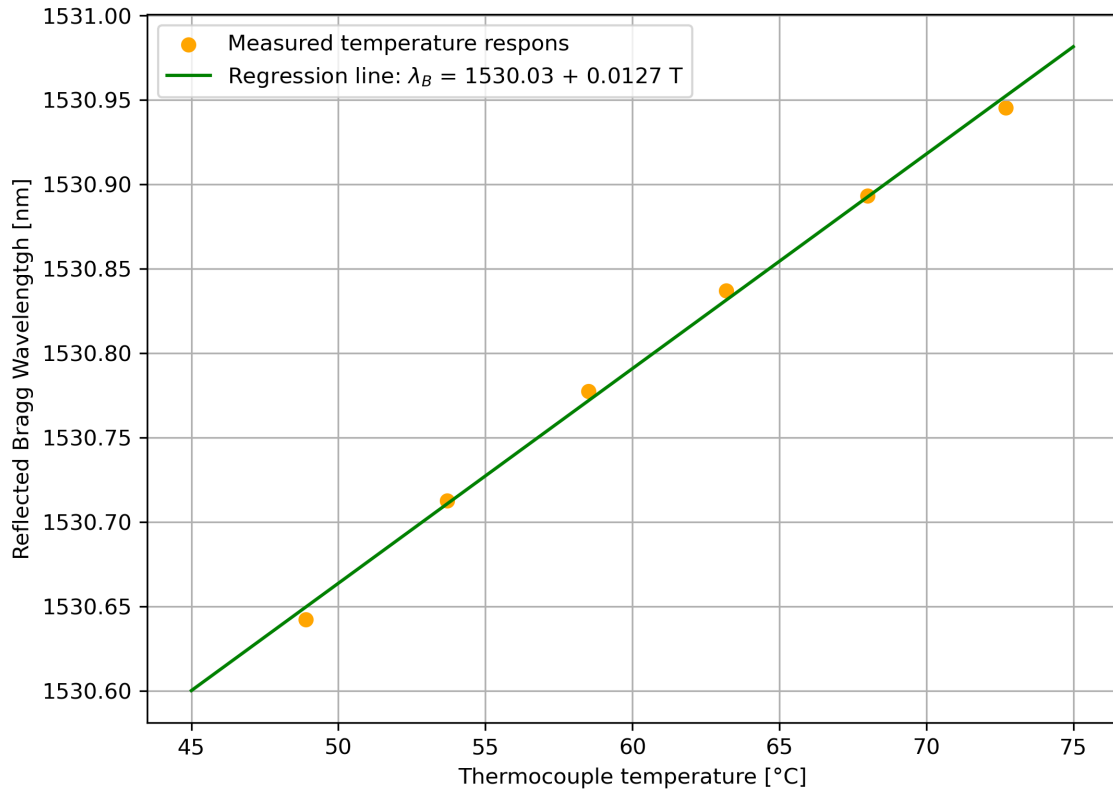
Figure 4.4: The measured temperature response from the in-situ calibration of the FBG located at the anode GDL.

4.2.2 Effect of PEM Fuel Cell Conditioning

Initial conditioning of the PEM fuel cell was done using voltage stepping. The voltage stepping and the respective current response over the conditioning period of 3 hours are shown in Figure 4.5. A PEM fuel cell is considered fully conditioned when the current stops decreasing for additional voltage steps. Yet, only a small change in the current for the high voltage step can be seen over the conditioning period from Figure 4.5. To see the full effect of conditioning a polarization and power curve were created from current-stepping done before and after the conditioning. The resulting polarization and power curves are given in Figure 4.6a and 4.6b respectively.

The maximum stable current the PEM fuel cell was able to obtain increased from 1 A/cm^2 to 1.4 A/cm^2 after the conditioning. Additionally, the conditioned PEM fuel cell exhibited higher cell potentials relative to the current density, as illustrated by the polarization curves in Figure 4.6a. Consequently, there was also a significant improvement in the power output of the conditioned PEM fuel cell. In Figure 4.6b, the unconditioned PEM fuel cell showed a maximum power of 9.7 W at 0.8 A/cm^2. However, the maximum power increased to approximately 14.2 W at 1.2 A/cm^2 after conditioning.

The polarization and power curves in Figure 4.5 also show a smaller, but not insignificant, improvement in the PEM fuel cell performance solely as a result of the first half of the current-stepping needed to acquire the I-V relation for the polarization curve. This was an early observation and was used to establish a ramp-up of the PEM fuel cell following the same approach to correct for any drop in performance over its non-operative period.
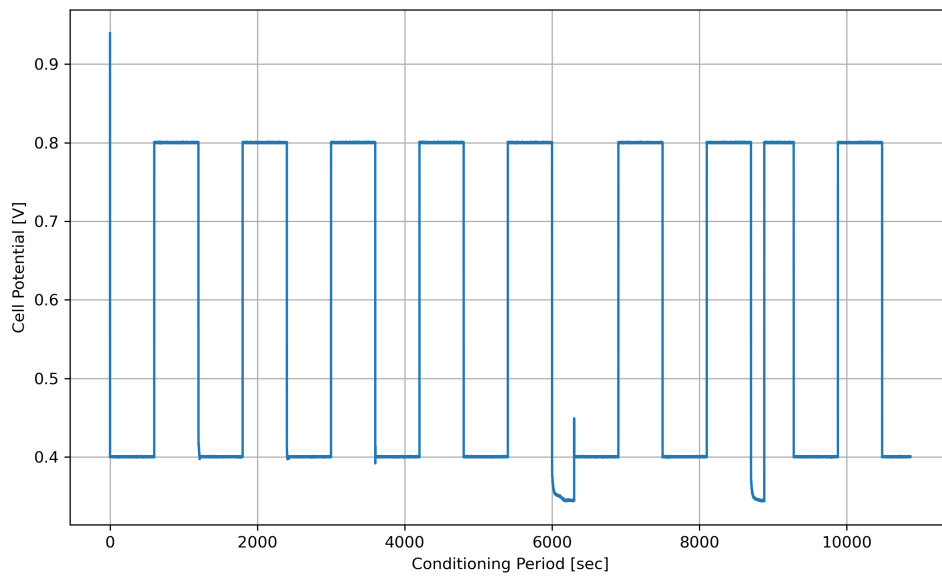
(a)
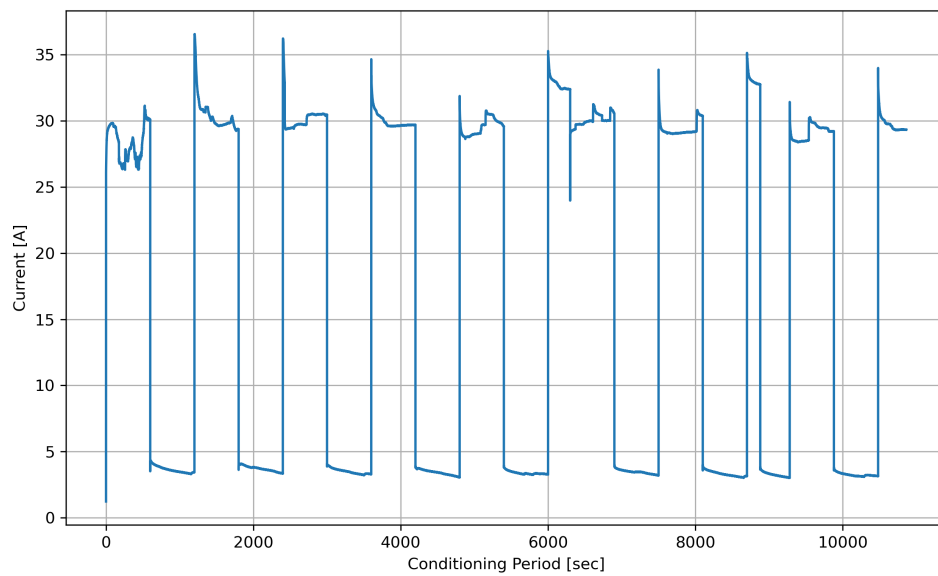
(b)

Figure 4.5: The voltage stepping (a) and the current response (b) during the 3 hours conditioning period.
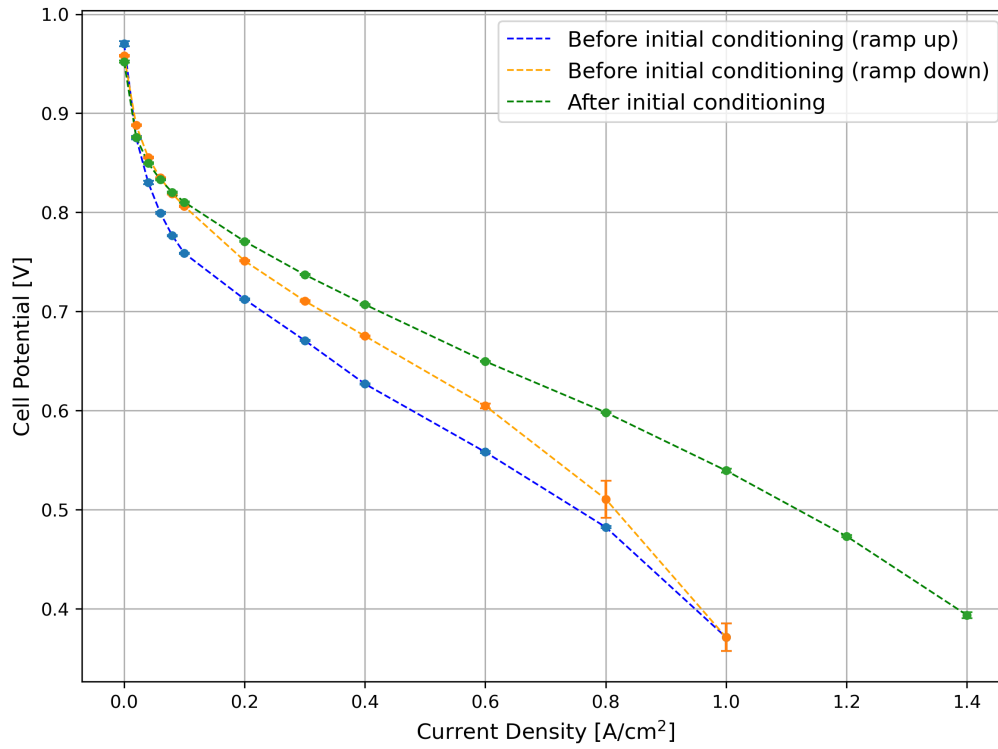
(a) Polarization curve
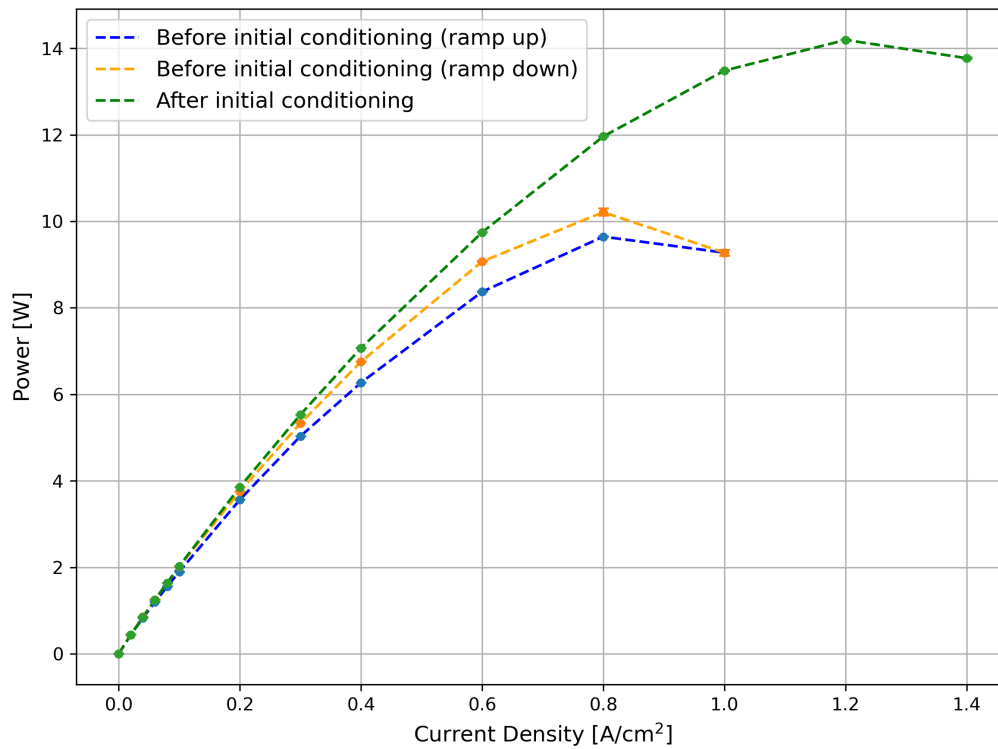
(b) Power curve

Figure 4.6: The polarization and power curve for the laboratory PEM fuel cell before and after conditioning.

4.2.3 FBG Measured Temperatures

The installed FBG measured temperatures at the center of the cathode GDL, while the PEM fuel cell underwent current-stepping. The FBG location was consistent with its position under the FBG calibration at the cathode. The cell was subject to a total of eight current steps between 8 and 35 A, each maintained for a five-minute interval. The current steps are plotted in blue in Figure 4.7. Meanwhile, the reflected Bragg wavelength from the positioned FBG was detected by the I-Mon software. Applying the linear relation estimated from the cathode calibration, as given by equation (4.2), the temperature response was plotted in red in Figure 4.7.

A temperature jump of 6 °C was measured at the cathode GDL when going from an OCV to operating at 8 A. At OCV the FBG measured a temperature of 70.6 °C, only slightly lower than the supplied cooling water temperature of 71 °C. From 8 to 35 A, the temperature at the cathode GDL increases with 13.13 °C.
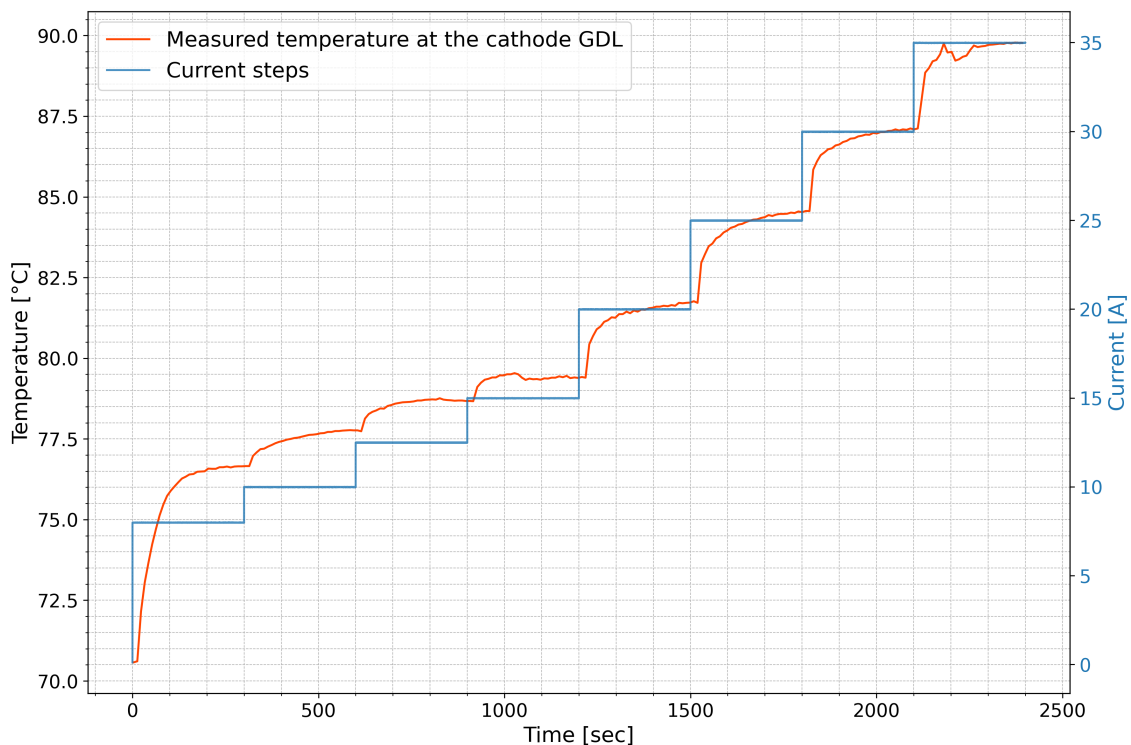
Figure 4.7: The temperature recorded by the FBG (in red) during the current-stepping (in blue) at the cathode GDL.

It is seen from Figure 4.7 that the temperature converges towards the end of each five-minute interval. To determine the steady-state temperature for each current step, the average temperature during the final minute of each current interval was calculated. These averages and their uncertainties are listed in Table 4.2 for each

current level. Table 4.2 also includes the temperature recorded by a K-type thermocouple at the cathode end plate, which is conventionally used by the FCT to determine the fuel cell temperature during operation. At OCV the thermocouple measured a temperature of 70.1 °C at the cathode end plate. Already, here it misrepresented the cell temperature measured to be 70.6 °C at OCV. As shown in Table 4.2, it is evident that the thermocouple's ability to indicate the cell temperature progressively worsens at higher currents.

Table 4.2: Steady-state temperatures at the cathode GDL, measured by the installed FBG for various currents.

I [A]	j [A/m^2]	T_{FBG}^{avg} [°C]	$\pm 2 \cdot S$	Thermocouple T [°C]
8	0.32	76.64	$\pm$ 0.026	70.3
10	0.40	77.76	$\pm$ 0.019	70.5
12.5	0.50	78.69	$\pm$ 0.014	70.6
15	0.60	79.41	$\pm$ 0.049	70.8
20	0.80	81.70	$\pm$ 0.073	71.0
25	1.00	84.51	$\pm$ 0.048	71.4
30	1.20	87.09	$\pm$ 0.041	71.8
35	1.40	89.77	$\pm$ 0.021	72.1

Furthermore, the FBG and second GDL were relocated to the anode to conduct temperature measurements at the same current levels. The objective was to use these measurements, in addition to those taken at the cathode, to model the temperature distribution across the PEM fuel cell. Achieving this requires similar fuel cell performance during both temperature measurements, as it directly affects the heat generation. The cell performance during the temperature measurements was evaluated by comparing their cell potential during the current-stepping.

The initial current-stepping performed after the reassembly of the cell is seen in green in Figure 4.8. When compared to the cell potential over the current-stepping for the FBG at the cathode, shown in blue, a significant performance drop is seen. This is most likely due to a dehydration of the MEA after opening the cell housing. Hence, a second conditioning was performed. The yellow plot in Figure 4.8 shows the cell potential over the current-stepping for the FBG located in the anode after the second conditioning. The second conditioning was shown to close the performance gap. Yet, the performance still varied greatly for many of the current levels. Furthermore, a reduction in the maximum stable current was observed after reassembly. Even after the second conditioning the maximum stable current was reached at 30 A in comparison with the originally maximum stable current of 35 A. Despite these variations, it was decided to proceed with the anode GDL sensor

measurements obtained after the second conditioning. This decision was made based on the acknowledgment that an exact reproduction of the initial cell performance was unattainable due to the changes in cell assembly.
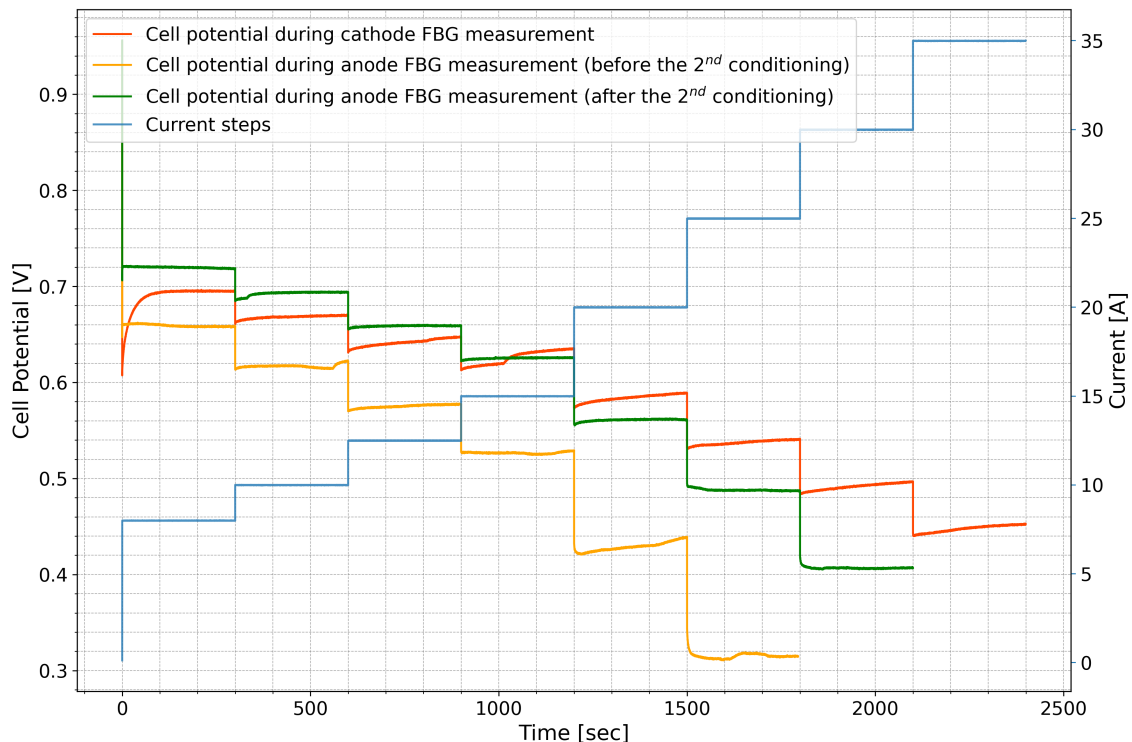
Figure 4.8: The recorded cell potential during the FBG temperature measurements. The image was used to compare the PEM fuel cell performance during the different measurements.

Figure 4.9a shows the reflected Bragg wavelengths from the FBG at the anode during the current-stepping done after the second conditioning. Using the linear relation obtained from the initial in-situ calibrations at the cathode, given in equation (4.2), a temperature profile was plotted in light blue in Figure 4.9b. This relation translated to significantly lower temperatures than expected from the FCT settings. The FCT settings are summarized in Table 3.3, and include a humidifier temperature of 62 ℃, a line temperature of 75 ℃, and a heating water temperature of 71 ℃.

Thus, the calibration with the FBG located at the anode was performed. The result from this calibration was given in Figure 4.4. Yet, this relation also displayed lower temperatures than expected from the FCT settings. The temperature measured by the thermocouple located at the cathode end plate of the cell housing is plotted in orange in Figure 4.9b for comparison. As both end plates are heated with heating water of 71 ℃, all measured temperatures are expected to be above 70 ℃ under operation. A hypothesis made was that the FBG experiences significantly lower strain than what was imposed during the calibrations. Hence, the temperature
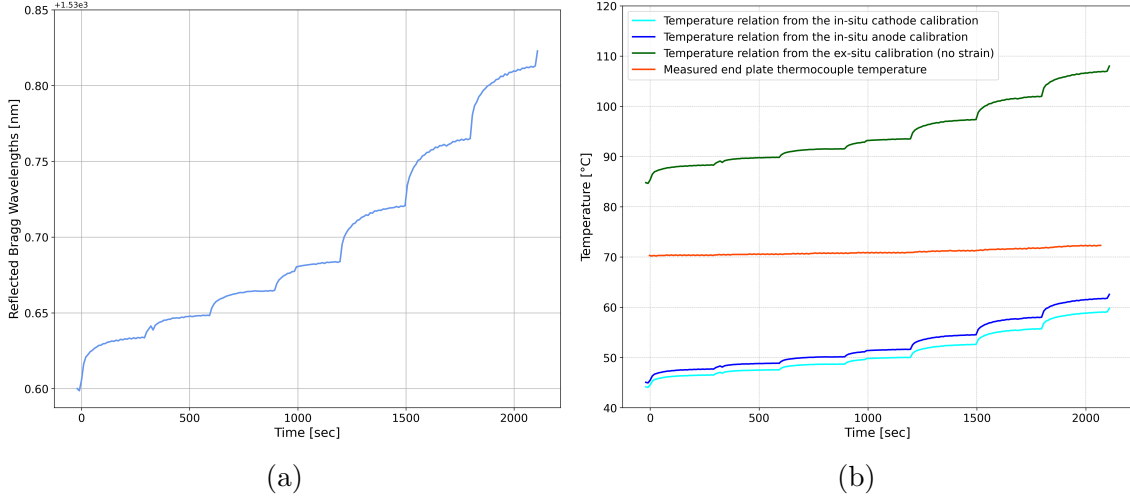
Figure 4.9: The reflected Bragg wavelength λ_B from the FBG installed at the anode GDL (a) and the resulting temperatures using the temperature relation found from the ex-situ and in-situ calibrations (b).

was also plotted under the assumption of no strain for comparison. The resulting temperature response for zero strain is plotted in green in Figure 4.4, which as expected provided significantly higher temperatures.

In light of the linear relations found in the calibrations leading to unreasonable temperature measurements at the anode GDL, a decision was made to pursue a mathematical estimation of the linear relation instead. To do this a series of assumptions were made. For all in-situ calibrations performed, the temperature sensitivity was between 0.0127 and 0.0144 nm/°C. This was true for all calibration done at both the cathode and anode. Hence, the temperature sensitivity was assumed to be within this range. Furthermore, the cell was assumed to be isothermal and equal to 71 °C at OCV, where the reflected Bragg wavelength was detected as 1530.60 nm. Using these assumptions, $\lambda_B(T)$ was estimated as

$$\lambda_B(T) = 1529.578 + 0.0144T, \tag{4.3}$$

for a 0.0144 nm/°C temperature sensitivity, and

$$\lambda_B(T) = 1529.698 + 0.0127T. \tag{4.4}$$

for a 0.0127 nm/°C temperature sensitivity. The resulting temperatures were plotted in Figure 4.10. If the assumptions are reasonable, one could further conclude that the true temperature at the anode GDL lies between the yellow and green lines in Figure 4.10 for each current. Table 4.3 gives the estimated steady-state temperature

for both the upper and lower calculated temperature response.
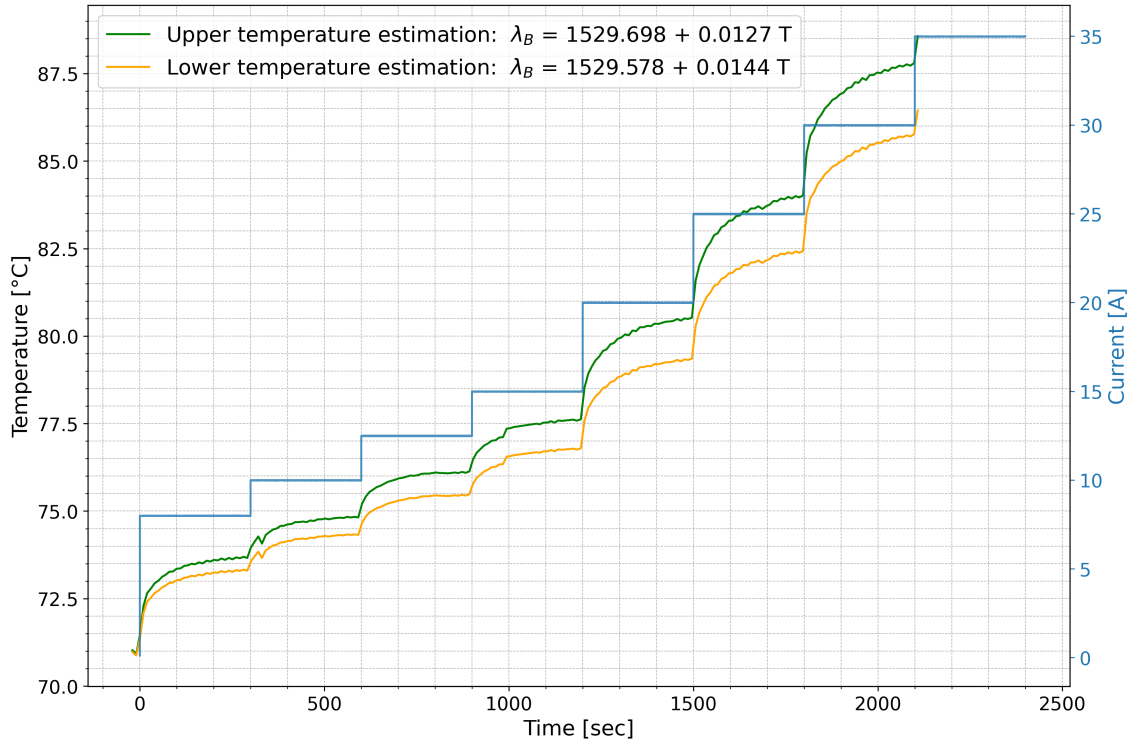
Figure 4.10: The upper and lower temperature estimation for the anode GDL for the current-stepping shown on the right axis in blue.

Table 4.3: Upper and lower limit estimations for the anode GDL temperature range for various currents.

I [A]	j [A/m^2]	Upper T_{FBG}^{avg} [°C]	$\pm \, 2 \cdot S$	Lower T_{FBG}^{avg} [°C]	$\pm \, 2 \cdot S$
8	0.32	73.64	$\pm$ 0.026	73.28	$\pm$ 0.023
10	0.40	74.81	$\pm$ 0.012	74.32	$\pm$ 0.010
12.5	0.50	76.09	$\pm$ 0.014	75.44	$\pm$ 0.012
15	0.60	77.59	$\pm$ 0.013	76.77	$\pm$ 0.011
20	0.80	80.46	$\pm$ 0.033	79.29	$\pm$ 0.029
25	1.00	83.95	$\pm$ 0.035	82.37	$\pm$ 0.031
30	1.20	87.70	$\pm$ 0.037	85.68	$\pm$ 0.033

Further, the upper and lower limits of the estimated temperature response at the anode GDL are compared to the measured temperature response at the cathode GDL in Figure 4.11. This shows a significant temperature difference between the anode and cathode GDL at lower current densities. The temperature gap, however, was closed for higher current densities.
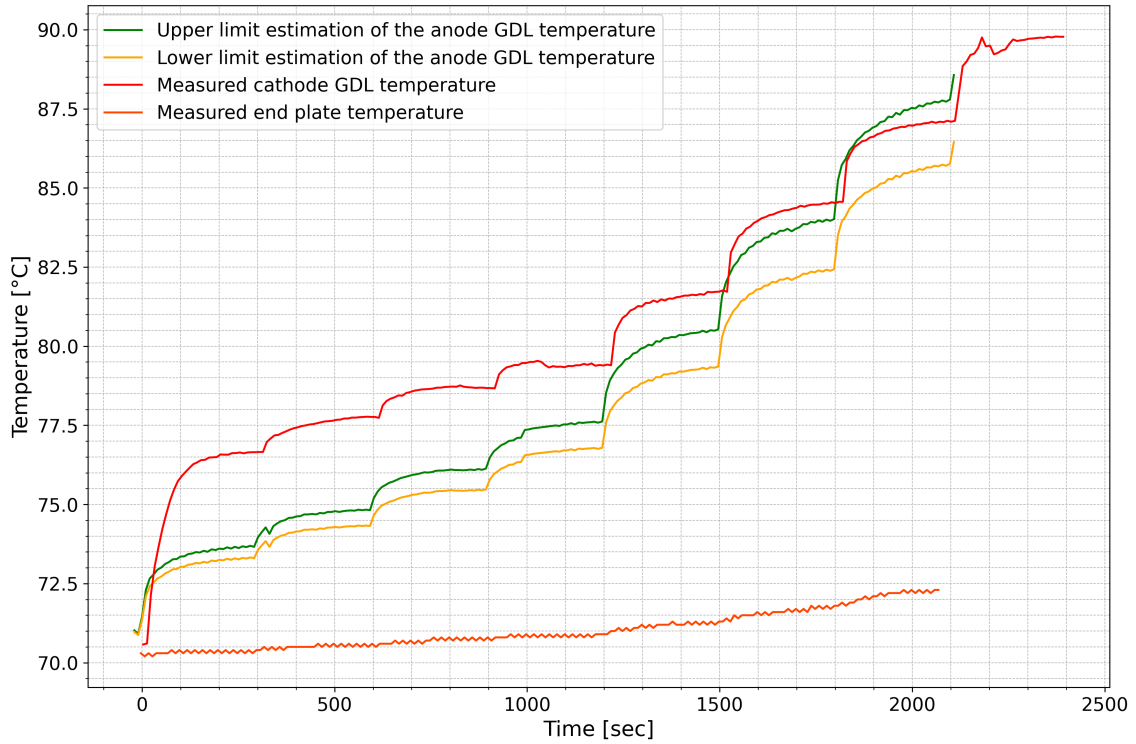
Figure 4.11: The measured cathode GDL temperature (red) over the current-stepping in comparison to the estimated anode GDL temperature (green and yellow) and end plate thermocouple measured temperature (orange) over the same current steps.

4.3   PEM Fuel Cell Modeling

To integrate the thermal conductivities from the project thesis with the in-situ temperature measurements obtained in this study, a one-dimensional thermal model of the laboratory PEM fuel cell was developed. The model was designed to simulate the through-plane temperature distribution experienced by the laboratory PEM fuel cell during testing. Consequently, the FCT settings outlined in Table 3.3, along with the measured I-V relation, were used to set the model parameters. Additionally, three different model scenarios were created for different humidification levels in the fuel cell. This section provides the model result for all three model scenarios.

4.3.1   The Modeled Losses

The activation, ohmic, and concentration losses were essential parameters to be estimated for the model. Firstly, the activation losses were assumed to be described by the Tafel equation. The I-V relation measured after the initial conditioning, seen

in Figure 4.6a, was used to estimate the Tafel coefficients and the exchange current of the PEM fuel cell. The approach is shown in Figure 3.11, yielding an exchange current of 0.003 A/cm^2 and the Tafel coefficients a and b equal to 0.235 and 0.094 respectively. Consequently, the following Tafel equation is used by the model

$$\eta_a = 0.235 + 0.094 \cdot log_{10}(j), \tag{4.5}$$

where j is given in A/cm^2.

Furthermore, concentration losses were modeled using equation (2.7) and (2.8), by assuming a temperature of 80 °C and a limiting current of 1.4 A/cm^2. The value 1.4 A/cm^2 was chosen because it represents the maximum stable operating current achieved by the PEM fuel cell. Lastly, the ohmic losses were modeled, where the ionic resistance were calculated from equation (3.8) and 3.9 for the respective humidity level. Figure 4.12 compares the modeled cell potential for all three model cases to the experimentally measured I-V relation. As seen in the figure, the model scenario that best represents the experimental data varies with current density. The best fit between the modeled potentials and the experimental data is seen for current densities between 0.3 and 0.8 A/cm^2 for all three model scenarios.
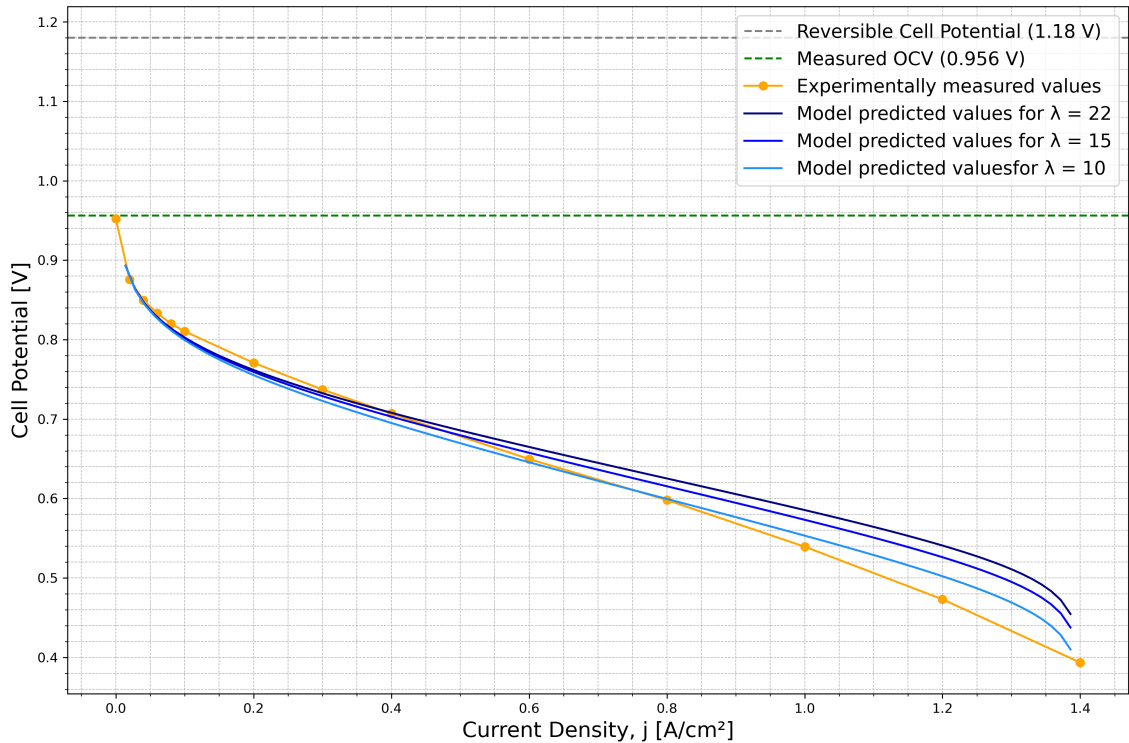
Figure 4.12: The model predicted polarization for the three model scenarios in comparison to the experimental data.

4.3.2 Simulated Temperature Profiles

The model was designed to establish the temperature profile over the laboratory PEM fuel cell based on the FBG-measured temperatures at the cathode GDL. The temperature profile was modeled for various humidification levels, as this was an unknown parameter during the fuel cell testing. The humidification levels modeled were the maximum humidity level ($\lambda = 22$), a moderate humidity level ($\lambda = 15$), and a poor humidity level ($\lambda = 10$). The three model cases and their respective thermal conductivities were listed in Table 3.8.

The simulated temperature profile for the fully humidified case, the moderately humidified case, and the poorly humidified case are given in Figure 4.13, 4.14 and 4.15 respectively. The vertical orange line in all three figures represents the FBG location, where the temperature was set constant and equal to the measured FBG temperature for each current density. Furthermore, the mass flows, activation losses, and concentration losses remained the same for all three model cases. The ohmic losses, however, were altered with respect to the humidity level λ. For all model cases, the maximum temperature was found at the CCL. These are listed in Table 4.4.
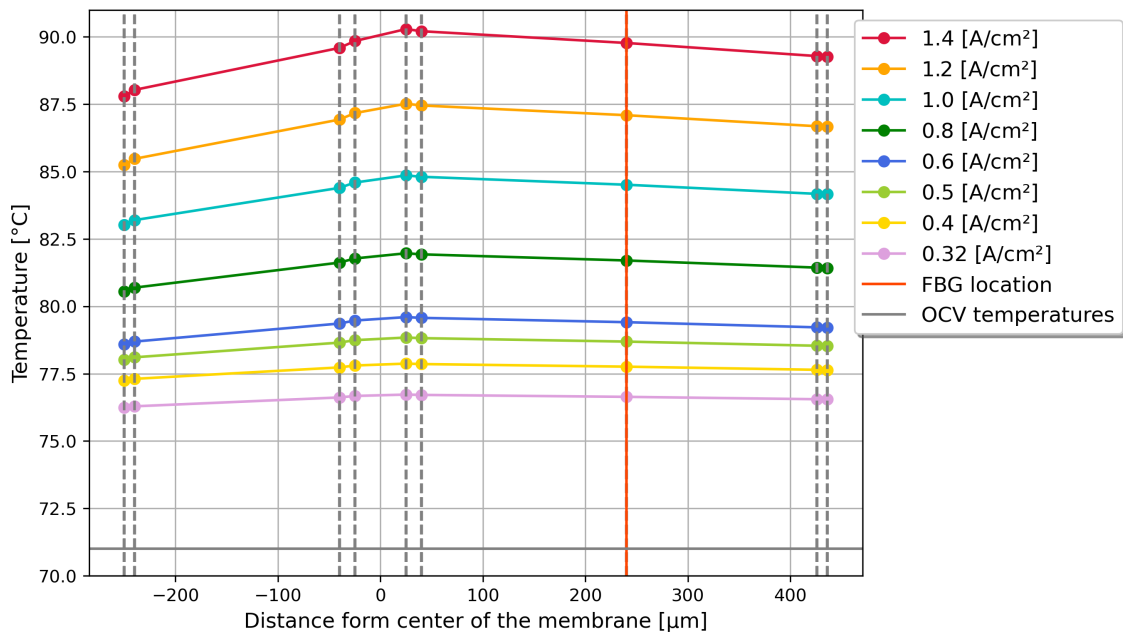
Figure 4.13: Simulated temperature profiles for the fully humidified model scenario ($\lambda = 22\ H_2O/SO_3^-$) at various current densities.
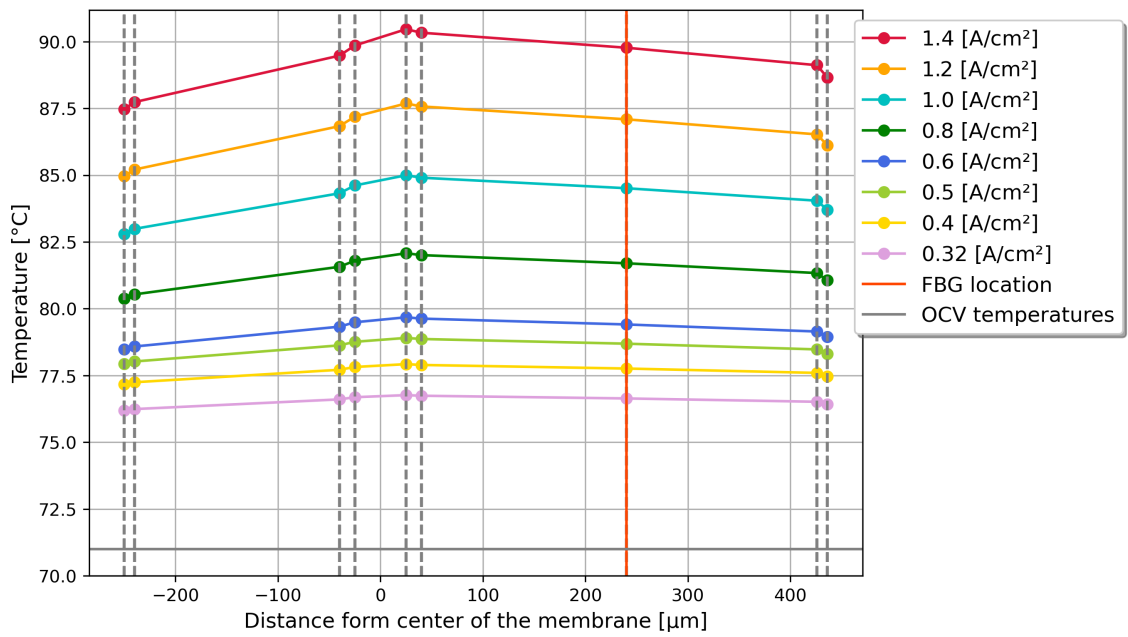
Figure 4.14: Simulated temperature profiles for the moderately humidified model scenario ($\lambda = 15\ H_2O/SO_3^-$) at various current densities.
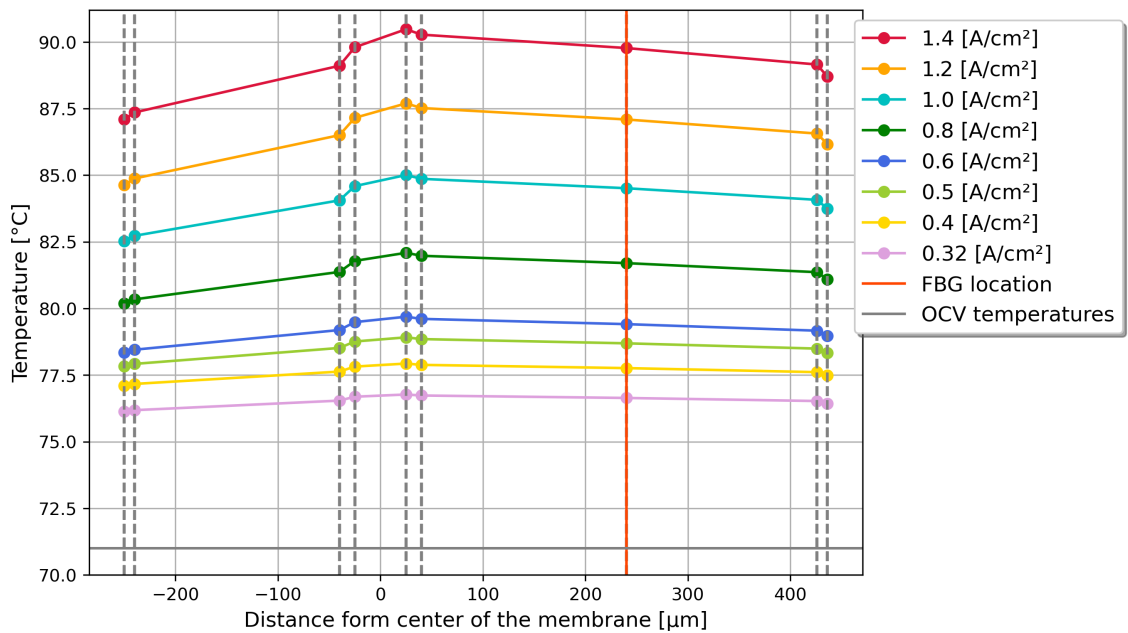
Figure 4.15: Simulated temperature profiles for the poorly humidified model scenario ($\lambda = 10\ H_2O/SO_3^-$) at various current densities.

Table 4.4: The highest temperature for all model scenarios, which was consistently found at the CCL.

| I [A]	j [A/cm^2]	Max T ($\lambda = 22$) [°C]	Max T ($\lambda = 15$) [°C]	Max T ($\lambda = 10$) [°C]
8	0.32	76.72	76.76	76.77
10	0.40	77.87	77.92	77.93
12.5	0.50	78.84	78.91	78.91
15	0.60	79.60	79.68	79.69
20	0.80	81.97	82.08	82.09
25	1.00	84.86	85.00	85.01
30	1.20	87.52	87.68	87.69
35	1.40	90.29	90.46	90.48

Lastly, the modeled temperature variations over the PEM fuel cell are given in Table 4.5. It is seen that for all three model cases, the temperature variation across the PEM fuel cell increased for higher current densities. Furthermore, lower humidity level also increases the temperature variation over the cell. This is a consequence of the reduction in thermal conductivities associated with lower humidification. It is also partly due to the increase in heat generation at the membrane for lower humidity levels.

Table 4.5: Maximum temperature difference over the PEM fuel cell for all model scenarios.

I [A]	j [A/m^2]	Δ T ($\lambda = 22$) [°C]	Δ T ($\lambda = 15$) [°C]	Δ T ($\lambda = 10$) [°C]
8	0.32	0.48	0.57	0.64
10	0.40	0.63	0.74	0.83
12.5	0.50	0.81	0.98	1.08
15	0.60	1.01	1.21	1.35
20	0.80	1.42	1.70	1.90
25	1.00	1.84	2.21	2.48
30	1.20	2.27	2.71	3.06
35	1.40	2.50	2.99	3.39

Chapter 5

Discussion

This chapter holds a thorough discussion of the thesis results, analyzing their accuracy and significance. To evaluate the results, both the temperature measurements and the simulated temperature profiles are compared to previous work in the field.

5.1 Discussion of Measured Thermal Conductivities

This section discusses the thermal conductivities found in the project thesis and compares them to what has previously been reported in the literature. The focus, however, will be on the thermal conductivities that have been incorporated into this thesis work. These include the thermal conductivity of the humidified Nafion membrane and the CLs at a 13.3 bar compaction pressure.

One immediate trend observed from the thermal conductivity results in Table 4.1, which was discussed in great detail in the project thesis, was the significant enhancement of through-plane thermal conductivity with proper humidification of the components. This was consistent with previous findings and has been shown to have a significant impact on simulated temperature profiles [14]. Based on this observation, the thermal conductivities for the Nafion membrane and CLs were changed with respect to the simulated humidity level in the three model cases of this thesis.

Firstly, humidification of the membrane showed a significant increase in measured thermal conductivity. This is consistent with findings from previous research. Burheim et al. estimated in 2009 a linear relation between the thermal conductivity and humidification level λ of a Nafion membrane [11]. This relation was found using

75

a similar measurement rig as utilized in the project thesis. The same research reported a thermal conductivity of 0.254 ± 0.016 W/mK for a fully humidified Nafion membrane, which matches exceptionally well with the 0.254 ± 0.005 W/mK thermal conductivity measured in the project thesis at 13.3 bars. The significant increase in thermal conductivity of Nafion with humidity was in the project thesis explained by the enhanced mobility. Higher water content is known to facilitate proton conductive pathways, increasing both the membrane's proton and thermal conductivity [7].

Furthermore, reported values for the thermal conductivity of the CL vary greatly. For a dry CL, these values range from 0.04 to 0.27 W/mK [28, 57, 58]. This considerable inconsistency is mainly due to the difficulty in experimentally measuring the thermal conductivity of a stand-alone CL, as the layer is typically coated on either the membrane or the GDL. Consequently, many researchers resort to estimating the CL's thermal conductivity based on measurements of the CCM and Nafion membrane thermal conductivity, which is the approach taken in the project thesis. Using a similar method, Khandelwal et al. reported the thermal conductivity of the dry CL to be $0.27 \ W/Km$ [58]. This approach, however, naturally carries a higher uncertainty due to the propagation of errors. The wide range of reported thermal conductivity values for the CL can also be explained by the large variation in CL compositions examined in various studies. In 2018, Bock et al. studied the effect of graphite and platinum loading on the thermal conductivity of the CL, discovering that both had significant influence on the thermal conductivity [57].

For humidified CLs, reported thermal conductivities are even more scarce. The only publications found on this topic were by Burheim et al. in 2014 and Eichner in 2023 [28, 51]. Burheim et al. reported values ranging from 0.12 ± 0.02 and 0.40 ± 0.9 W/mK for humidified CLs at 13.8 bars [28], whereas Eichner found a thermal conductivity of 0.67 ± 0.07 W/mK for a fully humidified CL at 13.9 bars [51]. In the project thesis, a thermal conductivity of 0.266 ± 0.212 W/mK was calculated for a fully humidified CL at 13.3 bars [7]. Despite its high uncertainty, this value falls within the range of previously reported values. It was therefore decided to proceed with this value for the fully humidified model scenario in this thesis work, due to the lack of a better alternative. However, lower values were chosen for the remaining two model cases based on previously measured values. Further investigation into the thermal conductivity of different CL compositions and humidification levels will be needed to reduce the uncertainty associated with these values.

5.2 Calibrations and Temperature Measurements at the Cathode GDL

The ex-situ calibration of the FBG had a temperature sensitivity of 0.0096 nm/°C, which is in good agreement with the literature [10, 38]. For the in-situ calibrations, however, a temperature sensitivity of 0.01427 nm/°C was found. This is significantly higher than the 0.0107 nm/°C sensitivity recorded by Nigel et al. during their in-situ calibration within a PEM fuel cell housing [9]. In contrast, they had milled sufficiently deep channels for the FBG to lie in, which in turn meant that the FBG was not compressed by the MEA. They also drilled channels into the cell housing to prevent the fiber from being fixed by the cell housing. In this thesis work no alterations to the cell housing were made, meaning there was no way around the optical fiber being fixed by the cell housing. Instead, the strain was limited by adding a second GDL and cutting the optical fiber on one end of the FBG. This meant the fiber was fixed on one end of the FBG between two gaskets and the cell housing, while the cut end laid within the cell's active area. It is evident that this layout is not fully isolated from strain, which is the sole reason behind performing in-situ calibrations. However, the measured temperature sensitivity above the theoretical sensitivity of 0.01 nm/°C further indicates that the strain was not constant over the temperature interval.

As the compaction pressure remained constant during the calibrations, some other factors must contribute to the induced strain observed at increasing temperatures. One possible explanation is the thermal expansion of the fuel cell housing material at higher temperatures. Since the optical fiber was fixed at one end of the FBG by the cell housing, a thermal expansion of the cell housing would induce strain on the FBG. The presence of temperature-induced strain underlines the importance of performing in-situ calibrations, as assuming a temperature response of 0.01 nm/°C would have significantly altered the temperature reading.

Additionally, it was observed that even a slight shift in the position of the FBG influenced its temperature response. Upon analysis of the temperature measurements, it was revealed that moving the FBG between the calibration and the temperature recording significantly affected the output temperatures. Despite not knowing this at the time, all calibrations and temperature measurements at the cathode were conducted at the same exact location, ensuring the accuracy of the cathode temperature data. This accuracy was further validated by the OCV temperature measurement of 70.6°C, consistent with the set operating conditions for the PEM fuel cell.

Having established the reliability of the temperature response from the in-situ calibrations at the cathode, this section will now proceed to evaluate the resulting temperature measurements in relation to the current density. The real-time temperature measurements at the cathode GDL for different operating currents were shown in Figure 4.7, where the FBG shows a good temporal response to changes in current. The evaluation of these FBG-measured temperature results, will be done through comparison with similar experiments. However, directly comparing in-situ temperature measurements of PEM fuel cells is challenging due to the large variation in fuel cell performance and specified operating conditions between the experiments. Therefore, the evaluation of the temperature results will focus on comparing the temperature rise recorded for increasing current density steps. While this parameter is not entirely invariant with operating conditions and fuel cell performance, it offers a more consistent basis for comparison.

Real-time temperature measurements within a PEM fuel cell have been conducted in a series of studies. However, to the author's knowledge, only one study, conducted by Nigel et al. in 2009, has used FBGs for this exact purpose [9]. In their study, they used a series of four FBGs for temperature sensing at the lands between the flow channels on the cathode. They measured temperatures for varying currents between 6 to 12 A within a laboratory PEM fuel cell with a 30.25 cm^2 active area. For the corresponding current densities of approximately 0.33 to 0.4 A/cm^2, they measured a temperature increase between 0.5 and 1.0 °C depending on the in-plane position of the FBG. In this study, a temperature increase of 1.12 °C was found at the cathode GDL from 0.32 to 0.4 A/cm^2 at the center of the 25 cm^2 active area. The slightly higher temperature increase observed in this study is to be expected because the FBG is positioned within the MEA, closer to the largest heat sources, rather than in the flow channels. Hence, the measured temperature increase with current density correlates well with their findings.

Furthermore, it is valuable to compare the temperature measurements with what is recorded using other sensing technologies. Vie and Kjelstrup were the first to measure the through-plane temperature distribution of a PEM fuel cell [20]. They used a total of four micro-thermocouples, one on each side of the membrane and one in each of the gas channels. However, the large thermocouple diameter of 280 μm, in comparison to the CL thickness of 10 μm, made the through-plane position of the thermocouples challenging to define. Regardless, the thermocouples next to the membrane measured an average temperature increase of 12.5 °C between OCV and 1.0 A/cm^2, while the thermocouples at the gas channels measured a temperature increase of approximately 8 and 7 °C over the same range at the anode and cathode respectively. The temperature increase in this study was 13.9 °C at the

cathode GDL over the same current density range. The higher temperature rise in this study can be explained by the sensor limitations of the thermocouples used by Vie and Kjelstrup. Firstly, the micro-thermocouples had to be chemically and electrically isolated, which increases their uncertainty. This causes the recorded thermocouple temperatures to be lower than the real temperature [20]. Moreover, the thermocouples were much larger than the optical fiber used in this study, in addition to having a much smaller active area of 5 cm^2. Consequently, the thermocouples blocked a higher percentage of the active area, impacting the heat generation to a larger extent than the optical FBG sensor did. Due to these limitations, they reported the measurements as minimum temperatures [20]. With these limitations in mind, the higher temperature rise measured in this thesis is considered valid.

Further, in 2009 Lee et al. employed a similar method as Vie and Kjelstrup to measure the through-plane temperature in a single PEM fuel cell [21]. However, they enhanced the approach by using three additional micro-thermocouples for more detailed temperature distribution analysis and calibrated their thermocouples to achieve a precision of ± 0.1°C despite the thermocouple insulation [21]. Similar to this study, they positioned two GDLs with a micro-thermocouple between them at both the anode and cathode to determine the GDL temperatures. With this sensor integration, they measured the through-plane temperature distribution for current densities up to 0.6 A/cm^2. The thermocouple between the two GDLs at the cathode recorded a temperature increase of approximately 0.6 °C as the current density increased from 0.4 to 0.6 A/cm^2.

In this thesis work, a temperature increase of 1.65 °C was measured over the same current density range. Due to the calibration and reduction in thermocouple diameter, the lower temperature difference can no longer be explained by the sensor limitations of the thermocouples. Instead, the 1 °C difference can be explained by temperature variations in the in-plane position. It has previously been reported large temperature variations in the in-plane direction of PEM fuel cells. For instance, Nigel et al. measured over 1 °C temperature difference upstream and downstream of the cathode flow field [9]. Furthermore, Lee et al. reported large fluctuations in the overpotential at 0.6 A/cm^2 and the cathode temperatures accordingly. They attributed these fluctuations to the dynamic behavior of liquid water at the cathode, where droplets form and burst randomly [21]. These temperature fluctuations at 0.6 A/cm^2 introduced a higher uncertainty tied to the reported temperature, although the exact uncertainty was not specified in the report. Taking these factors into account, the 1 °C higher temperature increase measured by the FBG for the same current density step is reasonable.
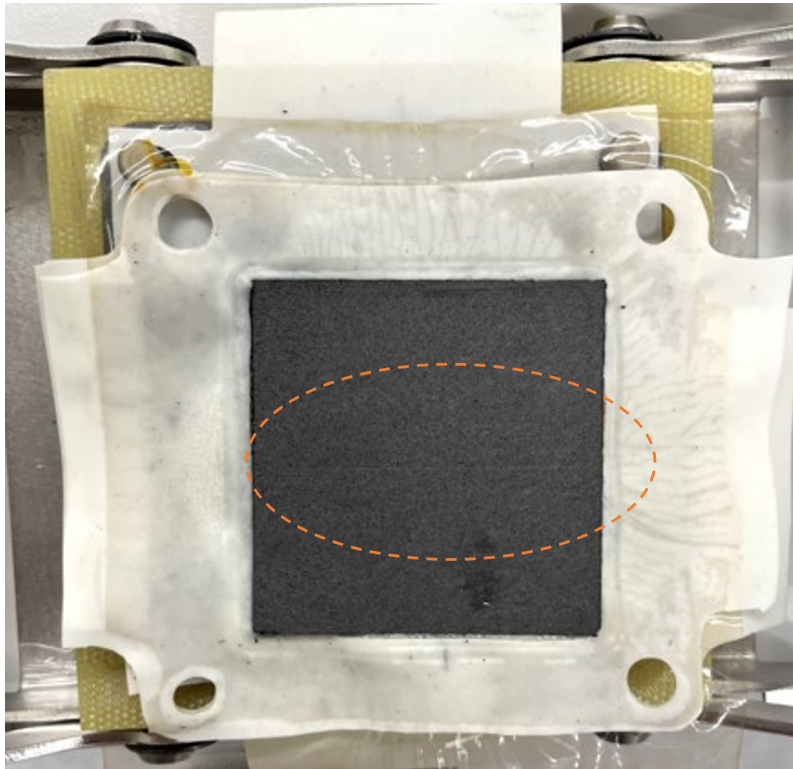
Figure 5.1: Image of the trace left by the FBG on the anode Sigracet GDL.

5.3 Calibration and Temperature Measurements at the Anode GDL

An anode calibration was not accurately performed before the measurements as the FBG sensitivity to fuel cell location was not yet discovered. Furthermore, any attempt made to calibrate the FBG at the anode at a later time failed to recreate the strain experienced by the FBG during the temperature measurements. To translate the detected Bragg wavelengths into a reasonable temperature response over the current stepping, a much smaller strain had to be assumed than what was recorded by previous calibrations. The reason for the significantly lower strain on the FBG during the anode temperature measurements can be explained by an imprint left by the optical fiber on the anode GDL, shown in Figure 5.1. Such an imprint will reduce the effective compaction pressure felt by the FBG, and consequently reduce the strain. An equivalent trace was not found on the cathode GDL, explaining the higher strain effects on the cathode measurements.

Assuming the OCV temperature, the anode GDL temperature could be estimated using similar temperature responses as seen for the calibrations. Even though the strain impact from the compaction pressure was assumed to be significantly lower, the temperature-induced strain from the thermal expansion of the cell housing was

thought to be the same. With this approach, a reasonable upper and lower temperature range for each current density could be estimated.

The anode temperature estimations show a different temperature response compared to the measured cathode temperatures over the same current densities as seen in Figure 4.11. Firstly, the temperature jump from the OCV to 8 A is estimated to be much smaller at the anode than what is measured at the cathode. Furthermore, at 8 A there is a 3.2 °C mean temperature gap between the estimated anode temperature and the measured cathode temperature. However, this gap closes for higher current densities, and at 30 A the upper estimated anode temperature exceeds the measured cathode temperature. It is worth noting that the anode GDL is expected to have a lower temperature than the cathode GDL due to the PEM fuel cell characteristics. This is because the cathode overpotential provides the largest heat source in the PEM fuel cell. However, the temperature difference between the anode and cathode GDL is expected to increase for higher currents, and not decrease as seen in Figure 4.11.

The challenge of performance reproducibility is one explanation for the difference in temperature response to increasing currents. As shown in Figure 4.8, a second conditioning was needed to obtain a similar fuel cell performance over the current-stepping. Still after conditioning, the same I-V relation as seen during the cathode GDL temperature measurements were not obtainable. This was most likely due to the change in PEM fuel cell composition as the second GDL was moved to the anode for the measurements.

For currents between 8 and 10 bars, the drop in potential is smaller during the anode temperature measurements, which also means that the fuel cell heat generation was lower for these currents. Hence, a larger temperature variation than normal can be expected between the anode and cathode GDL measurements. At 15 A, however, the cell potentials are quite similar. Here the mean temperature gap has reduced to 2.2 °C. This is still slightly higher than expected from literature where the variation is modeled or measured to be less than 1.5 °C [17, 20, 21]. However, this invariance is reasonable due to the slight difference in performance and the difference in cell composition between the measurements. It can also be explained by the high uncertainty of the estimated anode temperature. At higher currents, however, the performance was significantly worse during the anode temperature measurements than the cathode ones. Consequently, there would have been a higher heat generation during the anode measurements, explaining why the temperature gap closes at higher currents.

5.4 Evaluation of Modeled Losses in Comparison to Experimental Results

In the last section, we discussed the challenge of achieving consistent PEM fuel cell performance between the cathode and anode temperature measurements. Since similar performance was not attainable, it was decided to only use the cathode temperature measurements as a boundary layer in the model. Therefore, the polarization curve obtained before the cathode temperature measurements was used to model the fuel cell's activation losses using the Tafel equation.

Firstly, it is worth noting that the shape of the polarization curve measured after cell-conditioning deviates from polarization curves for a PEM fuel cell run on air and hydrogen. Although air is the most common oxidant used in the industry, PEM fuel cells supplied with air experience higher concentration losses compared to those supplied with pure oxygen at a stoichiometric rate. To model these concentration losses accurately, an appropriate limiting current was selected.

In Figure 4.12, the modeled cell potential is shown with respect to the current density and humidification level in comparison to the polarization curve created after conditioning. The modeled potential is found by subtracting the modeled activation, concentration, and ohmic losses from the measured OCV. For a humidity level λ of 10 water molecules per sulfonic group, the modeled cell potential fits nicely with the experimental values for current densities below 0.8 A/cm^2, while the modeled cell potential starts to deviate from the experimental values at even lower current densities for higher humidity levels.

The deviation at higher current densities is most likely explained by polarization sources neglected in the model. In 2009, Williams et al. did a detailed analysis of the several polarization sources taking place in a PEM fuel cell, which included various ohmic, activation, and concentration sources [59]. Several of these are accounted for in this thesis, but a few are neglected. Firstly, the model includes ohmic losses related to the electrical resistance in the CLs, GDLs, and BPs in addition to the ionic resistances. At lower current densities the losses related to the electric resistances are small and are therefore commonly neglected by simple models. However, they were included in this model as they were seen to have a significant impact for current densities above 1 A/cm^2. Yet, the ohmic losses from the electric contact resistances between the components are not included due to a lack of information on their value. They may, however, be partly the reason for the model's deviation from the experimental values at higher current densities. Furthermore, the elev-

ated membrane temperatures resulting from higher current densities risk reducing the ionomer's water uptake, thereby increasing ionic resistance. Consequently, the highest current densities may experience even lower levels of humidification [16]. Regardless, the modeled cell potential is sufficient for simulating the through-plane temperature distribution based on the experimental measurements obtained in the project and this thesis work.

5.5   Evaluation of Simulated Temperature Profiles

The modeled temperature profile for the three model cases with varying humidification levels is presented in Figures 4.13 - 4.15. The real humidity level of the PEM fuel cell was unknown during the testing. However, it is expected to lay within the range of the model cases. Furthermore, the modeled temperature variation between the BP for all model cases is given in Table 4.5. As seen from Table 4.5, the temperature variation increases for higher current densities and lower humidity levels. The increase in temperature variation at higher current densities is tied to increased heat generation and a higher modeled through-plane heat flux, as temperature distribution and heat flux are related by Fourier's law. This trend is consistent with findings from other studies.

For instance, Lee et al. measured a temperature variation between the gas channels of a single PEM fuel cell of approximately 1 °C at 0.6 A/cm^2, in comparison to a 0.5 °C temperature variation at 0.4 A/cm^2 and zero temperature variation at OCV [21]. This is close to the modeled temperature variation for $\lambda = 22$ at the same current densities. Furthermore, Zhang et al. measured the temperature drop from the CCL to the cathode flow plate for different cell voltages. They measured an increase in temperature drop from 0.5 °C at 0.8 V to 4 °C at 0.4 V [60]. These experimentally measured temperature variations build under the credibility of the modeled temperature profiles in this work as all of the modeled temperature drops, seen in Table 4.5, lay within this range.

To further evaluate the modeled temperature variations with respect to current density, it is useful to compare it to other PEM fuel cell models. As the actual temperatures are largely dependent on the cell temperature chosen for the model it is not possible to compare the temperatures directly. Instead, the temperature variations across the cell are more suitable for comparison. In 2015, Cao et al. designed a 3D model to investigate the effect of thermal contact resistance (TCR) between the GDL and the BP on the modeled temperature profile [17]. They found includ-

ing the TCR had a significant impact on the modeled temperature distribution, and the CCL temperature. Since the model in this thesis also accounts for TCR, their results provide a good basis for comparison. Accounting for TCR, they simulated the temperature profile for fuel cell voltages between 0.4 and 0.9 V. At 0.4 V they modeled a 3.5 °C temperature drop over the MEA, which decreased to a 2 °C drop for 0.6 V. A cell potential of 0.6 V correlates to the model cases at 8000 A/m^2 where a temperature drop over the MEA were found to lie between 1.34 and 1.87 °C depending on the water content λ. This difference is reasonable considering the model of Cao et al. considered higher polarization sources in their model resulting in increased heat generation.

The maximum temperature of for all model cases were found at the CCL, which agree with the model by Cao et al. that found the maximum temperature to consistently lay near the CCL [17]. Lee et al., however, experimentally measured the maximum temperature either at the CCL or in the center of the PEM [21]. The instances where the PEM temperature surpassed the CCL temperature occurred during the cell's ramp-up phase. Hence, it could be explained by poor water content in the membrane, leading to a higher ionic resistance compared to the ramp-down case.

In addition to the temperature variations increasing with current density, the model in this thesis also simulates higher variations for lower PEM fuel cell humidity levels. This is due to the reduced thermal conductivities of PEM fuel cell components associated with lower water content, as defined by Fourier's law. Additionally, the membrane exhibits higher ionic resistance at lower water content, resulting in increased ohmic losses. Consequently, also higher ohmic heat generation contributes to the higher temperature variations observed at lower water contents.

In 2017 Burheim reviewed how the last decade of research into the thermal conductivities of PEM fuel cell materials had altered our understanding of the internal temperature profile [14]. In this review, he demonstrated a significant reduction in temperature difference across a fully humidified PEM fuel cell ($\lambda = 22$) compared to a less humidified cell ($\lambda = 15$) when operated at 10 000 A/m^2. For the latter ($\lambda = 15$) he simulated a temperature drop from the CCL to the flow field of 9 °C, which was reduced to a 3.5 °C drop for his fully humidified model case ($\lambda = 22$). For the same current density, the model in this thesis simulates much smaller temperature variations across the PEM fuel cell. In the fully humidified model case ($\lambda = 22$), a temperature variation of 1.69 °C was simulated, which increased to 2.05 °C in the moderately humidified model case ($\lambda = 15$).

This significant difference in the simulated through-plane temperature profile is

partly due to variations in model specifications, such as the components' compositions, thicknesses, and thermal conductivities. Furthermore, defining a constant temperature boundary condition at the back of the BP, as done by Burheim and most numerical models, is not without errors. This assumption only holds for small current densities and has been contradicted by a series of experimental results [17]. For instance, measured temperature gradients in the cathode end plate were observed in this thesis work when running the PEM fuel cell at higher currents, despite keeping the cooling water temperature constant. Cao et al. recognized the limitations of this boundary condition and redesigned the backside flow plate boundary condition of their 3D model by applying a constant heat transfer coefficient to the cooling fluid [17]. They found that altering the boundary condition significantly impacted the temperature profile simulation.

Furthermore, this thesis study maintains a constant cathode GDL temperature, as measured by the FBG, across all three modeling scenarios. While in reality, the GDL temperature would vary with humidification, this approach was chosen to focus on determining the true humidity level rather than examining changes in temperature distribution with different humidity levels.

5.6 Comparing Simulated Temperature Profiles with Anode GDL Measurements

When comparing the cell potentials during the cathode and anode temperature measurements in Figure 4.8, it is seen that they are best correlated at the 15 A or 0.6 A/cm^2 current step. It can therefore be assumed that the heat generation in the cell was similar between the two measurements for this current, and is a good basis for comparison. Furthermore, at 0.6 A/cm^2 it is seen from Figure 4.12 that the model case for λ equal to 10 water molecules per sulfonic group is a great fit with the experimentally measured IV-relationship of the cell. Hence, it is interesting to compare the anode estimated temperature range at 0.6 A/cm^2 for the model case at the same current density and λ equal 10.

A closer look at this specific model case is given in Figure 5.2, which shows that the model simulation predicts a higher temperature at the anode GDL than what is estimated from the FBG measurements. This can partly be explained by the difference in cell assembly between the anode and cathode temperature measurements. There would most likely be more heat in the anode direction during the cathode temperature measurements due to the higher cathode thermal resistance associated

with the additional GDL. The same goes for the anode temperature measurements, where more of the heat flux is expected to leave through the cathode end plate.

There is also a high uncertainty tied to the estimated anode temperatures. If the temperature response assumption between 0.0144 and 0.0127 nm/°C was overestimated, it could explain why one measured lower temperatures than simulated. For instance, if the true temperature sensitivity during the measurements were 0.011 nm/°C, the estimated anode temperature would rather be 78.5 °C, which agrees nicely with the temperature simulation. Overall, it can be concluded that this work failed to accurately measure the anode GDL temperatures for varying loads. Hence it is recommended for future studies to execute proper calibrations of the FBG for each new PEM fuel cell location. Furthermore, simultaneously measuring the temperatures at various PEM fuel cell locations would be advantageous, which was not executed in this study due to equipment limitations.

The estimated anode GDL temperature ranges are compared to all the model scenarios and currents in Appendix B. However, these were excluded from the discussion due to the reproducibility issue shown in Figure 4.8 for all other currents than 15 A.

5.7 Evaluating the Water Content of The PEM Fuel Cell

The exact water content during the PEM fuel cell testing is not known. It also most likely changed over the operation periods. However, some conclusions can be made. Firstly, it is unlikely for a PEM fuel cell to be fully humidified ($\lambda = 22$) during operation, as this uptake is only obtainable for the Nafion membrane when submerged in water [46]. Furthermore, water contents above 15 water molecules per sulfonic group are attainable, but challenging to obtain if using the standard conditioning method of voltage cycling with humidified gas. The maximum water uptake of Nafion in a PEM fuel cell supplied with gases with a 100% relative humidity is approximately 15 water molecules per sulfonic group [61]. Higher water content can be obtained by allowing for condensation during the conditioning, for example by temperature cycling as demonstrated by Bezmalinovic et al. in 2014 [43].

In this work, a traditional method for conditioning was applied, which included voltage stepping at a relative humidity of 100%. Hence, it is reasonable to assume that the initial water content was equal to or less than 15 water molecules per sulfonic
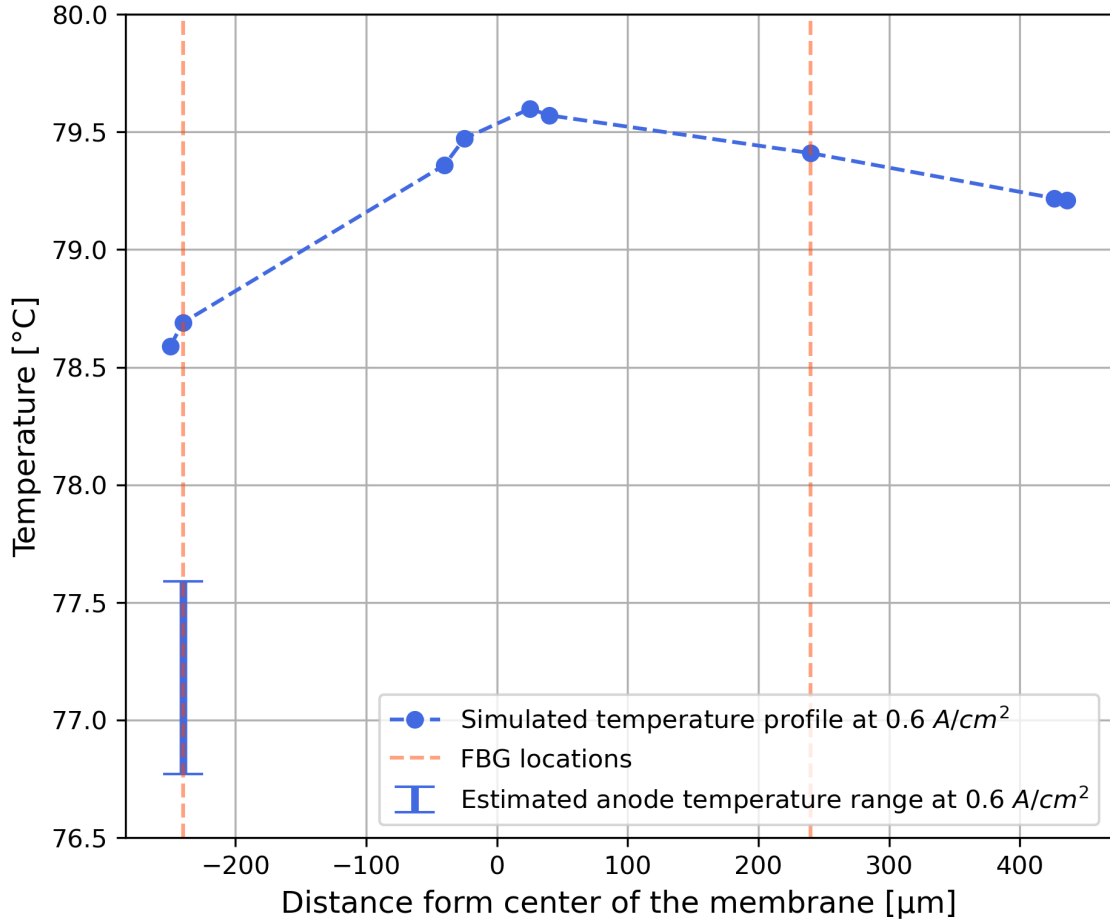
Figure 5.2: Comparison of the modeled temperature profile with the experimentally determined temperature range from the FBG measurements at the anode GDL for a current density of 0.6 A/cm^2 and a humidity level of 10 H_2O/SO_3^-.

group after the conditioning. However, during the testing, the relative humidity was reduced to 70%, which may reduce the humidity level over time. There is also a possibility for humidity reduction due to elevated membrane temperatures at higher current densities. With all this in mind, one can conclude that the humidity level during testing was most likely lower than 15 water molecules per sulfonic group. Hence, the least humidified model case best represents the true temperature distribution experienced by the PEM fuel cell during testing. This is highlighted by the fact that the model scenario at λ equals 10 aligns best with the polarization curve measured after conditioning.

Chapter 6

Conclusion

6.1   Conclusion

In conclusion, this thesis has provided a comprehensive investigation into the temperature profile across a PEM fuel cell through both experimental techniques and numerical modeling. The in-situ temperature measurements obtained at the cathode GDL have showcased the use of optical FBGs for this exact purpose, where the FBG was proven to have a rapid temporal response.

Furthermore, a significant temperature increase of 13.13 °C between 0.32 and 1.40 A/cm^2 was recorded using the FBG sensor. The observed temperature rise was validated through comparison with similar experiments, despite being slightly higher compared to previous measurements obtained through other sensing technologies. However, this difference was attributed to variations in sensor precision, placement, and the PEM fuel cell behavior. Based on this examination, the temperature readings taken at the cathode GDL were deemed reliable. Further comparison of these measurements with the temperature at the graphite plate concludes significant temperature gradients within the PEM fuel cell at higher current densities.

Furthermore, the implementation of empirically measured data into a one-dimensional model has raised important questions regarding general model designs. The simulated temperature profiles varied greatly from those assuming a constant graphite temperature but correlated well with models applying a constant heat transfer coefficient instead. It was concluded that assuming a constant graphite plate temperature is an inadequate assumption for thermal PEM fuel cell models. This conclusion was further supported by the approximately 2 °C temperature variation measured at the back of the graphite plate in this study.

Overall, this thesis emphasizes the significant temperature variations across a PEM fuel cell and the importance of empirical data to validate PEM fuel cell models. In the long term, these insights contribute to enhancing thermal management strategies and optimizing the performance of PEM fuel cells.

6.2   Suggestions for Further Work

The initial work of this thesis successfully demonstrated the use of FBGs for in-situ temperature measurements at the cathode GDL. However, despite this thesis presenting valuable results, it was not without shortcomings. The experimental setup in this thesis only allowed for one FBG integration at a time. To overcome this limitation, future researchers should explore the adoption of a fiber optic setup capable of accommodating multiple optical fibers. Such an approach would enable simultaneous temperature measurements at various through-plane or in-plane locations. This would also eliminate the reproducibility problem observed in this thesis between the cathode and anode temperature measurements.

Moreover, the investigation into FBG sensors for temperature sensing within a PEM fuel cell is currently limited to this study and the work by Nigel et al. in 2009 [9]. Both studies indicate a promising future for FBG sensors for in-situ temperature measurements. However, further research is necessary to fully understand and realize their potential. Future efforts should also focus on extending these implementation techniques to stack monitoring.

Furthermore, no conclusions were made for the anode GDL temperatures, only estimations based on broad assumptions. This was caused by the FBG experiencing significantly less strain, making the original calibrations unsuitable for accurately representing the temperature response. Hence, further work is needed to investigate the anode GDL temperature. This failed attempt also underlines the strain sensitivity of FBGs and highlights the importance of proper calibrations. In conclusion, accurate calibrations are essential for FBG applications in environments where negligible strain cannot be ensured. It is therefore suggested to perform a minimum of one new calibration at each new sensor position in all future work utilizing FBGs for temperature sensing.

The reason behind the reduction in strain experienced by the FBG at the anode GDL was in the discussion traced back to an imprint left by the optical fiber, as shown in Figure 5.1. This finding suggests the potential for further minimizing strain by carving sufficiently small traces for the optical fiber to lay in. Reducing strain is

essential for enhancing the reliability of FBG measurements. Therefore, this aspect should be further investigated to unlock the full potential of FBGs as commercial temperature sensors for PEM fuel cells.

In the second part of this thesis, it was revealed that integrating experimental data into numerical models significantly altered the simulated temperature profiles in comparison to other model designs. For the further development of accurate PEM fuel cell models, it was concluded that empirical data is essential to fine-tune the model designs. To build on the model presented in this thesis, it is recommended to introduce an additional constant temperature condition on the anode. Additionally, future efforts should explore the implementation of empirical data into more complex models of the PEM fuel cell, as the scope of this thesis was limited to a simple one-dimensional model design.

Lastly, it is worth noting that the measurements and modeling conducted in this thesis were confined to a specific set of operating conditions. To gain a comprehensive understanding of the thermal behavior of PEM fuel cells, future research should conduct similar experiments and numerical modeling across a broad range of operating conditions.

References

[1] United Nations (UN), *The Paris Agreement*, United Nations, URL: https://www.un.org/en/climatechange/paris-agreement (visited on 6th Apr. 2024).

[2] United Nations (UN), *Sustainable Development Goals*, United Nations, URL: https://sdgs.un.org/goals (visited on 22nd May 2024).

[3] International Energy Agency (IEA), *Net Zero by 2050*, tech. rep., Paris: IEA, 2021, URL: https://www.iea.org/reports/net-zero-by-2050.

[4] O. S. Burheim, 'Chapter 1 - Energy Storage', in: *Engineering Energy Storage*, ed. by O. S. Burheim, London: Academic Press, 2017, pp. 1–15, DOI: https://doi.org/10.1016/B978-0-12-814100-7.00001-8.

[5] Intergovernmental Panel on Climate Change (IPCC), 'Summary for Policymakers', in: *Climate Change 2022 - Mitigation of Climate Change: Working Group III Contribution to the Sixth Assessment Report of the Interis their a short cut governmental Panel on Climate Change*, Cambridge University Press, 2023, p. 28, DOI: 10.1017/9781009157926.001.

[6] O. S. Burheim, 'Chapter 8 - Hydrogen for Energy Storage', in: *Engineering Energy Storage*, ed. by O. S. Burheim, First Edition, London: Academic Press, 2017, pp. 147–192, DOI: https://doi.org/10.1016/B978-0-12-814100-7.00008-0.

[7] M. H. Hasselø, 'Optical and traditional detection of thermal balance in green hydrogen systems', Project thesis, Department of Energy and Process Engineering, Norwegian University of Science and Technology (NTNU), Trondheim, Norway, Jan. 2024.

[8] J. J. Lamb, O. S. Burheim and B. G. Pollet, 'Hydrogen Fuel Cells and Water Electrolysers', in: *Micro-Optics and Energy: Sensors for Energy Devices*, ed. by J. J. Lamb and B. G. Pollet, Cham, Switzerland: Springer International Publishing, 2020, pp. 61–71, DOI: 10.1007/978-3-030-43676-6_6.

[9]   N. A. David, P. M. Wild, J. Hu and N. Djilali, 'In-fibre Bragg grating sensors for distributed temperature measurement in a polymer electrolyte membrane fuel cell', in: *Journal of Power Sources* vol. 192., no. 2 (2009), pp. 376–380, DOI: https://doi.org/10.1016/j.jpowsour.2009.03.021.

[10] M. S. Wahl, L. Spitthoff, H. I. Muri, A. Jinasena, O. S. Burheim and J. J. Lamb, 'The Importance of Optical Fibres for Internal Temperature Sensing in Lithium-ion Batteries during Operation', in: *Energies* vol. 14., no. 12 (June 2021), DOI: 10.3390/en14123617.

[11] O. Burheim, P. J. S. Vie, J. G. Pharoah and S. Kjelstrup, 'Ex situ measurements of through-plane thermal conductivities in a polymer electrolyte fuel cell', in: *Journal of Power Sources* vol. 195., no. 1 (Jan. 2010), pp. 249–256, DOI: 10.1016/j.jpowsour.2009.06.077.

[12] P. J.S. Vie, 'Characterisation and optimisation of the polymer electrolyte fuel cell', PhD thesis, Department of Chemistry, Norwegian University of Science and Technology (NTNU), Trondheim, Norway, 2002 [Online], URL: http://hdl.handle.net/11250/244546.

[13] R. Bock, A. D. Shum, X. Xiao, H. Karoliussen, F. Seland, I. V. Zenyuk and O. S. Burheim, 'Thermal Conductivity and Compaction of GDL-MPL Interfacial Composite Material', in: *Journal of The Electrochemical Society* vol. 165., no. 7 (May 2018), F514–F525, DOI: 10.1149/2.0751807jes.

[14] O. S. Burheim, '(Invited) Review: PEMFC Materials' Thermal Conductivity and Influence on Internal Temperature Profiles', in: *ECS Transactions* vol. 80., no. 8 (2017), pp. 509–525, DOI: 10.1149/08008.0509ecst.

[15] B. Hamre, 'Thermal Conductivity in PEMFC PTLs with Different Gas Content and Corresponding simple PEMFC Internal Temperature Profiles', Master's Thesis, Department of Energy and Process Engineering, Norwegian University of Science and Technology (NTNU), Trondheim, Norway, 2020, URL: http://hdl.handle.net/11250/2457556.

[16] P. A. García-Salaberri and A. Sánchez-Ramos, 'Modeling of a polymer electrolyte membrane fuel cell with a hybrid continuum/discrete formulation at the rib/channel scale: Effect of relative humidity and temperature on performance and two-phase transport', in: *Applied Energy* vol. 367 (2024), DOI: https://doi.org/10.1016/j.apenergy.2024.123332.

[17] T.-F. Cao, Y.-T. Mu, J. Ding, H. Lin, Y.-L. He and W.-Q. Tao, 'Modeling the temperature distribution and performance of a PEM fuel cell with thermal contact resistance', in: *International Journal of Heat and Mass Transfer* vol.

87 (2015), pp. 544–556, DOI: https://doi.org/10.1016/j.ijheatmasstransfer.2015.04.010.

[18]   K. Inman and X. Wang, 'In-Situ Temperature Measurement on Cathode GDL in a PEMFC Using an Optical Fiber Temperature Sensor', in: *Journal of The Electrochemical Society* vol. 160., no. 6 (Mar. 2013), F496–F500, DOI: 10.1149/2.048306jes.

[19]   V.A.R. Ilie and S. Martemianov and A. Thomas, 'Investigation of the local temperature and overheat inside the membrane electrode assembly of PEM fuel cell', in: *International Journal of Hydrogen Energy* vol. 41., no. 34 (2016), pp. 15528–15537, DOI: https://doi.org/10.1016/j.ijhydene.2016.04.103.

[20]   P. J. Vie and S. Kjelstrup, 'Thermal conductivities from temperature profiles in the polymer electrolyte fuel cell', in: *Electrochimica Acta* vol. 49., no. 7 (Mar. 2004), pp. 1069–1077, DOI: https://doi.org/10.1016/j.electacta.2003.10.018.

[21]   S.-K. Lee, K. Ito, T. Ohshima, S. Noda and K. Sasaki, 'In Situ Measurement of Temperature Distribution across a Proton Exchange Membrane Fuel Cell', in: *Electrochemical and Solid-State Letters* vol. 12., no. 9 (June 2009), B126–B130, DOI: 10.1149/1.3152331.

[22]   M. Wilkinson et al., 'In Situ Experimental Technique for Measurement of Temperature and Current Distribution in Proton Exchange Membrane Fuel Cells', in: *Electrochemical and Solid-State Letters* vol. 9., no. 11 (Aug. 2006), A507–A511, DOI: 10.1149/1.2338769.

[23]   M. C. Williams, 'Chapter 2 - Fuel Cells', in: *Fuel Cells: Technologies for Fuel Processing*, ed. by D. Shekhawat, J. J. Spivey and D. A. Berry, Amsterdam: Elsevier, 2011, pp. 11–27, DOI: https://doi.org/10.1016/B978-0-444-53563-4.10002-1.

[24]   L. Mølmen, 'Durability Evaluation of PEM Fuel Cell Components', PhD thesis, Department of Electrification and Reliability, Jönköping University, Borås, Sweden, 2023 [Online], URL: https://www.diva-portal.org/smash/get/diva2:1756150/FULLTEXT01.pdf.

[25]   J. Larminie and A. Dicks, 'Introduction', in: *Fuel Cell Systems Explained*, second, Chichester, UK: John Wiley & Sons, 2003, chap. 1, pp. 1–24, DOI: https://doi.org/10.1002/9781118878330.ch1.

[26]   F. C. Store, *Membrane Electrode Assemblies (MEA)*, URL: https://www.fuelcellstore.com/fuel-cell-components/membrane-electrode-assembly (visited on 22nd Nov. 2023).

[27] J. Larminie and A. Dicks, 'Proton Exchange Membrane Fuel Cells', in: *Fuel Cell Systems Explained*, second, Chichester, UK: John Wiley & Sons, 2003, chap. 4, pp. 67–119, DOI: https://doi.org/10.1002/9781118878330.ch4.

[28] O. S. Burheim, H. Su, H. H. Hauge, S. Pasupathi and B. G. Pollet, 'Study of thermal conductivity of PEM fuel cell catalyst layers', in: *International Journal of Hydrogen Energy* vol. 39., no. 17 (May 2014), pp. 9397–9408, DOI: https://doi.org/10.1016/j.ijhydene.2014.03.206.

[29] U.S. Department of Energy at the Hydrogen and Fuel Cell Technologies Office, *Parts of a Fuel Cell*, URL: https://www.energy.gov/eere/fuelcells/parts-fuel-cell (visited on 8th Feb. 2024).

[30] O. S. Burheim, 'Chapter 6 - Electrochemical Energy Storage', in: *Engineering Energy Storage*, ed. by O. S. Burheim, London: Academic Press, 2017, pp. 75–110, DOI: https://doi.org/10.1016/B978-0-12-814100-7.00006-7.

[31] J. Larminie and A. Dicks, 'Operational Fuel Cell Voltages', in: *Fuel Cell Systems Explained*, second, Chichester, UK: John Wiley & Sons, 2003, chap. 3, pp. 45–66, DOI: https://doi.org/10.1002/9781118878330.ch3.

[32] G. Tsotridis, A. Pilenga, G. De Marco and T. Malkow, *EU Harmonised Test Protocols for PEMFC MEA Testing in Single Cell Configuration for Automotive Applications*, JRC Science for Policy report EUR 27632 EN, European Commission, Joint Research Centre, 2015, DOI: 10.2790/54653.

[33] N. David, P. Wild, J. Jensen, T. Navessin and N. Djilali, 'Simultaneous In Situ Measurement of Temperature and Relative Humidity in a PEMFC Using Optical Fiber Sensors', in: *Journal of The Electrochemical Society* vol. 157., no. 8 (June 2010), B1173–B1179, DOI: 10.1149/1.3436652.

[34] T. L. Bergman, A. S. Lavine, D. P. DeWitt and F. P. Incopera, *Incropera's Principles of Heat and Mass Transfer*, Global edition, eighth edition, Wiley, 2017.

[35] M. S. Wahl, J. J. Lamb, H. I. Muri, R. K. Snilsberg and D. R. Hjelme, 'Light Properties and Sensors', in: *Micro-Optics and Energy: Sensors for Energy Devices*, ed. by J. J. Lamb and B. G. Pollet, First Edition, Cham, Switzerland: Springer International Publishing, 2020, pp. 9–27, DOI: 10.1007/978-3-030-43676-6_2.

[36] J. J. Lamb, O. S. Burheim and D. R. Hjelme, 'Introduction', in: *Micro-Optics and Energy: Sensors for Energy Devices*, ed. by J. J. Lamb and B. G. Pollet, Cham, Switzerland: Springer International Publishing, 2020, pp. 3–8, DOI: 10.1007/978-3-030-43676-6_1.

[37] B. Elliott and M. Gilmore, '2 - Optical fiber theory', in: *Fiber Optic Cabling*, ed. by B. Elliott and M. Gilmore, Second Edition, Oxford: Newnes, 2002, pp. 11–53, DOI: https://doi.org/10.1016/B978-075065013-7/50003-9.

[38] A. Kersey et al., 'Fiber Grating Sensors', in: *Journal of Lightwave Technology,* vol. 15., no. 8 (Aug. 1997), pp. 1442–1463, DOI: 10.1109/50.618377.

[39] B. Illowsky et al., 'Measures of the Spread of the Data', in: *Introductory Statistics*, Houston, Texas: Rice University, 2013, chap. 2.7, pp. 110–120, URL: https://openstax.org/details/books/introductory-statistics.

[40] BioLogic Science Instruments, *FCT series User's Manual Version 5.22*, BioLogic Science Instruments SAS, Claix, France, 2013.

[41] Thorlabs, *Single Mode Fiber Optic Circulators*, URL: https://www.thorlabs.com/newgrouppage9.cfm?objectgroup_id=373 (visited on 29th Jan. 2024).

[42] Ibsen Photonics A/S, *I-MON 256 USB*, 2022, URL: https://ibsen.com/product/i-mon-256-usb/ (visited on 9th Nov. 2023).

[43] D. Bezmalinović, J. Radošević and F. Barbir, 'Initial Conditioning of Polymer Eelectrolyte Membrane Fuel Cell by Temperature and Potential Cycling', in: *Acta chimica Slovenica* ,vol. 62 (2015), pp. 83–87, DOI: 10.17344/acsi.2014.730.

[44] S. Ueda, S. Koizumi and Y. Tsutsumi, 'Initial conditioning of a polymer electrolyte fuel cells: The relationship between microstructure development and cell performance, investigated by small-angle neutron scattering', in: *Results in Physics* vol. 12 (2019), pp. 1871–1879, DOI: https://doi.org/10.1016/j.rinp.2019.01.066.

[45] S. Klug, *Application Note – Break-In Procedure for a PEMFC*, tech. rep., Revised July 2021, Scribner Associates Inc., 2021, URL: https://www.scribner.com/wp-content/uploads/2017/06/Application-Note-PEMFC-Break-in-Procedure-rev-B.pdf.

[46] J. Pharoah and O. Burheim, 'On the temperature distribution in polymer electrolyte fuel cells', in: *Journal of Power Sources* vol. 195., no. 16 (2010), pp. 5235–5245, DOI: https://doi.org/10.1016/j.jpowsour.2010.03.024.

[47] R. O'Hayre, S.-W. Cha, W. Colella and F. B. Prinz, 'Appendix B: Thermodynamic Data', in: *Fuel Cell Fundamentals*, ed. by R. O'Hayre, S.-W. Cha, W. Colella and F.B. Prinz, Third Edition, Hoboken, New Jersey: Wiley, 2016, pp. 519–528, DOI: https://doi.org/10.1002/9781119191766.app2.

[48] B. S. Pivovar and Y. S. Kim, 'The Membrane–Electrode Interface in PEFCs: I. A Method for Quantifying Membrane–Electrode Interfacial Resistance', in: *Journal of The Electrochemical Society* vol. 154., no. 8 (May 2007), B739–B744, DOI: 10.1149/1.2740005.

[49] T. E. Springer, T. A. Zawodzinski and S. Gottesfeld, 'Polymer Electrolyte Fuel Cell Model', in: *Journal of The Electrochemical Society* vol. 138., no. 8 (Aug. 1991), pp. 2334–2342, DOI: 10.1149/1.2085971.

[50] J. Zhang, H. Zhang, J. Wu and J. Zhang, 'Chapter 1 - PEM Fuel Cell Fundamentals', in: *Pem Fuel Cell Testing and Diagnosis*, ed. by J. Zhang, H. Zhang, J. Wu and J. Zhang, Amsterdam: Elsevier, 2013, pp. 1–42, ISBN: 978-0-444-53688-4, DOI: https://doi.org/10.1016/B978-0-444-53688-4.00001-2.

[51] B. J. Eichner, 'Simulation of temperature distribution within a PEM electrolysis stack using ex-situ thermal conductivity measurements', Master's Thesis, Department of Energy and Process Engineering, Norwegian University of Science and Technology (NTNU), Trondheim, Norway, 2023, URL: https://hdl.handle.net/11250/3115144.

[52] O. S. Burheim, S. Kjelstrup, J. G. Pharoah, P. Vie and S. Møller-Holst, 'Calculation of reversible electrode heats in the proton exchange membrane fuel cell from calorimetric measurements', in: *Electrochimica Acta* vol. 56 (Mar. 2011), pp. 3248–3257, DOI: 10.1016/j.electacta.2011.01.034.

[53] R. Schweiss, C. Meiser, T. Damjanovic, I. Galbati, N. Haak, *New Generation Sigracet® Gas Diffusion Layers (GDLs)*, URL: https://www.fuelcellstore.com/spec-sheets/sigracet-gdl-white-paper-new-generation.pdf (visited on 22nd Apr. 2024).

[54] The Engineering Toolbox, *Thermal Conductivity of Hydrogen*, 1997, URL: https://www.engineeringtoolbox.com/hydrogen-H2-thermal-conductivity-temperature-pressure-d_2106.html (visited on 23rd Apr. 2024).

[55] H. Sadeghifar, N. Djilali and M. Bahrami, 'Thermal conductivity of a graphite bipolar plate (BPP) and its thermal contact resistance with fuel cell gas diffusion layers: Effect of compression, PTFE, micro porous layer (MPL), BPP out-of-flatness and cyclic load', in: *Journal of Power Sources* vol. 273 (2015), pp. 96–104, DOI: https://doi.org/10.1016/j.jpowsour.2014.09.062.

[56] F. P. Incropera and D. P. DeWitt, 'Appendix 1: PROPERTY TABLES AND CHARTS (SI UNITS)', in: *Fundamentals of Heat and Mass Transfer*, Third Edition, 1990, URL: https://cecs.wright.edu/people/faculty/sthomas/htappendix01.pdf.

[57] R. Bock et al., 'The influence of graphitization on the thermal conductivity of catalyst layers and temperature gradients in proton exchange membrane fuel cells', in: *International Journal of Hydrogen Energy* vol. 45., no. 2 (2020), International Hydrogen and Fuel Cell Conference 2018, Trondheim, Norway, pp. 1335–1342, DOI: https://doi.org/10.1016/j.ijhydene.2018.10.221.

[58] M. Khandelwal and M. Mench, 'Direct measurement of through-plane thermal conductivity and contact resistance in fuel cell materials', in: *Journal of Power Sources* vol. 161., no. 2 (2006), pp. 1106–1115, DOI: https://doi.org/10.1016/j.jpowsour.2006.06.092.

[59] M. V. Williams, H. R. Kunz and J. M. Fenton, 'Analysis of Polarization Curves to Evaluate Polarization Sources in Hydrogen/Air PEM Fuel Cells', in: *Journal of The Electrochemical Society* vol. 152., no. 3 (2005), A635–A644, DOI: 10.1149/1.1860034.

[60] G. Zhang, L. Guo, L. Ma and H. Liu, 'Simultaneous measurement of current and temperature distributions in a proton exchange membrane fuel cell', in: *Journal of Power Sources* vol. 195., no. 11 (2010), pp. 3597–3604, DOI: https://doi.org/10.1016/j.jpowsour.2009.12.016.

[61] A. Weber et al., 'A Critical Review of Modeling Transport Phenomena in Polymer-Electrolyte Fuel Cells', in: *Journal of The Electrochemical Society* vol. 161 (Aug. 2014), F1254–F1299, DOI: 10.1149/2.0751412jes.
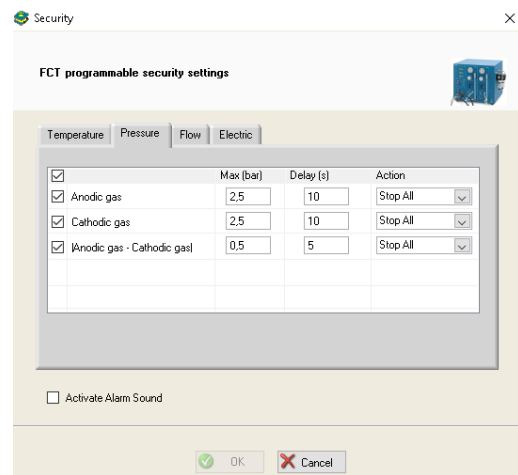
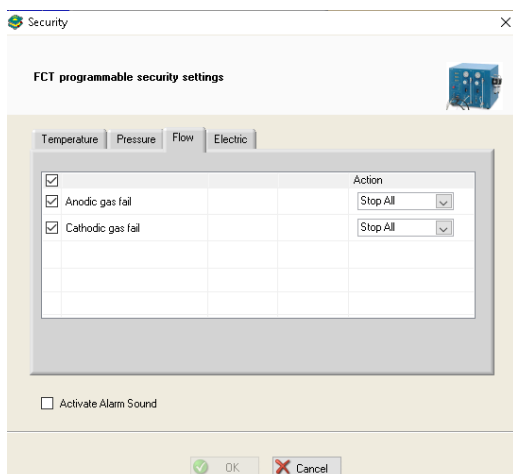# Appendix

Appendix A

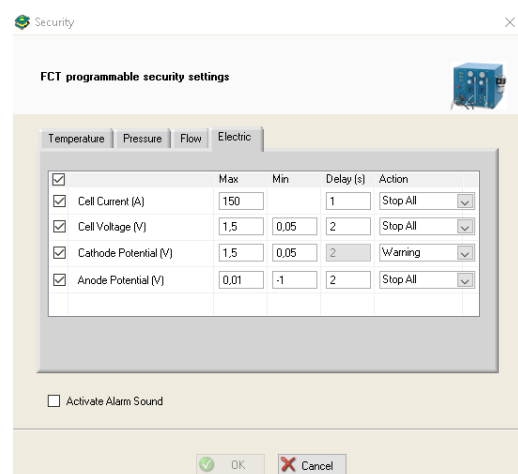# FCT Security Settings
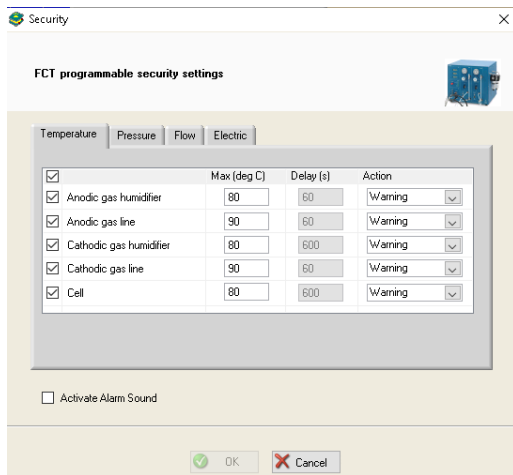
(a) Temperature limits.

(b) Pressure limits.

(c) Flow limits.

(d) Electric limits.

Figure A1: Images of the security limits and the respective actions set for the FCT system for all PEM fuel cell operation.

Appendix B

The Simulated Temperature Profiles Compared to Estimated Anode GDL Temperatures

Figure B1 - B3 shows the modeled temperature profiles for the anode side in comparison to the temperature estimations for the anode GDL. The anode GDL estimated temperature ranges are indicated in the same color as the respective current density.
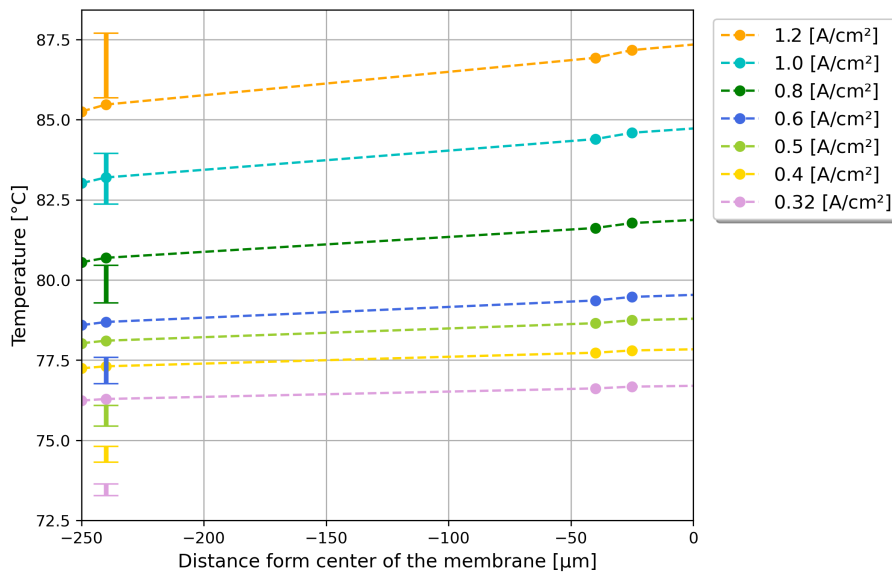

Figure B1: The simulated temperature profile in comparison to the estimated anode GDL temperatures for the fully humidified model scenario ($\lambda = 22$).
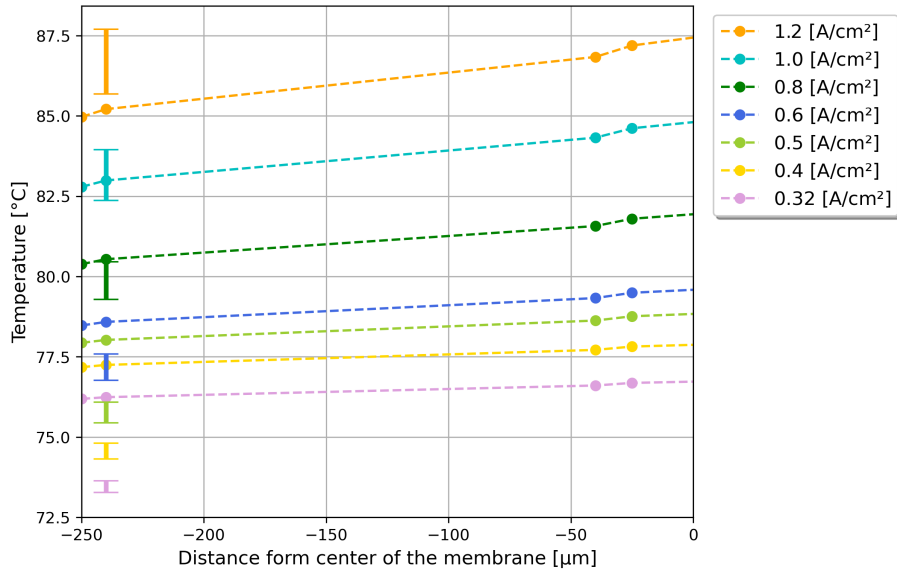
Figure B2: The simulated temperature profile in comparison to the estimated anode GDL temperatures for the moderately humidified model scenario ($\lambda = 15$).
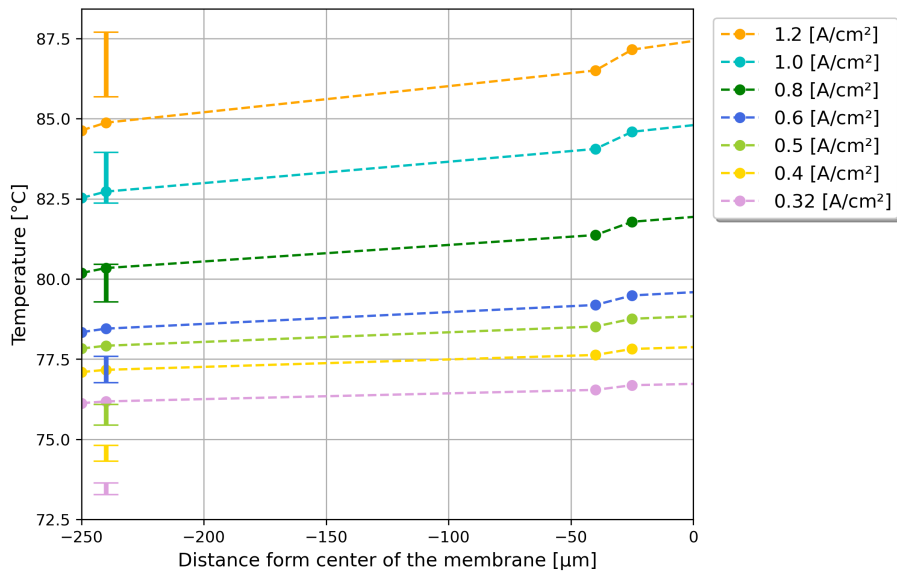

Figure B3: The simulated temperature profile in comparison to the estimated anode GDL temperatures for the poorly humidified model scenario ($\lambda = 10$).